REGIONAL VARIABILITY OF THE FREQUENCY DISTRIBUTION OF DAILY PRECIPITATION AND THE SYNOPTIC CHARACTERISTICS OF HEAVY PRECIPITATION EVENTS IN PRESENT AND FUTURE CLIMATE SIMULATIONS

By

ANTHONY M. DEANGELIS

A dissertation submitted to the

Graduate School-New Brunswick

Rutgers, The State University of New Jersey

in partial fulfillment of the requirement

for the degree of

Doctor of Philosophy

Graduate Program in Atmospheric Science

written under the direction of

Anthony J. Broccoli

and approved by

_____

_____

_____

_____

New Brunswick, New Jersey

May 2014

ABSTRACT OF THE DISSERTATION

Regional Variability of the Frequency Distribution of Daily Precipitation and the Synoptic Characteristics of Heavy Precipitation Events in Present and Future Climate Simulations

By

ANTHONY M. DEANGELIS

Dissertation Director:

Anthony J. Broccoli

Changes in the characteristics of daily precipitation in response to global warming may have serious impacts on human life and property. An analysis of precipitation in climate models is performed to evaluate how well the models simulate the present climate and how precipitation may change in the future. Models participating in phase 3 and 5 of the Coupled Model Intercomparison Project (CMIP3 and CMIP5) have substantial biases in their simulation of heavy precipitation intensity over parts of North America during the 20th century. Despite these biases, the large-scale atmospheric circulation accompanying heavy precipitation is either simulated realistically or the strength of the circulation is overestimated. The biases are not related to the large-scale flow in a simple way, pointing toward the importance of other model deficiencies, such as coarse horizontal resolution and convective parameterizations, for the accurate

simulation of intense precipitation. Although the models may not sufficiently simulate the intensity of precipitation, their realistic portrayal of the large-scale circulation suggests that projections of future precipitation may be reliable. In the CMIP5 ensemble, the distribution of daily precipitation is projected to undergo substantial changes in response to future atmospheric warming. The regional distribution of these changes was investigated, revealing that dry days and days with heavy-extreme precipitation are projected to increase at the expense of light-moderate precipitation over much of the middle and low latitudes. Such projections have serious implications for future impacts from flood and drought events. In other places, changes in the daily precipitation distribution are characterized by a shift toward either wetter or drier conditions in the future, with heavy-extreme precipitation projected to increase in all but the driest subtropical subsidence regions. Further analysis shows that increases in heavy precipitation in midlatitudes are largely explained by thermodynamics, including increases in atmospheric water vapor. However, in low latitudes and northern high latitudes, changes in vertical velocity accompanying heavy precipitation are also important. The strength of the large-scale atmospheric circulation is projected to change in accordance with vertical velocity in many places, though the circulation patterns, and therefore physical mechanisms that generate heavy precipitation, may remain the same.

Acknowledgements

Most importantly, I would like to thank my advisor, Dr. Anthony Broccoli, for not only guiding me through my graduate career but also initiating my interest in research. If it wasn't for his initial encouragement to apply my academic skills to research as an undergraduate, I may have never chosen the path that I am on. Serving as my advisor since 2007, Tony's ongoing support, advice, constructive criticism, and friendship has helped shape the researcher and person that I am today. I will leave Rutgers having no regrets that I chose Rutgers as my graduate institution and Tony Broccoli as my advisor.

Other professors at Rutgers have also played a role in shaping and developing my professional interests and skills. Dr. Ying Reinfelder also saw my potential as a scientist and encouraged me to participate in her research group. In working with her, she provided additional friendship, support, and advice that allowed me to see the scientific process from a different and more comprehensive perspective. I also thank Dr. Alan Robock, who in working with Ying and I, gave useful scientific feedback, offered me additional career building support and advice, and encouraged the publication of my first scientific article. Other members of this research group who deserve recognition for their contributions include Dr. Francina Dominguez (University of Arizona), Dr. David Robinson (Rutgers University), and Dr. Deniz Kustu (Rutgers University at the time).

More recently, the members of my Ph.D. committee, in addition to Tony Broccoli, have played a substantial role in helping develop the work that appears in this thesis. In particular, Dr. Steven Decker has provided input regarding synoptic meteorology, gave useful feedback on analyses, and carefully edited my first publication

and posters related to the project. Dr. Benjamin Lintner has encouraged the continual presentation and discussion of my work in research group meetings, has provided ongoing feedback and suggestions, and gave me useful ideas for how to analyze data. Finally, Dr. Gabriel Vecchi provided useful feedback and suggestions.

My fellow graduate students and colleagues at Rutgers have also contributed to my professional and personal development and aided in the completion of my research. Matthew Niznik helped download and process much of the CMIP5 output that makes up this thesis, contributed analyses that helped develop part of the dissertation, and was always available as both a colleague and friend. Paul Loikith also helped obtain CMIP5 output, provided useful ideas, and served as a mentor and friend since the end of my undergraduate years. Stephen Nicholls was always willing to have lengthy discussions about science and helped with numerous computing tasks. Other graduate students, friends, and colleagues, who stand out for providing professional and social support along the way, include Michael Erb, Ross Alter, Bryan Raney, Brian Marmo, Jessie Sagona, and Mira Berdalh. I also thank Mike Ferner and Mina Azer for their ongoing technical assistance and members of the Environmental Science Department and Graduate School New Brunswick staff for their administrative assistance.

Finally, I thank my family for their support as I complete my current goal of obtaining a Ph.D. and embark on a new journey in my scientific career path.

Financial support for this work was provided by a fellowship from the Environmental Protection Agency Science to Achieve Results (EPA STAR) program and a grant (NA09OAR4310109) from the NOAA Climate Program Office. Part of this thesis has been published in the Journal of Climate, titled “A Comparison of CMIP3

Simulations of Precipitation over North America with Observations: Daily Statistics and Circulation Features Accompanying Extreme Events," by Anthony M. DeAngelis, Anthony J. Broccoli, and Steven G. Decker. The American Meteorological Society holds copyright to that work.

Table of Contents

List of Tables

List of Illustrations

Figure 33. Global median sensitivity of precipitation at specific percentiles (% K^{-1}) computed from (a) annual, (b) DJF, and (c) JJA days (curves and shading, see section 4.3 for details). At each percentile, the model median (black line), interquartile range (IQR, 25^{th}-75^{th} percentile, dark shading) and full range (light shading) of the sensitivities are shown. For comparison, the intermodel variability (min, 25^{th} percentile, median, 75^{th} percentile, max) of the global median grid cell value of Sh and Rh (red and blue box-and-whiskers, respectively) are plotted to right of the respective plots, using the same y-axis. Note that Sh and Rh are computed using all percentiles $\geq 99^{th}$ (as described in section 4.2.b). The black and green dashed lines indicate 0% K^{-1} and 7% K^{-1}, respectively. ... 154

Figure 34. Winter (DJF) composite patterns of various quantities during heavy precipitation events at a grid cell in the northeastern United States (black box), for the CMIP5 ensemble mean. (left) Composite patterns for the historical period, (middle) RCP8.5 period, and (right) their difference. Pressure at mean sea level (PMSL, hPa, line contours) is shown in every panel, with a contour interval of 2 hPa in the historical and RCP8.5 plots and 1 hPa in the difference plots (negative changes are dashed, positive are solid). Color fills show (a)-(c) z-scores of geopotential height at 500 mb (Z500*), (d)-(f) wind voriticity at 850 mb (ζ850, 10^{-6} s^{-1}), and (g)-(i) **Q**-vector convergence (QVC, 10^{-19} m kg^{-1} s^{-1}); see section 4.2.c for further description of the plotted quantities. In the difference plots, grid cells where at least 12 of 17 individual models have the same sign of change as the model mean and the change is statistically significant (see section 4.4.a) in at least 6 of those models, are identified with a dot for PMSL and cross for the respective color-filled quantities. Below each of the difference plots, the spatial

1. Introduction

1.1 Motivation and summary

Changes in the frequency distribution of precipitation in response to atmospheric warming have been detected in observations and projected in climate model simulations of future climate with increased greenhouse gases. Such changes, including an increased occurrence of extreme precipitation events and increased frequency of prolonged dry periods, may have serious consequences for human life, property, agriculture, water resources, and ecosystems (Easterling et al. 2000; Rappaport 2000; IPCC 2012). It is important that scientists better quantify the regional distribution of these projected changes as society prepares for climate change. Understanding the physical mechanisms that generate changes in characteristics of precipitation in observations and climate models will also help improve our fundamental understanding of the climate system and may lead to better predictions. In order to reliably use climate models to predict and understand future changes in precipitation, it is important that they realistically simulate the statistics of high-frequency precipitation as well as the physical mechanisms that generate heavy precipitation. Evaluating climate model simulations against high-quality observations over the 20th century is therefore critical. In this thesis, climate models participating in phase 3 and 5 of the Coupled Model Intercomparison Project (CMIP3 and CMIP5) are used to better understand regional projections of daily precipitation statistics, the underlying physical mechanisms for heavy precipitation, and how well the models simulate these characteristics during the late 20th century.

1.2 Previous evaluations of simulated precipitation statistics

Several previous studies have evaluated climate model simulations of daily and higher frequency precipitation. Despite differences among the studies regarding the models and observations used, geographical domain analyzed, and quantitative methods, many of the same model biases were found over various regions: too many wet days, overestimation of the frequency and intensity of light precipitation events, and underestimation of the frequency and intensity of heavy events (e.g., Zwiers and Kharin 1998; Iorio et al. 2004; May 2004; Emori et al. 2005; Kimoto et al. 2005; Kharin et al. 2007; Perkins et al. 2007; Sun et al. 2007; Wehner et al. 2010; Sillmann et al. 2013a). Such biases in simulated precipitation were found not only with coarse resolution climate models but also high resolution regional models (Frei et al. 2003; Gutowski et al. 2003; Semmler and Jacob 2004; Boroneant et al. 2006; Lenderink and Meijgaard 2008; Boberg et al. 2009). In one study, high resolution regional models were shown to overestimate heavy and extreme precipitation over much of the contiguous United States (Wehner 2013). In the studies referenced above, model biases existed whether observations were treated as station point values or gridded at a resolution comparable to the climate models studied.

Several studies have shown that when climate models are run at higher spatial resolution, the simulation of high frequency heavy precipitation statistics improves (Iorio et al. 2004; Kimoto et al. 2005; Kharin et al. 2007; Wehner et al. 2010; Dulière et al. 2011). One reason higher resolution climate models simulate heavy precipitation better may be that the models rely less on convective parameterizations when run at higher resolutions (Iorio et al. 2004; Wehner et al. 2010; Li et al. 2011). Previous studies imply

that convective parameterizations in climate models partly result in the underestimation of intense precipitation and too frequent simulation of light events (Gutowski et al. 2003; Iorio et al. 2004; May 2004; Emori et al. 2005; Kharin et al. 2007; Wilcox and Donner 2007; Wehner et al. 2010; Li et al. 2012). Some studies have demonstrated that convective precipitation can be made more realistic by changing the characteristics of convective parameterization schemes or by embedding cloud resolving models into climate models (Iorio et al. 2004; Emori et al. 2005; Wilcox and Donner 2007; Li et al. 2012). Other reasons for improved simulation of intense precipitation with increased horizontal resolution may include improved dynamics and vertical motion, better simulation of tropical cyclones, more realistic representation of topography, and better ability to resolve mesoscale processes and land surface-atmosphere interactions (Colle and Mass 2000; Gutowski et al. 2003; Iorio et al. 2004; Semmler and Jacob 2004; Wehner et al. 2010; Dulière et al. 2011; Li et al. 2011).

Since climate models are used to predict future changes in extreme precipitation in response to global warming, it is important to know how well climate models simulate observed changes in heavy precipitation which are associated with warming over the late 20th century. Unfortunately, previous studies have shown that climate model simulations of observed changes in heavy precipitation are rather poor. For example, Kiktev et al. (2003) showed that HadAM3, the atmospheric component of the third climate configuration of the Met Office Unified Model (HadCM3), has little skill in reproducing observed trends in precipitation indices over the late 20th century, such as the annual maximum five-day precipitation event. Other studies have shown that climate models underestimate observed positive trends in heavy precipitation over a variety of domains,

such as Northern Hemisphere land areas (Min et al. 2011), South America (Marengo et al. 2010), Germany (Tomassini and Jacob 2009), Australia (Alexander and Arblaster 2009), and the contiguous United States (Wuebbles et al. 2013). Observed amplifications in tropical extreme precipitation with increased sea surface temperatures are underestimated by atmosphere-only and coupled simulations participating in CMIP3 (Allan and Soden 2008; Gastineau and Soden 2011). Lenderink and Meijgaard (2008) showed that a high-resolution regional climate model underestimates the increase in intense hourly precipitation observed with higher daily temperatures over Europe during the 20th century. Finally, a severe underestimation in the increase of heavy precipitation with warming was found at the global scale in CMIP3 models using reanalysis and Global Precipitation Climatology Product observations (Liu et al. 2009; Shiu et al. 2012). Shiu et al. (2012) hypothesize that underestimations in the heavy precipitation response to warming mainly arise from the inability of models to resolve convection. These previous studies suggest that future increases in the frequency and intensity of heavy and extreme precipitation events in response to global warming may be larger than current climate model simulations indicate. Improving resolution and the simulation of convection in models may be necessary for more reliable projections.

Changes in the physical mechanisms that generate extreme precipitation, such as features of the large-scale circulation, are likely to play a role in quantitative changes in extreme precipitation in the future (Zwiers and Kharin 1998; Yin 2005; Meehl et al. 2005; Emori and Brown 2005; Lionello and Giorgi 2007; Raible et al. 2007; Archambault et al. 2008; Gutowski et al. 2008a,b; Gastineau and Soden 2009; and others). Furthermore, it is possible that unrealistic climate model simulations of the large-scale

atmospheric dynamics and thermodynamics associated with extreme precipitation events lead to biases in the amount of precipitation simulated. For these reasons, it is of great importance to evaluate the ability of climate models to reproduce the large-scale physical mechanisms that are observed with extreme precipitation events. While it has been shown that climate models simulate fairly realistic atmospheric circulation patterns associated with extreme precipitation events over the Maritime Alps (Boroneant et al. 2006) and central United States (Gutowski et al. 2008b; Kawazoe and Gutowski 2013), few studies have evaluated the large-scale physical processes linked to extreme precipitation in climate models. Additional research on evaluating such physical mechanisms in a comprehensive way is therefore warranted, and chapter 2 of this dissertation aims to address this topic.

1.3 Observed and simulated changes in precipitation statistics

Using observations of the recent past, many studies show that changes in heavy to extreme precipitation events have occurred during the 20th century. Groisman et al. (2005) studied station precipitation data and found that increases in heavy precipitation frequency and intensity were prevalent over many global land regions during mainly the second half of the 20th century. Alexander et al. (2006) show that the frequency and intensity of heavy precipitation days (days with precipitation above the 90th percentile) increased between 1951 and 2003 over Eurasia and North America. More increases than decreases in annual maximum 1 and 5 day precipitation amounts were found over North America and Eurasia in Min et al. (2011), consistent with Alexander et al. (2006). Analyses focused on the United States show robust increases in the intensity and

frequency of extreme precipitation in the central part of the country over the 20th century (Groisman et al. 2004; Groisman et al. 2012; Villarini et al. 2013a). Perhaps to summarize, Westra et al. (2013) find that nearly two-thirds of stations globally show increases in the annual maximum daily precipitation amount over the 20th century.

Using an ensemble of state-of-the-art coupled atmosphere-ocean climate model simulations, studies overwhelmingly show that increases in the frequency and intensity of heavy precipitation may continue over most global regions in response to future anthropogenic warming (e.g., Meehl et al. 2005; Tebaldi et al. 2006; Kharin et al. 2007; Sun et al. 2007; Orlowsky and Seneviratne 2012; Seneviratne et al. 2012; Kharin et al. 2013; Scoccimarro et al. 2013; Sillmann et al. 2013b; Villarini et al. 2013b). Projected increases in heavy to extreme precipitation are also found, for example, in high resolution regional simulations over North America (Wehner 2013) and in an ensemble of atmosphere-mixed layer ocean models (Barnett et al. 2006). Areas with robust projected decreases in heavy precipitation are confined to subtropical subsidence regions in the Pacific and Atlantic oceans (e.g., Kharin et al. 2007; Sun et al. 2007; Kharin et al. 2013) and small low-latitude land regions seasonally (e.g., Barnett et al. 2006). The qualitative consistency between observed and simulated changes in intense precipitation as well as attribution analyses suggest that the affects of anthropogenic warming on extreme precipitation are already occurring (Min et al. 2011; Pall et al. 2011; Seneviratne et al. 2012; IPCC 2013). However, natural climate variability, sparse observations over some regions, and uncertainties in climate model simulations makes the detection and attribution of observed trends in heavy precipitation an ongoing challenge (Zhang et al. 2001; Kendon et al. 2008; Min et al. 2011; Seneviratne et al. 2012).

Understanding the physical mechanisms for changes in heavy precipitation, as well as the entire distribution of high frequency precipitation, is critical for improving scientific understanding of the climate system and projections. An emerging scientific consensus is that changes in heavy to extreme precipitation are disproportionately larger than changes in mean or total precipitation, in both observations and simulations, and that extreme precipitation increases even in places where mean or total precipitation does not change or decreases (Easterling et al. 2000; Allen and Ingram 2002; Groisman et al. 2004; Groisman et al. 2005; Kharin and Zwiers 2005; Barnett et al. 2006; Kharin et al. 2007; Sun et al. 2007; Liu et al. 2009; Kharin et al. 2013; Scoccimarro et al. 2013; Sillmann et al. 2013b). This discrepancy suggests that there are different underlying physical mechanisms by which total and extreme precipitation respond to atmospheric warming.

Climate model simulations show that changes in mean precipitation are constrained by the tropospheric energy balance between latent heat released from precipitation and infrared cooling (Allen and Ingram 2002; Held and Soden 2006; Allan and Soden 2007; Vecchi and Soden 2007; Lambert and Webb 2008; Previdi and Leipert 2008; Giorgi et al. 2011; O'Gorman et al. 2012; Allan et al. 2013). In climate models, the global sensitivity of mean precipitation is about 1-3.5 % K^{-1} (e.g, Allen and Ingram 2002; Held and Soden 2006; Sun et al. 2007; Kharin et al. 2013), which is smaller than that found in some observational analyses (e.g., Wentz et al. 2007; Liu et al. 2009; Shiu et al. 2012). Differences between the observed and simulated sensitivity of mean precipitation may be related to the relatively short record of precipitation observations and type of radiative forcing (e.g., greenhouse gases versus aerosols) resulting in

atmospheric warming (Previdi and Liepert 2008; Liepert and Previdi 2009). Contrary to total precipitation, changes in extreme precipitation intensity are thought to be broadly constrained by changes in atmospheric moisture because these events occur on short time scales and result from large-scale moisture convergence (Allen and Ingram 2002; Trenberth et al. 2003; Held and Soden 2006; Pall et al. 2007). Following the Clausius-Clapeyron (hereafter C-C) relationship and assuming constant relative humidity, atmospheric moisture increases at approximately 7 % K^{-1} with warming for temperatures typical of the lower troposphere (e.g., Held and Soden 2006). This suggests that extreme precipitation may increase by about 7 % K^{-1} if changes in the large-scale atmospheric circulation are small. However, as discussed later in this introduction, regional thermodynamic and dynamical mechanisms may be more complex.

An important consequence of the differing rates by which total and extreme precipitation respond to warming is that the distribution of high frequency precipitation must change. In particular, heavy events may become more frequent while light or moderate events become less frequent (Giorgi et al. 2011). Using a metric that characterizes dry spell length and precipitation intensity together, Giorgi et al. (2011) find projected increases in the intensity of the hydrologic cycle over many global land regions in climate model simulations, suggesting a shift in the precipitation distribution toward more dry periods and/or increased heavy precipitation in the future. In Sillmann et al. (2013b), increases in consecutive dry days coincident with increases in heavy precipitation indices are also found over broad middle and low-latitude land regions in CMIP5 projections. Additional studies using coupled climate model simulations show decreasing light/moderate and increasing heavy daily precipitation in response to global

warming, both globally and regionally (Pall et al. 2007; Sun et al. 2007; Gastineau and Soden 2009; Scoccimarro et al. 2013). Studies using monthly precipitation find a similar response of precipitation to warming over tropical land (Lintner et al. 2012) and between 60°S-60°N (Lau et al. 2013) in simulations, whereby dry and heavy precipitation periods increase in frequency while light or moderate periods decrease. The simulated changes in the distribution of precipitation have also been detected in observations to a limited extent. Using satellite data, Lau and Wu (2011) find increased very light, decreased light-moderate, and increased heavy daily precipitation in response to warmer SSTs in the tropical oceans. Giorgi et al. (2011) find increases in hydrologic intensity over the late 20th century over various land regions using gridded and station observations. Lintner et al. (2012) extended their analysis to monthly gauge and satellite observations and found a similar increasing-decreasing-increasing response of dry-light-heavy months, respectively, to warming over the tropics. However, smaller-scale regional analyses over the United States show that daily precipitation of all intensities has increased over the 20th century in many regions (Karl and Knight 1998), suggesting that there is regional variability in changes in the precipitation distribution. Further exploration of this regional variability, both in observations and models, is necessary to better understand the response of the high frequency precipitation distribution to global warming.

The local and regional projected changes in the distribution of precipitation have not been comprehensively explored in previous studies due to limitations in the analysis methods, including aggregation of locations over large domains or averaging of precipitation over wide ranges of intensity. Recently, Loikith et al. (2013) applied k-means cluster analysis to investigate the local and regional variability of the detailed

characteristics of the daily temperature distribution over North America. Motivated by this work, the same methodology is applied to projected changes in the local daily precipitation distribution in CMIP5 simulations in chapter 3 of this dissertation. Such an analysis allows for a comprehensive exploration of the local and regional variability in projected changes in the high frequency distribution of precipitation.

1.4 Physical mechanisms for changes in heavy precipitation

Much attention has been given to understanding the underlying physical mechanisms for changes in heavy precipitation in response to global warming. As mentioned earlier, increases in heavy precipitation intensity may broadly be explained by increases in atmospheric water vapor, which follow the C-C rate of 7 % K^{-1}. However, recent studies show that the thermodynamical mechanisms are more complex, and that dynamical mechanisms are important when considering small spatial scales.

O'Gorman and Schneider (2009a,b) (hereafter OS09a,b) developed a comprehensive scaling to explain simulated increases in extreme precipitation that is based on the condensation of water vapor during extreme events assuming a saturated atmosphere. Their scaling takes into account the vertical profile of tropospheric temperature and upward vertical velocity when extreme precipitation occurs. Thermodynamically, the OS09a,b scaling is more complex than C-C scaling because it accounts for changes in atmospheric stability with warming. Additionally, because it includes vertical velocity, the OS09a,b scaling also accounts for dynamical changes that occur during extreme precipitation events. The predicted thermodynamic sensitivity of globally-averaged extreme precipitation to warming emerging from the OS09a,b scaling

(~5-6 % K^{-1} in coupled climate models) is smaller than the C-C rate of 7 % K^{-1}, mostly because of a decrease in the moist adiabatic lapse rate with warming. The OS09a,b full scaling (including both thermodynamical and dynamical components) sufficiently predicts the actual extreme precipitation response to warming, both globally- and zonally-averaged, in aquaplanet and coupled climate model simulations (Kharin et al. 2007; Sun et al. 2007; Sugiyama et al. 2010; Kharin et al. 2013). A slight variation of the OS09a,b scaling, introduced by Sugiyama et al. (2010), incorporates precipitable water, vertical velocity at 500 mb, and the vertical profile of atmospheric moisture not assuming saturation. Their variation is shown to perform similarly to the OS09a,b scaling over the tropical oceans, but is perhaps a better match for actual precipitation sensitivities to warming at the highest percentiles in some climate model simulations. In the work of OS09a,b, Sugiyama et al. (2010), and others (e.g., Emori and Brown 2005), changes in vertical velocity are shown to be a critical component of the extreme precipitation response to warming, especially in low-latitude regions. Thus, changes in aspects of the atmospheric circulation during extreme events are important when considering the regional sensitivity of extreme precipitation.

The atmospheric circulation accompanying extreme precipitation events may change in response to a number of physical mechanisms as a result of climate change. A poleward shift in extratropical storm tracks, as a result of changes in the horizontal and vertical structure of atmospheric temperature, is perhaps the most robust signature of global warming on the atmospheric circulation found in both observations and climate model simulations (McCabe et al. 2001; Yin 2005; Bengtsson et al. 2006; Wang et al. 2006; Salathé 2006; Raible et al. 2007; O'Gorman 2010; Bender et al. 2012; Chang et al.

2012). It is plausible that changes in storm tracks may have some direct effect on the intensity of extreme precipitation at middle and high latitudes (e.g., Raible et al. 2007; Pfahl and Wernli 2012). Changes in the atmospheric circulation accompanying extreme precipitation events in the extratropics may also be influenced by changes in modes of climate variability that are either directly or indirectly (i.e., through teleconnentions) related to the local circulation patterns, such as the Madden-Julian oscillation (MJO) (Jones and Carvalho 2011; Jones and Carvalho 2012), El Niño-Southern Oscillation (ENSO) (Haylock et al. 2006; Schubert et al. 2008; Zhang et al. 2010), North Atlantic oscillation (NAO) (Yiou and Nogaj 2004; Raible et al. 2007; Zhang et al. 2010), Pacific-North American regime (Archambault et al. 2008), or Pacific Decadal oscillation (PDO) (Zhang et al. 2010).

In the tropics, regional changes in the atmospheric circulation accompanying extreme precipitation may be influenced by changes in mean tropical conditions, including changes in the Hadley or Walker circulations and the regional pattern of oceanic warming (Held and Soden 2006; Vecchi et al. 2006; Lu et al. 2007; Vecchi and Soden 2007; Gastineau et al. 2008; Chou et al. 2009; Seager et al. 2010; Huang et al. 2013). Dynamical feedbacks associated with changes in gross moist stability, an effective measure of tropical static stability (Chou et al. 2013), have also been shown to influence tropical precipitation and circulation, and may therefore affect extreme events (e.g., Chou and Neelin 2004; Chou et al. 2009). More intense precipitation rates in the tropics can also feed back on the vertical velocity and low-level convergence accompanying extreme events through enhanced latent heat release (Trenberth 1999; Allen and Ingram 2002; Trenberth et al. 2003; Pall et al. 2007). Finally, changes in the

frequency, intensity, and tracks of tropical cyclones may affect the regional changes in extreme precipitation in the tropics and at higher latitudes (e.g., Kunkel et al. 2012), though deficiencies in simulating tropical cyclones in climate models make this mechanism difficult to study (e.g., Manganello et al. 2012; Camargo 2013).

Previous studies have explored the connection between changes in atmospheric circulation and extreme precipitation to some extent. In Raible et al. (2007), a comparison between the climate of the Maunder Minimum and present day in the NCAR CCSM2 model shows that a southward shift in Northern Hemisphere storm tracks in a colder climate is also associated with a southward shift in extreme precipitation. Gastineau and Soden (2009) look at changes in metrics of the atmospheric circulation, such as 500 mb upward velocity and 850 mb vorticity and wind speed, as a function of precipitation intensity between future and present simulations in the CMIP3 ensemble. They find a slight intensification in 850 mb wind and vorticity associated with heavy precipitation (>95th percentile) in the extratropics (30°-90°), consistent with a poleward shift and intensification of storm tracks in a warmer climate. They also find a weakening of the circulation strength associated with heavy precipitation in the tropics (30°S-30°N), which is supported by satellite observations and atmosphere-only GCMs in a later study by the authors (Gastineau and Soden 2011). The latter finding is in contrast to Sugiyama et al. (2010), who show that changes in the vertical velocity associated with extreme tropical precipitation vary considerably among climate models, with some models showing large increases at very high percentiles. The discrepancies in these findings may reflect differences in the subset of models used and methodology. Finally, changes in the atmospheric circulation accompanying extreme precipitation appear to be marginal in the

mid-latitudes, as shown with a regional analysis of the central United States in Gutowski et al. (2008b) and aggregate analysis for 30°-60°N in Sugiyama et al. (2010).

A limitation of earlier studies is that metrics characterizing the atmospheric circulation during extreme precipitation events are computed for broad geographical regions (i.e., the aggregation or mean of data points over 30°S-30°N or other zonal bands). This prevents an analysis of circulation changes that are specific to locations with possibly different behavior from the zonal mean, such as the equatorial east Pacific (e.g., Vecchi and Soden 2007; Huang et al. 2013). Some studies have looked at the spatial patterns of changes in extreme circulation metrics independently from precipitation (e.g., Raible et al. 2007; Gastineau and Soden 2009). However, extreme precipitation is not always associated with extreme circulation features (Pfahl and Wernli 2012), and a direct link cannot be made between changes in extreme circulation and precipitation in those studies. An in-depth analysis of the changes in atmospheric circulation directly associated with extreme precipitation events at the grid cell level is therefore warranted. In chapter 4 of this dissertation, such an analysis is provided.

2. Evaluation of CMIP3 and CMIP5 simulations

2.1 Introduction

In this chapter, the precipitation output from the CMIP3 and CMIP5 ensembles is compared with high quality observations over North America. Daily precipitation statistics and the large-scale circulation features accompanying extreme precipitation events are evaluated. This chapter focuses on CMIP3, as the CMIP5 ensemble was not yet available at the time when analysis began. In section 2.2, the observations, CMIP3 climate models, and general methodology are described. Precipitation statistics in CMIP3 are evaluated and discussed in section 2.3, while the evaluation of large-scale physical mechanisms accompanying extreme precipitation in CMIP3 simulations is shown and discussed in section 2.4. In section 2.5, a parallel evaluation using the CMIP5 ensemble is presented, where similarities and differences between CMIP3 and CMIP5 are highlighted and discussed. The chapter concludes with a brief statement in section 2.6. Much of the material presented in this chapter has been published in the Journal of Climate, titled "A Comparison of CMIP3 Simulations of Precipitation over North America with Observations: Daily Statistics and Circulation Features Accompanying Extreme Events," by Anthony M. DeAngelis, Anthony J. Broccoli, and Steven G. Decker.

2.2 Data and Methodology

2.2.a Precipitation Observations

Gridded observations of daily precipitation covering all global land areas and the time period 1979 to present have been developed by the Climate Prediction Center (CPC). The gridded precipitation product is produced from rain gauge observations over global land areas. The stations used in the gridded product include a combination of special collections from the CPC as well as stations from the Global Telecommunications System (GTS) (Chen et al. 2008a). A quality control procedure utilizing satellite data and numerical model output was applied to the station data before gridding (Chen et al. 2008b), which was an improvement to the quality control used for the CPC United States precipitation product described in Higgins et al. (2000). After applying the quality control procedure, the station data were placed on a 0.5°x0.5° longitude-latitude grid using optimal interpolation. A comparison of optimal interpolation with other gridding methods for this precipitation product is provided in Chen et al. (2008c) and reveals no significant differences between methods. In this dissertation, the 0.5°x0.5° grid of the observations was converted to a 2.5°x2.5° grid via area averaging to be more comparable with the typical resolution of the climate models analyzed (see section 2.2.c) before computing precipitation statistics, a procedure which has been shown to improve agreement between observed and simulated metrics involving extreme precipitation (Chen and Knutson 2008). Precipitation analyses shown in this chapter focus on North America because of the high density and large number of stations that went into the CPC gridded product over this region during the late 20th century (Chen et al. 2008a,c). Precipitation data is missing for some days over parts of North America; however, because the percentage of missing days at any grid cell is no more than 0.5% over the analysis period (1979-99), the missing data should not impact the results.

2.2.b North American Regional Reanalysis

The National Centers for Environmental Prediction North American Regional Reanalysis (NARR) (Mesinger et al. 2006) was used as observed data for variables other than precipitation for the evaluation of large-scale atmospheric patterns associated with extreme precipitation. For analysis, the NARR was regridded from its initial spatial resolution of 32 km x 32 km on a Lambert Conformal Conic projection to a 2.5°x2.5° resolution to match the grid on which the precipitation observations and climate models were analyzed. A linear average of all values whose grid cell centers on the original NARR grid fell within the boundaries of the new 2.5°x2.5° grid determined the values on the coarser grid. Furthermore, three-hourly NARR data were converted to daily averages over the daily period 12Z to 12Z to match the CPC precipitation observations.

2.2.c CMIP3 output

The climate model simulations evaluated in sections 2.3 and 2.4 of this chapter were 20th century runs from the CMIP3 collection. These simulations were forced with realistic temporal variations of anthropogenic and natural forcings as deemed appropriate by the individual modeling groups (Meehl et al. 2007). The output from the CMIP3 models is available at the World Climate Research Programme's CMIP3 multimodel dataset archive hosted by the Program for Climate Model Diagnosis and Intercomparison [http://www-pcmdi.llnl.gov/ipcc/about_ipcc.php]. There were 17 models with sufficient daily precipitation output for the evaluation of precipitation statistics, and those models are listed in Table 1 (note that expansions of all CMIP3 model acronyms are available

online at http://www-pcmdi.llnl.gov/ipcc/model_documentation/ipcc_model_documentation.php). Of those 17 models, only 12 had archived meteorological variables other than precipitation for use in evaluating physical mechanisms associated with heavy precipitation events; such models are also identified in Table 1. Due to the limited availability of multiple ensemble members, only one 20th century ensemble member run was analyzed from each model.

The output from each climate model was regridded to the 2.5°x2.5° grid on which the precipitation observations and NARR output were analyzed. The regridding procedure consisted of either linear interpolation if the original climate model grid area (in square degrees) was larger than that of the target grid or area averaging otherwise. The specific models that were regridded using area averaging are shown in Table 1, along with the original horizontal resolution of all models. Because the original spatial resolution of some models is much coarser than 2.5°x2.5°, the sensitivity of the results to the resolution of the analysis grid was evaluated by performing a parallel analysis of precipitation statistics using a 5.0°x5.0° analysis grid. While in some cases there was better agreement between the models and observations on the 5.0°x5.0° grid, the improvement was quite small and most of the same model biases remained. All analyses shown in this paper are therefore presented on the 2.5°x2.5° common grid.

2.2.d General analysis methods

The time period with the greatest overlap among the CPC observations, NARR, and CMIP3 models is 1 January 1979- 31 December 1999. Due to inconsistencies in the calendar setup among the CMIP3 models, 29 February was removed from all datasets,

resulting in a time domain of exactly 7665 days for the CPC and NARR observations and all CMIP3 models. The 1979-99 time period of analysis was considered too short for long term trends in precipitation statistics to be reliable, thus only summary statistics over this period were analyzed. This decision was based on a separate analysis using the CPC United States precipitation dataset (described in Higgins et al. 2000) over the period 1961-98, which showed that long term trends in daily precipitation statistics are spatially noisy and unlikely to be statistically significant or meaningful over time periods as short as the one used in this dissertation (not shown).

While many studies involving extreme precipitation utilize metrics based on Generalized Extreme Value or other statistical distributions (e.g., Zwiers and Kharin 1998; Wilby and Wigley 2002; May 2004; Semmler and Jacob 2004; Kharin and Zwiers 2005; Kharin et al. 2007; Wehner et al. 2010; Wehner 2013), rather simple statistical methods were used in this chapter and throughout this dissertation. The choice of simple statistical methods was made to eliminate the potential uncertainties resulting when making the necessary assumptions involved in more sophisticated statistical procedures (Kharin and Zwiers 2005; Wehner et al. 2010; Wehner 2013). Finally, the intent of this chapter is to evaluate the collective performance of the CMIP models and to see the range of model variability where appropriate, rather than to evaluate the individual performance of certain models. Therefore, the figures focus on the model average and the envelope of variability among the models, so the results from individual models are generally not displayed (with one exception). A detailed analysis of why certain models perform better than others requires a controlled experiment in which only certain model components are allowed to vary, which is not possible in the present analysis. Furthermore, it is very

difficult to identify one single climate model that outperforms all others at everything (Perkins et al. 2007); therefore, a ranking of the CMIP models may not be very insightful.

2.3 Precipitation statistics

The first metric which was evaluated in the CMIP3 models was the mean daily precipitation for the analysis period 1979-99 (Fig. 1). This analysis reveals that although the models generally capture the spatial patterns of mean precipitation fairly well, they tend to underestimate precipitation in wet areas and overestimate precipitation in dry areas. For example, the model average is drier than observations by as much as 5 mm day^{-1} along the Pacific Coast near 55°N during winter, where the climatological precipitation exceeds 10 mm day^{-1} (Figs. 1d,e). To the east of this area and extending a greater distance along the coast, the climatological winter precipitation is substantially lighter and the model average has wet biases of about 1-4 mm day^{-1} (Fig. 1e). Another example of substantial model dry biases over a relatively moist region is in southern Mexico and along the United States Gulf Coast, where the models are drier than observations by about 1-5 mm day^{-1} depending on location and season (Figs. 1b,e,h). The model biases in mean precipitation are consistent with those found in Iorio et al. (2004) over the contiguous United States using the National Center for Atmospheric Research (NCAR) Community Climate Model version 3 (CCM3) atmospheric general circulation model. Differences between the model average and observations are expressed as a percentage on the right column of Fig. 1 to assess how model biases scale with mean precipitation and for a more sensitive determination of the sign of model biases where the biases are small in magnitude. It appears that the model dry biases in

the south and along parts of the Pacific Coast are somewhat proportional to the CPC mean precipitation, as the percent biases mostly fall between -30% and -70% in these areas (Figs. 1c,f,i). Note that much of the large area of model wet biases across the northern and interior parts of the domain when expressed as a percentage is greatly exaggerated by the calculation method and very light climatological precipitation over this area. Over much of the northeastern part of the domain, where amount and percentage biases are both small, the models simulate mean precipitation quite well.

A similar analysis was performed for the mean precipitation that falls from just the wettest 1% of days (i.e., the mean precipitation coming from the daily 99^{th} percentile and above). This quantity (hereafter referred to as P99M) was chosen instead of the 99^{th} percentile itself because it is likely to be less spatially noisy and represents the average intensity of heavy to extreme precipitation. The results of this analysis are displayed in Fig. 2. The average performance of the CMIP3 models is noticeably poorer for P99M than it is for the mean precipitation. One particular area where model biases in P99M are disproportionately larger than those in mean precipitation is the southeastern United States and southern Mexico, where P99M is underestimated by more than 15 mm day^{-1} over much of the area (Figs. 2b,e,h). When expressed as a percentage, model dry biases over this area are larger for P99M than for mean precipitation, especially during summer and in southern Mexico (Figs. 1c,f,i, 2c,f,i). The model dry biases in P99M in the southeast United States also extend to higher latitudes during the summer season (Figs. 2e,f,h,i), more so than they do with mean precipitation (Figs. 1e,f,h,i). In general, model biases in P99M appear to be more negative over much of the domain when compared to mean precipitation biases. As was the case with mean precipitation, the model average

appears to do well generally east of 100°W and north of 40°N. Overall, the results shown in Fig. 2 are consistent with previous studies that used individual climate models and studied the contiguous United States (Iorio et al. 2004; Wehner et al. 2010).

To examine the intermodel variability of the biases in P99M, six regions within the North America study domain were chosen that approximately exhibit homogeneous characteristics of climatological precipitation as well as homogeneous CMIP3 model biases in mean and P99M precipitation (Fig. 3; note that all region names are explained in the caption). The P99M model biases were then averaged over each of these regions for each model and displayed on a box-and-whisker plot for all seasons (Fig. 4). The negative biases in P99M in the PCOAST and SEAST regions appear quite robust among the models, as more than 75% of the models show negative biases during all seasons over these regions (Figs. 4a,d). Indeed, all models analyzed show negative biases during fall in the PCOAST region and during both summer and fall in the SEAST region, suggesting that there is a systematic problem that results in too little heavy precipitation in these regions and seasons, a topic which will be discussed in section 2.4. Substantial and robust negative biases of about the same magnitude as those over the PCOAST region are also present over the SMEX region in winter and spring (Fig. 4f). The largest variability among the individual CMIP3 models occurs over SMEX in summer and fall, where a majority of the models have negative biases but the individual model biases range from -40 mm day^{-1} to more than 10 mm day^{-1} (Fig. 4f). There are also robust negative model biases in the SWEST region during summer, at a time when the North American monsoon brings heavy and convective rain over parts of this region (Fig. 4e). All CMIP3 models show a positive bias over the WINT region in winter (Fig. 4b), though this bias is

small in magnitude because of the light P99M precipitation over this region (Fig. 2d). The good performance of the CMIP3 models over the NEAST region is quite apparent during winter, where model biases straddle zero and have a small range of variability (Fig. 4c).

The regions defined in Fig. 3 were also used to analyze model biases over the entire daily precipitation distribution during the period 1979-99. For each grid point, daily precipitation percentiles in increments of 0.1 were computed from all days. The values of each percentile were averaged across the grid points in each of the six regions. This procedure was employed on the CPC data and the output from each of the CMIP3 models. The regional average values for each percentile from the CPC data were then paired with those from each of the CMIP3 models to form a set of quantitle-quantile (*Q*-*Q*) plots, a graphical approach for comparing distributions from two samples (Wilks 2006, 113–114). The *Q*-*Q* plots shown in Fig. 5 are constructed by comparing the minimum, median, and maximum CMIP3 model value for each percentile to the corresponding CPC value to depict the envelope of model performance for that region.

Despite the details of the precipitation distributions being somewhat different over each region, Fig. 5 shows that there are aspects of the model biases that are robust for all regions. The models tend to overestimate the intensity of light precipitation events, as seen by the model median rising above the 1:1 line at the low end of the precipitation distribution in every region. At the high end of the distribution, the opposite problem occurs, in which the models tend to underestimate the intensity of daily events to a degree which varies depending on the region. The intensity at which the model median transitions from overestimating to underestimating daily precipitation varies from as light

as 2-3 mm day^{-1} over the SEAST region (Fig. 5d), to as heavy as 20 or more mm day^{-1} for regions like NEAST and SWEST (Figs. 5c,e), depending on the severity of model biases in P99M precipitation (Figs. 2, 4). Numerous studies have found that climate models of varying spatial resolution and complexity have similar qualitative biases in daily precipitation distributions over Northern Hemisphere land regions (Sun et al. 2007), the United States (Gutowski et al. 2003; Iorio et al. 2004), Europe (Boberg et al. 2009), Australia (Perkins et al. 2007), and Japan (Kimoto et al. 2005). The result of climate models overestimating light precipitation and underestimating heavy precipitation is that they simulate relatively realistic mean precipitation, as shown in Fig. 1 and in earlier studies (e.g., Frei et al. 2003; Iorio et al. 2004; May 2004; Kimoto et al. 2005; Boroneant et al. 2006; Dulière et al. 2011). Potential reasons for the underestimation of heavy precipitation found in climate models are discussed in section 2.4.

To investigate the ability of the CMIP3 models to accurately simulate the seasonality of heavy precipitation events, the seasonal cycle of heavy precipitation was objectively quantified in CPC observations and CMIP3 models using harmonic analysis. More specifically, the P99M precipitation was computed separately for each calendar month over the period 1979-99 at each grid cell, resulting in a time series with 12 elements. Then, a one-period sinusoidal function (also known as the first harmonic) was fit to this 12 element time series using least-squares regression as described in Wilks (2006, 371–381). The resulting harmonic fit can be described with a phase representing the time of year of maximum P99M, and the percentage of total variance of monthly P99M that is explained by the harmonic fit, which is proportional to the relative strength

of the seasonal cycle of P99M. The phase is shown with vectors and percent variance with color fills in Fig. 6.

Figure 6 shows that on average, the CMIP3 models reasonably reproduce the observed seasonal patterns of heavy to extreme precipitation over most of North America, especially when considering the additional smoothing inherent in computing a multimodel average. In particular, the strong fall-to-winter maximum along the Pacific Coast, summer maximum in the northern-interior, and mid-to-late summer maximum in southern Mexico are simulated reasonably accurately by the models. The apparent disagreement between the CMIP3 model average and CPC observations in parts of northern Canada may be influenced by the sparseness of observations over this area (Chen et al. 2008c). More substantial disagreements between the CMIP3 simulated and observed seasonal cycle of P99M exist over the west coast of Mexico and the southeastern United States, where the models show a stronger and more widespread cool season maximum than is observed. Such biases may be the result of the models underpredicting P99M precipitation more severely during summer than winter in these regions (Figs. 2, 4). The models also simulate a pronounced winter maximum in P99M further inland along the Pacific Coast than is observed, which appears to be related to the overestimation of heavy winter precipitation in this region as a result of the coarse terrain representation in the models (Fig. 2). Ruiz-Barradas and Nigam (2006) used a harmonic analysis similar to the one presented here to evaluate the performance of a subset of CMIP3 models in simulating the seasonal cycle of mean precipitation over North America. While certain models in their analysis showed difficulty in simulating the correct timing and amplitude of the observed seasonal cycle over various places, the

models collectively captured the presence of a notable winter maximum along the Pacific Coast and summer maximum in central North America and southern Mexico, consistent with the results shown here.

2.4 Physical mechanisms associated with extreme precipitation

The large-scale physical mechanisms associated with extreme precipitation events were analyzed by developing composites of various atmospheric quantities during the most extreme precipitation events at each grid cell. To compute a composite for a grid cell, the dates of the heaviest 21 precipitation events were identified and an atmospheric quantity of interest was averaged over those 21 dates for the entire North America domain, resulting in a map showing the composite spatial structure of that quantity associated with an average extreme event at that grid cell. The number of events was chosen subjectively so that the smallest event would have a probability of occurring approximately once per year, as 21 years of data were used (1979-99). The 21st wettest event also represents approximately the 99th percentile (the basis of heavy precipitation statistics studied in this chapter) when drawn from a sample consisting of just winter (December-January-February, DJF) or summer (June-July-August, JJA) days. For observations, the CPC product was used to identify the 21 most extreme precipitation events at each grid cell while the NARR was used for the atmospheric quantities that were composited.

In some cases, the atmospheric quantities were first converted to a standardized anomaly at each grid cell before computing the composites, to eliminate the influence that model biases in the mean and variability of the atmospheric quantities would have on

the results. The standardized anomaly (or z-score) is defined as the anomaly divided by the standard deviation. The climatological mean and standard deviation were computed for a 21-day window centered on the original date (the date corresponding to each of the 21 extreme events) over all years from the period 1980-98. Defining the mean and standard deviation in this way allowed for the z-scores to represent anomalies that were with respect to a smoothly varying and seasonally dependent climatology (Hart and Grumm 2001).

As mentioned previously, only 12 CMIP3 models had available output of the variables needed for the composite analysis and therefore only these 12 models were analyzed (see Table 1). An analysis of biases in precipitation statistics using just these 12 models (not shown) led to the same conclusions as those presented in section 2.3 using all 17 models. Therefore, a direct comparison can be made between the precipitation analysis in section 2.3 and composite analysis shown here. When comparing composites between NARR and the model average, it should be noted that the model average is actually the composite of 252 extreme events (21 events from 12 different models) while the NARR is the composite of only 21 events. As a consequence of averaging across a larger number of events, the circulation features in the model average will be smoother than in NARR, and this must be taken into consideration when evaluating the realism of the simulated composites. Additionally, the composited quantities are shown over the entire North America domain for all analyzed grid cells in this section. The reader should note that only patterns of composited quantities that are relatively close to the analyzed grid cells (within ~1000 km) are likely to be associated with the extreme events at those

grid cells, and that patterns of composited quantities may be influenced by noise or climatology in distant areas.

To characterize the basic large-scale dynamical structure of the atmosphere, composites of pressure at mean sea level (hereafter PMSL) and geopotential height standardized anomalies at 500 mb (hereafter Z500*) were made for various North American grid cells (Figs. 7, 8, 10-12). The geopotential height was not available as a direct quantity from any of the CMIP3 models, therefore it was calculated by first computing surface pressure (a quantity that was also unavailable from the archived CMIP3 output) using the hydrostatic equation, then by using the hypsometric equation. Although the NARR outputs geopotential height directly, NARR geopotential height was computed in the same way as for the CMIP3 models for the sake of consistency. Differences between geopotential height directly output from NARR and that calculated with the same method as for the CMIP3 models were very small (not shown), suggesting that the method of calculation was satisfactory. The atmospheric levels which were available from the CMIP3 models and used in all computations involving multiple vertical levels were 1000, 925, 850, 700, 600, 500, 400, 300, and 200 mb, where levels below the surface were omitted.

The composites displayed in this section focus on grid cells where the CMIP3 models either showed substantial biases in P99M precipitation or where P99M precipitation was simulated quite well. A comparison of simulated and observed composites at these grid cells provides insight as to the physical problems with models that might be responsible for biases in heavy precipitation amounts. The first selection of grid cells includes locations where P99M precipitation is severely underestimated by the

models in both winter and summer: the Pacific Coast near 55°N, the southeast United States, and southern Mexico (Figs. 7-8). In comparing the winter composites of PMSL and Z500* between the NARR and model average, the models reasonably simulate the gross atmospheric circulation features associated with extreme events at these grid cells, especially when taking into account the additional smoothing in the model average (Fig. 7). However, the model average composites for the Pacific Coast and southern Mexico show stronger circulation features and larger gradients in PMSL and Z500* than is observed (Figs. 7b,f). Composites for a majority of the individual CMIP3 models at these grid cells look very similar to the model average composite, with only few models having stronger or weaker circulation features than the model mean (not shown). Thus, the model average composite for these cases does not appear to be influenced by individual outlier models and is a representative measure of how the bulk of the CMIP3 models perform. This is generally the case for all other grid cells shown in this paper where the model average appears to have biases in circulation features. Composites from different grid cells than the ones shown here within the Pacific Coast, southeast United States, and southern Mexico regions have the same characteristics as those shown in Fig. 7 (not shown). In the summer, the observed atmospheric circulation features associated with extreme precipitation at the same grid cells shown in Fig. 7 are much weaker (Figs. 8a,c,e). Furthermore, there is a minimum in Z500* located over or close to the grid cells at low latitudes, suggesting that atmospheric instability and moist convection are important mechanisms for extreme summer precipitation. As in the winter composites, the CMIP3 models reasonably capture the broad atmospheric patterns observed during

extreme summer events, with perhaps a slight overestimation of the strength of the circulation features (Figs. 8b,d,f).

Along the Pacific Coast, the CMIP3 models underestimate heavy winter precipitation yet the atmospheric circulation features associated with extreme precipitation events are slightly stronger than observed (Figs. 7a,b), suggesting that other physical deficiencies are present in the models. One likely deficiency is the oversimplified representation of topography by the coarse resolution models over this mountainous region, which leads to unrealistically light precipitation on the upwind side of mountains. Other studies have shown that climate models of varying spatial resolution and complexity underestimate extreme precipitation in places where it is orographically forced (Iorio et al. 2004; Semmler and Jacob 2004; Wehner et al. 2010), but that higher resolution simulations are more realistic (Colle and Mass 2000; Iorio et al. 2004; Wehner et al. 2010). Composites of vertically integrated water vapor flux (hereafter VIWVF) and the convergence of VIWVF (hereafter C(VIWVF)), two quantities which are highly relevant to the generation of extreme precipitation (e.g., Trenberth et al. 2003), were also produced for this grid cell (Figs. 9a,b). These composites support that deficiencies in CMIP3 orography are related to heavy precipitation underestimation at this location. In particular, the models underestimate C(VIWVF) over the center of strong convergence associated with extreme events while the magnitudes and orientation of VIWVF vectors are realistic to somewhat weaker than observed (Figs. 9a,b). Additional composite analyses reveal that an underestimation in vertically integrated water vapor itself (hereafter VIWV) and gradients in VIWV near the Pacific Coast are the primary cause for underestimations of VIWVF and C(VIWVF) (not shown). Such underestimations of

gradients in VIWV are likely a direct result of the oversimplified topography in the CMIP3 models.

In the southeast United States and Mexico, the underestimation of heavy precipitation despite realistic or overly strong circulation features during extreme events is possibly related to problems in simulating convective precipitation. This is supported by the dominance of convective precipitation in these regions, especially during summer (Changnon 2001; Dai 2001; Christian et al. 2003; Riemann-Campe et al. 2009), and the probable link between convective parameterizations and the underestimation of heavy precipitation in climate models (Gutowski et al. 2003; Iorio et al. 2004; May 2004; Emori et al. 2005; Kharin et al. 2007; Wilcox and Donner 2007; Wehner et al. 2010; Li et al. 2012). The northward migration of dry P99M model biases in summer (see Fig. 2) is also consistent with this explanation, as convective precipitation spreads north in summer (Changnon 2001; Dai 2001; Christian et al. 2003; Riemann-Campe et al. 2009), and simulated atmospheric circulation features during extreme summer events in the midwestern United States are also realistic (not shown). Because tropical cyclones are also an important mechanism for extreme precipitation at low latitudes near the Atlantic Ocean (Rappaport 2000; Lau et al. 2008; Kunkel et al. 2010; Kunkel et al. 2012), the underestimation of heavy precipitation in these regions is possibly also related to the inability of the coarse resolution CMIP3 models to accurately simulate tropical cyclones (Bengtsson et al. 1995; McClean et al. 2011; Manganello et al. 2012; Camargo 2013).

In some places, such as the western intermountain regions from Canada through Mexico, the CMIP3 models overestimate the intensity of P99M precipitation during winter (see Figs. 2 and 4). Winter composites of PMSL and Z500* for a selected grid

cell in the western United States show that the atmospheric circulation pattern associated with extreme winter events is simulated quite realistically by the CMIP3 models (Figs. 10a,b). This implies that the overestimation of heavy precipitation at this grid cell is mainly the result of the CMIP3 models oversimplifying the complex topography of western North America. That is, in places where observed precipitation is small because of subsidence on the lee side of mountains, the models simulate too much precipitation because the true terrain pattern is not accurately represented (Colle and Mass 2000). Composites of VIWVF and C(VIWVF) at this location indicate that the models overestimate C(VIWVF) during extreme winter events and that this overestimation is predominantly the result of underestimations in the divergence of low-level (10 m to 500 mb average) winds (not shown). It is possible that such deficiencies in the simulated wind divergence at this location are partly influenced by the unrealistic representation of topography.

In north-central Mexico, the observed atmospheric circulation during extreme winter events is characterized by a rather complex pattern in which surface winds originate from the Gulf of Mexico and anomalous mid tropospheric winds come from the Pacific Ocean (Fig. 10c). Although the CMIP3 models realistically simulate the main features of this pattern, they slightly overestimate the gradients in PMSL and Z500* (Fig. 10d). Model average composites of VIWVF and C(VIWVF) show substantial biases when compared to NARR for this location (Figs. 9c,d). The overestimations of VIWVF vectors stem from overestimations in low-level wind and VIWV itself, while overestimations in C(VWIVF) result from overestimations in the convergence of low-level wind (not shown). It is possible that the oversimplified representation of the

complex topography of Mexico in the models partly influences overestimations in the low-level wind convergence discussed above. However, given that circulation biases are also apparent with composites of PMSL and Z500*, it is likely that some fundamental large scale deficiency in the atmospheric dynamics is present in CMIP3 models during extreme precipitation events over this region.

Composites of PMSL and Z500* are also shown for locations where heavy to extreme precipitation is quantitatively realistic in the CMIP3 models to see if the atmospheric circulation during extreme events is simulated accurately in those places (Figs. 11-12). Two such locations are Newfoundland and northern Canada. The atmospheric circulation during extreme events over Newfoundland is qualitatively similar in winter and summer, although gradients of PMSL and Z500* are much weaker in summer (Figs. 11a, 12a). In both seasons, the CMIP3 model average overestimates the strength of the low PMSL associated with the circulation and places the low closer to the grid cell (Figs. 11b, 12b). In winter, the couplet of positive/negative Z500* is also shifted northeast in the models (Fig. 11b). Given that the models generate quite realistic P99M precipitation amounts over this region, it is possible that such errors in the circulation are compensated by other model deficiencies. Such deficiencies may stem from the inability of the models to resolve or accurately simulate some of the processes that generate extreme precipitation in the northeastern part of North America. These processes can include moist convection and tropical cyclones in the warm season (Dai 2001; Christian et al. 2003; Riemann-Campe et al. 2009; Kunkel et al. 2010; Kunkel et al. 2012; Manganello et al. 2012), mesoscale precipitation bands associated with extratropical cyclones (Novak et al. 2004), and other features of the synoptic atmospheric

structure that were not explored here (Milrad et al. 2010). The atmospheric circulation patterns during extreme events in northern Canada are interesting in that they appear to result in low-level moisture flow that originates from the Pacific Ocean in winter and Gulf of Mexico in summer (Figs. 11c, 12c). The model average captures this observed seasonal shift in moisture flow rather well, despite having a somewhat different arrangement of low and high PMSL centers in winter and somewhat stronger gradients of PMSL in summer (Figs. 11d, 12d). As was the case with Newfoundland, it is possible that small errors in the simulated circulation over northern Canada are compensated by other physical deficiencies in the models (discussed above) resulting in realistic P99M precipitation.

Composite patterns of low-level wind and standardized anomalies of vertically integrated water vapor (hereafter VIWV*) were computed for extreme winter and summer precipitation events at every grid cell on the North America domain. The values of low-level wind and VIWV* at the center grid cell for each of the composites was then displayed on a map of North America (Fig. 13). This analysis represents a summary of the atmospheric circulation and moisture anomalies associated with extreme events at every grid cell on the domain and is intended to provide a measure of CMIP3 model performance for grid cells that were not explicitly analyzed in Figs. 7-12. It should be noted that because only the local low-level wind associated with extreme events at each grid cell is displayed in Fig. 13, the wind vectors do not always indicate an oceanic moisture source. For instance, the moisture source for extreme winter precipitation events in the Midwestern United States includes both the Gulf of Mexico and western Caribbean, as seen in composites of VIWVF and C(VIWVF) for a Midwest grid cell

(Figs. 9e,f), despite local low-level winds being from the southwest (Figs. 13a,b). Nonetheless, the observed patterns of local wind and VIWV* during extreme events are not surprising: winds usually blow the from the south and/or a source of moisture when near the coast, there are positive VIWV* values across the domain, and there are much weaker local winds and VIWV* values during summer as a result of weaker and less organized circulation patterns (Figs. 13a,c). Many of the conclusions that were reached about the ability of CMIP3 models to simulate the observed circulation during extreme events from the analysis of individual grid cells can be seen in Fig. 13. That is, despite being able to reproduce the gross features, the models tend to overestimate the strength of the circulation associated with extreme events over some places. Figure 13 reveals that such overestimations in the circulation are largest along the entire Pacific Coast and much of northern and eastern Canada, where VIWV* values are also too high in the models. Over much of northeastern North America, the simulated direction of local wind during extreme events also has small errors (Figs. 13b,d), as was suggested by composites of PMSL and Z500* over Newfoundland (Figs. 11-12). Over many of these regions where the models have biases in simulated circulation, P99M precipitation is realistic or even underestimated, strengthening the point that errors in the simulated circulation during extreme events may be compensated by other physical deficiencies in the models.

In addition to the simple physical quantities shown in Figs. 7-13, other physical quantities were computed that further summarize the complexity of atmospheric circulation and thermodynamical patterns associated with extreme precipitation events. One such quantity is **Q**-vector convergence (hereafter QVC), a metric based on quasi-

geostrophic theory that quantifies the portion of upward vertical motion explained by synoptic and meso-α-scale forcing (i.e., warm air advection, positive vorticity advection, and large-scale frontogenesis) (Hoskins et al. 1978). Quantitatively, the **Q**-vector can be computed with gradients in geopotential height and temperature at a given atmospheric level (Holton 2004, 168–174). Composites of QVC averaged over the lower troposphere (850, 700, and 600 mb) were analyzed for extreme winter and summer precipitation across the North America domain. The analysis revealed that the CMIP3 models accurately capture the features of QVC associated with extreme events but overestimate the magnitudes of QVC in regions where the large scale circulation is also overestimated, particularly the northeastern part of the domain (not shown). Such results are consistent with those presented in Figs. 7-13. The lifted index, a quantity that approximately characterizes the atmospheric static stability and thus potential for convective precipitation, was also composited during extreme events. This analysis showed that while the magnitudes of lifted index were sometimes underestimated by the models, patterns of standardized anomalies of lifted index were quite realistic over most of the domain (not shown). This implies that the anomalous thermodynamical structure of the atmosphere during extreme events, partly driven by the large scale circulation, is simulated well by the CMIP3 models.

2.5 A comparison of CMIP3 with CMIP5

In this section, an analysis that was performed for the CMIP5 ensemble analogous to that shown in sections 2.3-2.4 will be highlighted. Daily output from CMIP5 was obtained from the Earth System Grid Federation archive [http://pcmdi9.llnl.gov/esgf-

web-fe/]. There were 17 models with archived variables necessary for the evaluation of both precipitation statistics and the physical mechanisms associated with extreme precipitation events (Table 2). The models listed in Table 2 are those with available output by 1 July 2012. Models that became available after that date are excluded, though various sensitivity tests involving different CMIP5 model subsets suggest that including those additional models would not substantially alter the conclusions (not shown). The historical scenario from CMIP5 was used for the evaluation. The historical scenario, which is analogous to the 20th century scenario in CMIP3, is forced with observed changes in atmospheric composition (due to natural and anthropogenic sources), solar forcing, and land use (Taylor et al. 2009; Taylor et al. 2012). The first available ensemble member run from each CMIP5 model was analyzed. The time period 1 January 1979- 31 December 1999 was evaluated in CMIP5 and all CMIP5 output was regridded from its original horizontal resolution to a common 2.5°x2.5° resolution, following the same procedure as for CMIP3 (see section 2.2.c). Leap days (29 February) were removed from all CMIP5 output. In the figures showing CMIP3 in this section (Figs. 14-17), only the 12 CMIP3 models with necessary output for the evaluation of both precipitation statistics and physical mechanisms are used (see Table 1).

The spatial pattern of annual heavy precipitation (P99M) over North America is compared between the CPC observations and the CMIP3 and CMIP5 multimodel averages in Fig. 14. CMIP3 and CMIP5 exhibit the same general biases in annual P99M across much of the domain, including underestimations in the southeastern United States, southern Mexico, and along the Pacific Coast, and overestimations across the intermountain regions of the west extending into central Mexico (Fig. 14). The

underestimation in P99M in the southeast United States in CMIP5 is somewhat smaller than in CMIP3, both in spatial extent and magnitude. Improvements in CMIP5 over CMIP3 are also seen in the southeastern United States when considering winter (DJF) and summer (JJA) P99M (not shown). The spatial extent of the overestimation in annual heavy precipitation in the western intermountain regions in CMIP5 is somewhat larger than in CMIP3 (Fig. 14). The differences between CMIP3 and CMIP5 in Fig. 14 are not sensitive to the subset of CMIP3 and CMIP5 models used in computing P99M biases (i.e., when including more models from each ensemble that have available precipitation output, or when just using models from the same modeling groups from each ensemble) (not shown). In a recent evaluation, Sillmann et al. (2013a) found similar biases in CMIP5 precipitation over North America when compared to HadEX2 observations for precipitation indices such as total rainfall from days exceeding the 95th percentile and the maximum five-day precipitation amount. They also found that the intensity of heavy precipitation in CMIP5 is somewhat higher and therefore more realistic than CMIP3 over regions such as central and eastern North America, consistent with the results shown here. Biases in climatological mean precipitation are very similar between the CMIP3 and CMIP5 ensembles (not shown).

It is interesting to assess the degree to which horizontal resolution influences the performance of CMIP3 and CMIP5 models in simulating heavy precipitation over North America, as CMIP5 models generally have higher resolution than CMIP3 models (Tables 1-2). As discussed in section 1, higher resolution models tend to simulate the statistics of high frequency precipitation more realistically (e.g., Iorio et al. 2004; Wehner et al. 2010; Dulière et al. 2011; Li et al. 2011). To objectively evaluate the performance of the

individual models, the root-mean-square (RMS) of the difference in P99M between each model and the CPC observations (both datasets on the 2.5°x2.5° grid) was computed over all grid cells over North America. In Fig. 15, the RMS error value versus corresponding native horizontal resolution (expressed as total number of grid cells globally) for each model is plotted, along with statistics of the linear relationship, to provide a general assessment of the influence of resolution on model biases. Despite the rather wide scatter in performance among the individual models, there is a general tendency for the higher resolution models to have smaller RMS error, especially for annual and summer (JJA) P99M, with R^2 values of about 0.3 (Figs. 15a,c). The wide scatter in model performance is expected as the CMIP ensembles include a diverse group of models with many physical differences in addition to horizontal resolution, including convective parameterizations. When using winter (DJF) data, the relationship between RMS error and horizontal resolution is noticeably weaker, with R^2 values dropping below 0.1 (Fig. 15b). The more pronounced improvement in model performance with increased resolution during summer, a time when convective precipitation is prevalent over North America, may reflect the reduced dependence of the higher resolution simulations on convective parameterizations (Li et al. 2011, Li et al. 2012).

The composite analysis shown in section 2.4 and in Figs. 7-13 was repeated for CMIP5, focusing on annual heavy precipitation (i.e., including all seasons). In producing the composite maps for NARR, CMIP3, and CMIP5 in this section, atmospheric quantities were averaged over the days when precipitation equals or exceeds the 99th percentile at a grid cell. This allows for a direct comparison with biases in annual P99M in Fig. 14. Fewer atmospheric levels were available from the CMIP5 archive (1000, 850,

700, 500, 250 mb) for the computation of variables such as Z500 and low-level wind. For a consistent comparison among datasets, Z500 and low-level wind in NARR and CMIP3 were computed using the available CMIP5 levels.

Composites of PMSL and Z500* were produced for selected grid cells where the biases in P99M between CMIP3 and CMIP5 have different magnitudes and/or spatial extent, such as the southeastern United States, southwestern United States, and central Mexico (see Fig. 14). Overall, the atmospheric circulation patterns during heavy annual precipitation days are very similar between the CMIP3 and CMIP5 multimodel means at these locations (Fig. 16). Over the southeastern United States, where both CMIP3 and CMIP5 underestimate intense precipitation (more so in CMIP3), the atmospheric circulation patterns in both CMIP3 and CMIP5 agree reasonably well with observations (Figs. 16a-c). Over the southwestern United States where CMIP5 overestimates P99M slightly more than CMIP3 (Fig 14), the minima in Z500* associated with extreme events in both CMIP3 and CMIP5 are slightly weaker than observed while the PMSL pattern is simulated well (Figs. 16d-f). Finally, both CMIP3 and CMIP5 show circulation features characterized by stronger gradients in PMSL and stronger Z500* minima than observed over a grid cell in Mexico where CMIP5 overestimates heavy precipitation slightly more than CMIP3 (Figs. 16g-i).

To perform a more comprehensive comparison of the simulated atmospheric circulation associated with heavy precipitation between NARR, CMIP3 and CMIP5 at all grid cells, the local low-level (10-m to 500-mb mean) wind averaged over days when the daily precipitation equals or exceeds the annual 99^{th} percentile is plotted in Fig. 17. Fig. 17 is analogous to Fig. 13, except it only shows low-level wind and is computed from all

seasons. Both CMIP3 and CMIP5 models overestimate the strength of the local low-level winds inland of the Pacific Coast and have somewhat more southerly local winds during heavy precipitation in northeastern Canada when compared to NARR (Fig. 17). The generally realistic simulation of the atmospheric circulation by the CMIP3 and CMIP5 models in much of the eastern United States is in agreement with a more comprehensive evaluation of the physical mechanisms associated with extreme precipitation over the Midwest United States in CMIP5 models by Kawazoe and Gutowksi (2013). Overall, CMIP3 and CMIP5 are very similar in their simulation of the local low-level wind associated with heavy precipitation, consistent with the composite analysis of individual grid cells in Fig. 16 which showed minor differences in the large-scale circulation between CMIP3 and CMIP5.

The differences between the observed and simulated atmospheric circulation features in Figs. 16-17 suggest that there is no simple relationship between biases in atmospheric circulation and heavy precipitation in CMIP3 or CMIP5, as can also be concluded from the CMIP3 analysis in sections 2.3 and 2.4. Furthermore, improvements in CMIP5 over CMIP3 in simulating heavy precipitation, particularly over the southeastern United States, do not appear to be strongly related the simulation of the large-scale atmospheric circulation patterns during extreme events. Horizontal resolution and other physical processes in the models, including the parameterization of convective precipitation, may be more important for such improvements (e.g., Fig. 15; Iorio et al. 2004; Wilcox and Donner 2007; Wehner et al. 2010).

2.6 Concluding remarks

The models participating in CMIP3 and CMIP5 show robust biases in their simulation of daily precipitation statistics over North America, most notably underestimations in the intensity of heavy precipitation over certain regions, including the southeastern United States, southern Mexico, and Pacific Coast. Despite biases in precipitation intensity, the gross features of the large-scale atmospheric circulation associated with heavy to extreme precipitation events are realistic over most places. The ability of the models to realistically simulate the large-scale mechanisms accompanying heavy precipitation provides confidence in their use to understand projected changes in precipitation in a future climate, at least from a qualitative perspective. Given their biases in precipitation intensity and based on conclusions from previous studies, however, climate models may underestimate future increases in heavy precipitation. In the subsequent two chapters, CMIP5 models are used to examine projected changes in the daily precipitation distribution and to better understand the physical mechanisms for changes in regional heavy precipitation.

3. Projected changes in the daily precipitation distribution in CMIP5

3.1 Introduction

In this chapter, CMIP5 models are used to examine projected changes in the frequency distribution of daily precipitation in response to future global warming. The study domain is expanded to the entire globe for this analysis. A focus is on the regional variability of projected changes, which has not been comprehensively explored in previous studies. To explore the regional variability, cluster analysis is applied to difference histograms of daily precipitation at all grid cells. The CMIP5 output and methodology are described in section 3.2. The main results of the analysis are presented and discussed in section 3.3. In section 3.4, the potential physical mechanisms for regional changes in the precipitation distribution are explored with additional analyses and a literature review. Finally, in section 3.5, a discussion of the broader impacts and limitations of the analysis is provided.

3.2 Data and methodology

3.2.a CMIP5 output

The same CMIP5 models and runs that were used to evaluate the climate of the late 20th century (section 2.5, Table 2) were used in all analyses of future climate in this dissertation (chapters 3 and 4). The RCP8.5 scenario, a high emissions scenario in which the radiative forcing reaches approximately 8.5 W m^{-2} by the end of the 21st century (Moss et al. 2010; Taylor et al. 2012), is used to represent future climate. The RCP8.5

scenario is compared with the historical scenario described in section 2.5. The time period 1 January 1979- 31 December 1999 is used from the historical scenario and 1 January 2079- 31 December 2099 from the RCP8.5 scenario. Using longer time periods (1960-99 and 2060-99) does not change the main findings emerging from the comparison of historical and future climate (not shown). The same methodology applied to the historical output, including the regridding to a 2.5°x2.5° longitude-latitude grid and the removal of leap days, was also applied to the RCP8.5 output.

3.2.b Cluster analysis

To analyze regional changes in the annual distribution of daily precipitation between the historical and RCP8.5 scenarios of the CMIP5 models, k-means cluster analysis is applied to difference histograms of daily precipitation. More specifically, a histogram of daily precipitation at each grid cell and for each model is computed for both the historical and RCP8.5 simulations using days from all seasons. The historical histogram is then subtracted from the RCP8.5 histogram to obtain the difference histogram at all grid cells for each model. In constructing the histograms, different normalizations applied to the raw daily precipitation before counting over bins were explored. In the simplest case, precipitation is binned based on raw amount, where the first bin is 0 to 0.5 mm day^{-1} representing zero or trace precipitation (hereafter zero/trace), the second is 0.5 to 2.5 mm day^{-1} (hereafter very light) and subsequent bins have a 2.5 mm day^{-1} width, with the heaviest bin being 122.5-125 mm day^{-1}. When binning precipitation based on raw amount, drier grid cells may not have counts in heavier bins, potentially creating a bias in the assignment of clusters to those grid cells.

For this reason, it is useful to normalize the daily precipitation by some measure of the local mean precipitation intensity before generating histograms. The historical P99M (defined in section 2.3) was shown to be a sufficient measure of the local precipitation intensity and is used for the normalization in this chapter. When normalizing by P99M, the first bin representing zero/trace is 0 to 0.01, the second bin is 0.01 to 0.1, and remaining bins have a width of 0.1 up to 2, with the largest bin being greater than or equal to 2 (i.e., larger than twice the local historical P99M). While the normalization has the advantage of removing the influence of climatological precipitation when assigning clusters, it masks information about the actual intensity of precipitation which may be related to the physical mechanisms responsible for precipitation changes (Lau et al. 2013). Therefore, cluster analysis is applied to histograms generated from both normalized and non-normalized precipitation in this chapter and the results are shown for both.

There is large spatial variability in the raw count differences (RCP8.5 – historical) for certain precipitation bins, partially as a result of climatological mean precipitation, and the clustering algorithm is very sensitive to this (not shown). Furthermore, due to the positively skewed character of daily precipitation distributions, the lighter bins always have larger count differences than the heavier bins, giving more weight to the lighter bins when assigning clusters. To assign clusters based on the shape of precipitation change histograms regardless of the magnitude of count changes and to represent light and heavy events with more equality, the log (base 10) is applied to the count differences before performing the cluster analysis. Note that for negative count differences, the log is applied to the absolute value of the count difference and the negative sign reapplied after.

Taking the log has the effect of both reducing the spatial variability in the range of count differences (allowing grid cells with similarly shaped histograms to appear more similar to the cluster algorithm) and giving more weight to heavier precipitation bins.

K-means clustering is applied to the difference histograms at the individual grid cells for either 1) the model average histograms, where the histograms at every grid cell were first averaged over the 17 available models and the log of count differences was applied after averaging, or 2) the aggregate of histograms at all grid cells and every individual model, where the model average (case 1) is treated as a separate "model." In the latter, the cluster analysis takes into account histogram data at each grid cell for every model simultaneously and assigns one of *k* clusters to each grid cell of every model. Applying cluster analysis to the aggregate of grid cells from all models allows for an assessment of the intermodel variability in precipitation change behavior. In all cases, the clustering algorithm works by assigning each *n*-bin histogram at every grid cell to one of *k* centroid histograms (also referred to as clusters), where the centroid histogram is the linear mean of the histograms over the grid cells assigned to that cluster. Each grid cell is assigned to the centroid histogram with the smallest *n*-dimensional distance from the grid cell histogram, where distance is defined as the sum (over all *n* bins) of the squared differences between the grid cell and centroid histogram bin counts. This distance may also be referred to as the squared Euclidean distance, with units of squared $\log_{10}(count\ differences)$ in this analysis.

3.2.c V-fold cross validation

When applying cluster analysis, one must choose an appropriate number of clusters that effectively summarizes the data put under analysis. One objective method to evaluate an appropriate number of clusters is based on V-fold cross validation (Hill and Lewicki 2006, 123–126). In this process, the original dataset that is to undergo cluster analysis (in this case, precipitation change histograms at individual grid cells) is split into *V* equal sized samples, where the splitting is applied along the grid cell dimension. Leaving out one of the *V* subsamples, cluster analysis is applied to the remaining *V*-1 subsamples using a fixed number of clusters. The centroids obtained by the application of cluster analysis to the *V*-1 subsamples are then used to predict the appropriate cluster for the grid cells in the left-out sample (i.e., by assigning the centroid histogram with the smallest distance from the grid cell histogram to that grid cell). The procedure is performed *V* times, each time leaving out one of the *V* subsamples. The distance between the left-out grid cell histograms and the corresponding predicted centroid histograms is then averaged over all grid cells in each left-out subsample and then over the *V* subsamples, giving a metric of the error for the assignment of centroid histograms for a particular number of clusters. The process is then repeated using different numbers of clusters, ultimately resulting in a relationship between error in predictability and number of clusters. The point at which reductions in predictability error with increased cluster number become insignificant determines an appropriate number of clusters for the dataset. For example, if significant reductions in error are seen when increasing the number of clusters to 2 and 3, but error begins leveling off at 4 or more clusters, an appropriate number of clusters might be 3 or 4. There remains some subjectivity in determining the point of diminishing returns with increased number of clusters.

Fig. 18 shows the results of applying the V-fold cross validation procedure to histograms of count differences in raw precipitation as well as precipitation normalized by historical P99M. V=5 is used for the analysis, but the results are nearly identical for different values of V ranging from 3 to 15 (not shown). The average error when applying the analysis to the aggregate of grid cells over all models is larger than when applied to the model average grid cells alone (Fig. 18). This is expected due to the inherently larger variability between grid cell histograms when considering many different models. When the analysis is applied to raw precipitation, average error is slightly larger than when applied to normalized precipitation, suggesting that the normalization reduces some of the inter-grid cell variability resulting from climatological precipitation, improving the predictions. In all cases, there is a fairly large drop in average error when going from one to two clusters, with progressively smaller reductions in error when continuing to add clusters, especially in the case of the multimodel average (circles in Fig. 18). Based on the results of the V-fold cross validation and inspection of the results of cluster analysis when using a varying number of clusters ranging from two to eight, four clusters was chosen to adequately represent the spatial variability in difference histograms in the CMIP5 output. The physical insight gained from using more than four clusters does not appear to be substantial. Furthermore, using fewer clusters makes the geographical pattern of cluster assignments easier to visualize and interpret. Nonetheless, a drawback of using few clusters is that more individual grid cells will not neatly fit into one of the clusters, a topic which will be further investigated in section 3.3.b.

3.3 Results

3.3.a Spatial patterns of mean and heavy precipitation

As an introduction and for future reference throughout this dissertation, the climatological patterns and projected changes in mean and heavy precipitation in CMIP5 are shown in Figs. 19-20. Increases in mean precipitation between the historical and RCP8.5 simulations are largest in magnitude in the tropics, where climatological precipitation in the historical simulation is also largest (Fig. 19). In some places, such as the equatorial Pacific, increases in precipitation appear to be influenced by subtle redistributions in the spatial precipitation pattern. Such redistributions may be related to changes in tropical mean circulation, such as the Walker circulation (Vecchi and Soden 2007; Chou et al. 2009), a topic which is further discussed in section 3.4. Precipitation also increases in most middle to high-latitude regions, especially during the local winter season. Decreases in mean precipitation, both in amount and percentage, occur over dry subtropical oceanic regions, such as the eastern North and South Pacific, tropical North Atlantic, eastern South Atlantic, and eastern Indian Ocean. Precipitation also decreases, with seasonal variability, over some land regions, including Central America and northern Africa during DJF and the Caribbean, eastern South America, the Mediterranean region, southern Africa, and Australia during JJA. The seasonal decreases in mean precipitation over land occur over dry regions and are more apparent when viewing the changes as a percentage (Figs. 19g-i). Changes in mean precipitation in CMIP5 models are broadly consistent with earlier CMIP3 studies showing wet places becoming wetter and dry places becoming dryer in a future warmer climate (e.g., Held and Soden 2006; Vecchi and Soden 2007; Seager et al. 2010).

The picture is quite different when looking at projected changes in mean precipitation from the heaviest 1% of daily events (P99M, Fig. 20). Projected increases in P99M are dominant across the global domain, which is especially apparent when the changes are expressed as a percentage (Figs. 20g-i). The largest relative increases are once again in the tropics and high latitudes. In some places and seasons, such as Central America and the Pacific Coast of North America during boreal summer (JJA) and the western North Pacific during boreal winter (DJF), climatological mean precipitation decreases while heavy precipitation increases (Figs. 19h,i, 20h,i). Areas of substantial projected decreases in heavy precipitation are apparent, especially in subtropical oceanic regions; however, these decreases are notably smaller in spatial extent than the corresponding decreases in climatological mean precipitation over the same areas. The regions and seasons characterized by rather large percentage decreases in heavy precipitation, including some land regions in South America and Africa, are mostly those in which P99M is very light in the historical simulation. One interesting exception is over northern Australia and the adjacent Indian Ocean where P99M decreases during austral winter (JJA) and historical P99M is substantial (Fig. 20c,f,i). The results in Figs. 19-20 are in agreement with previous observational and climate model studies showing disproportionate increases in heavy precipitation relative to mean precipitation (e.g., Easterling et al. 2000; Allen and Ingram 2002; Groisman et al. 2005; Kharin and Zwiers 2005; Kharin et al. 2007; Sun et al. 2007; Liu et al. 2009; Kharin et al. 2013; Scoccimarro et al. 2013; Sillman et al. 2013b). These projected changes imply a shift in the daily precipitation distribution characterized by an increase in both dry and heavy precipitation frequency at the expense of light-moderate precipitation over many places.

3.3.b Analysis of daily precipitation distributions

Fig. 21 shows the results of applying k-means cluster analysis to the multimodel average histograms using raw annual precipitation bins (see section 3.2.b for details). There are two distinct types of centroid histograms that emerge from the analysis: 1) the lightest precipitation bin(s) show decreasing counts while all larger events increase (clusters 1 and 2, hereafter referred to as down-up), and 2) zero/trace and heavy precipitation increases at the expense of light-moderate precipitation (clusters 3 and 4, hereafter referred to as up-down-up). The former occurs in high-latitude regions as well as parts of the tropics, while the latter primarily occurs in midlatitude and subtropical regions (Fig. 21c). When using four clusters, each of these main histogram types is further split into two subtypes. For the down-up type, the main distinction between clusters 1 and 2 is that the very light (second) bin also has decreasing counts in cluster 2 (Figs. 21a,b). Cluster 2 mainly occurs in the oceanic tropical regions and over the lower latitude and climatologically wetter parts of the broad high-latitude regions assigned the down-up type. Clusters 3 and 4 are different in that the transition from decreasing to increasing counts occurs at a heavier intensity in cluster 4 (Fig. 21d,e). The increases in the heavy tail in cluster 4 are also reduced compared to cluster 3, implying that many individual grid cells assigned this cluster have little change or count decreases in the heavy bins. Cluster 4 is generally more prevalent at lower latitudes within the broad up-down-up region, with no clear relationship to the climatological precipitation (Figs. 19a, 21c).

In Fig. 22, precipitation is first normalized by the local historical P99M before generating histograms and applying cluster analysis (as described in section 3.2.b). Though the results are similar to those using non-normalized precipitation, there are differences worth noting. One is that cluster # 1 is less prevalent over Antarctica and the northern high latitudes when precipitation is normalized. This may be the result of the zero/trace bin not being capped with a fixed threshold such as 0.5 mm day^{-1} but rather $1/100^{th}$ of the local P99M. At the highest latitude locations, the normalized threshold may be less than 0.5 mm day^{-1}, resulting in more precipitation and larger count differences in the second bin than would otherwise occur, hence the assignment of cluster 2. A more notable difference is that cluster 4 is dominated by decreases in heavy precipitation and better centered over drier regions with projected decreases in mean and heavy precipitation when precipitation is first normalized by P99M (Figs. 19a,g, 20a,g, 21c, 22c). Thus, the normalization has the effect of better separating grid cells with a distinct difference in the response of the heavy tail of the distribution. For this reason, precipitation normalized by P99M is used for the rest of the analyses in this chapter.

When comparing patterns of mean precipitation change with the cluster assignments in Figs. 21-22, it is apparent that the areas assigned the down-up clusters are those in which mean precipitation is projected to increase in the future (Figs. 19d,g, 21c, 22c). Likewise, areas assigned the up-down-up clusters are those in which changes in mean precipitation are small or negative. This relationship is partly expected, since most regions projected to have little change or decreases in mean precipitation also have projected increases in heavy precipitation (Figs. 19, 20), implying an up-down-up shift in the daily precipitation distribution as discussed in section 1.3. It is noteworthy though

that over areas with a projected increase in mean precipitation, the precipitation increases because zero/trace or very light precipitation days are replaced with more substantial precipitation days. In these areas, increases in mean precipitation are not dominated by increases in the heavy tail of the precipitation distribution that are partly compensated by decreases in light-moderate events and more frequent dry days. Rather, mean precipitation is increasing because of more frequent and more intense precipitation events of all intensities. The same can be said for regions of substantial mean precipitation decreases, in which precipitation of all intensities is less frequent in the future (seen later). In summary, changes in mean precipitation, especially when expressed as a percentage, are a very good indicator of regional changes in the daily precipitation distribution despite regional differences in climatological precipitation.

In both Figs. 21 and 22, metrics of grid cell variability within cluster groupings are shown on the histograms. The inter-quartile range (IQR) of count differences across histograms assigned to the same cluster generally do not deviate from the shape of the centroid histogram, demonstrating that the sign of the mean count difference at a particular bin is representative of at least 75% of the assigned grid cells. In some cases, the IQR of count differences spans zero, most notably for the transition bins in the up-down-up clusters. Indeed, the wide spread of count differences in the second bin of cluster 4 implies that a decrease in precipitation at the heavy tail (esp. when normalized by P99M) is often associated with an increase in not only zero/trace days, but also days with very light precipitation (Figs. 21e, 22e). Additionally, the zero-spanning IQR in the heavy bins in cluster 4 shows that many grid cells assigned this cluster do indeed have count increases in heavy precipitation. The 5^{th} to 95^{th} percentile spread of count

differences is also shown in Figs. 21-22 and like the IQR, it broadly follows the shape of the mean histograms, but with a larger spread. However, the full range of count differences is very large in all cases, suggesting that some individual locations show very different behavior from any the four clusters.

The spatial pattern of differences between local and assigned centroid histograms is further investigated to get a better idea of where the local precipitation response is very different from the four clusters of Figs. 21-22. In Fig. 23, the distance between the histogram at each grid cell and its assigned centroid histogram from Fig. 22 (i.e., using precipitation normalized by P99M) is shown. Recall that distance is defined as the sum, over all bins, of the squared differences between centroid and local histogram bin counts and has units of squared $\log_{10}(count\ differences)$. Over much of the geographical areas assigned to a particular cluster, the distances are relatively small compared to the full range of distances across the map (Figs. 23a,c,e,g). Areas with large distances tend to be isolated or confined to small regions and generally occur in the lower latitudes. The graphs in Fig. 23 (right column) show the variability in count differences among grid cells with a distance of less than 10 from their assigned cluster, where a distance of 10 is arbitrarily chosen to represent the threshold of close agreement with the centroid histogram. Though the full range of count differences is still large, the 5^{th} to 95^{th} percentile spread is very closely confined to the centroid histogram shape when considering just these locations, more so than when considering all locations assigned the cluster (compare Figs. 22a,b,d,e with Figs. 23b,d,f,h). This implies that the general behavior in the precipitation distribution at locations with small distance, which constitute a majority of the domain and coherent geographical regions, can be predicted

to a large extent by the mean centroid histograms. Similar conclusions can be drawn when the analysis of Fig. 23 is repeated using raw precipitation, but with the 5^{th} to 95^{th} percentile spread more frequently hitting zero in heavier bins, most likely due to the lack of counts in heavy bins at dry locations (not shown).

To further explore the behavior of precipitation change at grid cells with large differences from their assigned cluster, grid cells with a distance of 10 or more from their respective cluster in Fig. 22 (shown in Fig. 23) are subjected to a new k-means cluster analysis (Fig. 24). A notable feature that emerges in the new cluster assignments is a mean histogram type characterized by a down-up-down-up shape, which occurs in scattered tropical regions (Figs. 23a,c). While the spread among individual grid cell histograms assigned this cluster is large, an inspection of individual grid cells and those with distances less than 5 from this cluster indicates that the initial down-up-down behavior is robust, particularly in the oceanic regions of the West Pacific, North Atlantic, and Indian Ocean (not shown). Thus, this behavior is not an artifact of averaging over many grid cells and indeed occurs at individual locations. When using six or more clusters in the original analysis of all grid cells for raw or normalized precipitation, the same down-up-down-up cluster emerges in the same regions, consistent with Fig. 24 (not shown). Cluster 2 of Fig. 24 is a hybrid of the down-up and up-down-up types and occurs at the boundaries of these types in the original analysis (Figs. 22c, 24c). Cluster 3 represents a slight deviation from the original up-down-up cluster of Fig. 22 reflecting variability in the transition bins. Cluster 4 shows a larger magnitude and more robust decrease in the heavy tail of the distribution than was found when using all grid cells, occurring near subtropical oceanic areas with projected decreases in both mean and

P99M precipitation (Figs. 19g, 20g, 24c). Indeed, when considering all locations with decreases in both mean and heavy precipitation, the up-down response of the daily precipitation distribution is quite robust (Fig. 25). Thus, an up-down change of the daily precipitation distribution is another distinct type of precipitation response in the CMIP5 ensemble, which primarily occurs in subtropical subsidence regions.

The remaining scatter in precipitation behavior at individual grid cells (represented by the stars in Figs. 21-25) highlights the inherently noisy nature of precipitation and potentially complicated local mechanisms at play when considering precipitation change. Inadequate sampling when constructing precipitation histograms may also contribute to the scatter in the precipitation distribution at some locations. To test this, the analysis of Fig. 22 was repeated using 40-year periods (1960-99 and 2060-99) instead of 21-year periods. While the results were generally the same, the grid cell scatter in precipitation response was somewhat reduced for the up-down-up cluster # 3 when using the longer time periods (not shown).

Up until this point the analysis has focused on k-means cluster analysis applied to difference histograms that were first averaged over the individual 17 CMIP5 models. Now, the intermodel variability is explored by combining the histograms from every grid cell and every model into one sample and then applying cluster analysis, as described in section 3.2.b. The results of this analysis when using normalized precipitation are shown in Figs. 26-27. The pattern of cluster assignments for the multimodel average component of the aggregate and shapes of the four emerging histograms are qualitatively similar to those when applying cluster analysis to the multimodel average (Figs. 22, 26, 27). This is an indication that the precipitation distribution response of the multimodel mean is

representative of that of the individual models, as the results are not substantially altered by the inclusion of individual models. Furthermore, the pattern of cluster assignments for each of the individual models in Fig. 26 is broadly consistent with that for the multimodel average in Fig. 22. That is, the down-up response generally occurs in the tropics and high latitudes, while the up-down-up response occurs elsewhere. There is, however, a fair degree of intermodel variability in the geographical placement and spatial extent of certain clusters (e.g., cluster 3 dominates in the MPI-ESM-LR, MPI-ESM-MR, and MRI-CGCM3 models, while cluster 4 dominates in the GFDL-ESM2G and GFDL-ESM2M models). These differences in cluster assignments between individual models are likely related to different patterns and magnitudes of the mean precipitation response.

Though the spatial pattern of changes in the daily precipitation distribution is variable among individual models (Fig. 26), it is possible that the models agree better when considering large-scale regional averages (e.g., Chou et al. 2009). To test this, regions are defined based on the cluster assignments determined from the analysis in Fig. 22 (i.e., using normalized precipitation) and the mean difference histogram over each region is computed for each individual model (Fig. 28). The full model range of regional-mean count differences closely follows the centroid histogram shapes of Fig. 22, with the exception of transition and zero/tace bins in some cases (Figs. 22, 28). This suggests that although the individual models have variable spatial patterns of precipitation response, when averaged over large regions, the response of the daily precipitation distribution is fairly robust. About half of the models show a small increase in the heavy tail of the daily precipitation distribution when averaged over region 4 in Fig. 28. However, when averaged over the smaller regions better centered over the

subtropical subsidence regions (Fig. 29c, region 4), almost all models show decreases in the heavy bins (Fig. 29e). Similar results are obtained when averaging over the regions in Fig. 25a (not shown). The down-up-down-up response that emerges in the cluster analysis of the multimodel mean over small regions (Figs. 24a,c) is not at all robust across the individual models when averaged over these regions (Fig. 29a), suggesting that this response occurs at only scattered locations in some individual models.

3.3.c Summary of main histogram types

From the analysis of k-means clustering applied to difference histograms of daily precipitation, four distinct responses of the precipitation distribution emerge, which are summarized in Table 3. These responses appear not only when averaging precipitation histograms over many grid cells but also occur at individual locations with fairly high robustness (e.g., Fig. 23). When averaged over the broad regions that make up each of the main histogram types in Table 3, the precipitation response is fairly consistent across the 17 individual models used in the analysis (Figs. 28-29). A notable exception is for the down-up-down-up response, which may not be physically robust.

In previous studies that focus on large regions, the main response of the precipitation distribution to warming is shown to have an up-down-up shape. The analyses in this chapter show that other responses of the daily precipitation distribution to warming are also important regionally, including shifts toward generally wetter (down-up) and drier (up-down) conditions in the future.

3.4 Physical mechanisms associated with precipitation change

In this section, the physical mechanisms that may be responsible for the projected changes in the precipitation distribution are explored. One interesting finding from the cluster analyses in this chapter is that the down-up response of the precipitation distribution, representing a shift toward generally wetter conditions, occurs in both high latitudes and the tropics, two regions with very different climates and physical processes relevant to precipitation. In the tropics, a mechanism that may be responsible for the precipitation response is the pattern of oceanic warming, which in turn may be related to a change in the mean tropical circulation (Vecchi and Soden 2007; Chou et al. 2009; Huang et al. 2013). In Fig. 30, changes in mean surface (2-m) temperature between the historical and RCP8.5 scenarios in CMIP5 are plotted, noting that changes in surface air temperature over the tropical oceans are strongly tied to changes in sea surface temperatures (SSTs). In the central and eastern equatorial Pacific, eastern equatorial Atlantic, and western Indian Ocean near the horn of Africa, increases in surface air temperature are relatively larger than surrounding areas (Fig. 30a). These are the same tropical regions showing the down-up precipitation response from the cluster analysis (Figs. 21-22). In CMIP5 models, preferential SST warming near the equator is associated with increased upward vertical velocity, causing patterns of annual mean precipitation change to correlate better with the pattern of SST warming than the climatological precipitation (Huang et al. 2013). Such a mechanism, known as “warmer get wetter,” appears to be responsible for much of the regional down-up precipitation response in the tropics emerging from the cluster analysis shown here. A possible exception is the western equatorial Pacific, where direct increases in atmospheric moisture upon the already convergent circulation, described by some as the “wetter get wetter” mechanism,

may be more important for the precipitation increase (Held and Soden 2006; Chou and Neelin 2004; Chou et al. 2009; Seager et al. 2010). Precipitation also increases over east Africa, where the physical mechanisms are less obvious. A shift toward wetter conditions in east Africa was also shown to be a robust CMIP5 response using monthly precipitation in Lintner et al. (2012).

Another proposed mechanism for regional changes, especially decreases, in tropical precipitation is the "upped-ante" mechanism (Neelin et al. 2003; Chou and Neelin 2004). Tropospheric warming increases the moisture threshold necessary for convection to occur (Neelin et al. 2003). Due to regional differences in the increase in atmospheric water vapor with warming, gradients in low-level moisture arise and dry advection occurs over convective margins, preventing those areas from reaching the new moisture threshold (Neelin et al. 2003; Chou and Neelin 2004; Lintner and Neelin 2007). This was shown to be a robust mechanism for regional decreases in precipitation in individual CMIP3 models near convective margins (Chou et al. 2009). In the analysis shown here, there do not appear to be areas of notable precipitation decrease near convective margins in the ensemble and climatological mean (Fig. 19). This may be because regional changes in tropical precipitation, as well as the placement of climatological convergence zones, are highly variable among individual models and the signal cancels out in the model mean (Chou et al. 2009). When looking at Fig. 26 more closely, there are adjacent areas of the down-up and up-down cluster assignments in the western Pacific in some models, suggesting that precipitation decreases near convergence zones. However, a more in-depth analysis of individual models would be necessarily to better understand how the upped-ante mechanism relates to changes in the precipitation

distribution at the regional level in these models. Lintner et al. (2012) propose that the upped-ante mechanism may be responsible for decreases in light-moderate monthly precipitation frequencies when considering the aggregate tropical land precipitation distribution. From this perspective, the upped-ante mechanism may be emerging from the cluster analyses in this chapter as the regional-mean decreases in light-moderate precipitation in the up-down-up cluster (e.g., Figs. 22c,d).

Changes in the atmospheric circulation represent another potentially significant mechanism leading to the spatial pattern of precipitation changes, especially in the extratropics. The transition from little change to projected decreases in mean sea level pressure (PMSL) in high latitudes, especially near 55°S, is geographically consistent with the transition from the up-down-up to down-up precipitation responses (Figs. 21, 22, 30b). Thus a poleward shift in storm tracks (e.g., Yin 2005; O'Gorman 2010; Chang et al. 2012) appears to be important for the high-latitude down-up precipitation response. In the northern high latitudes, it is also tempting to make a connection between the relatively large warming and down-up precipitation response (Figs. 21c, 22c, 30a). This is because warmer temperatures in the presently cold and relatively dry region would likely lead to more frequent and larger precipitation events due to increased atmospheric moisture (Held and Soden 2006; Seager et al. 2010). However, the relationship between surface warming and the increased precipitation response in southern high latitudes is considerably weaker, as is the apparent correlation between warming and precipitation changes over other land regions.

To further explore how changes in atmospheric circulation may be related to changes in the precipitation distribution, percentage changes in the root-mean-square

(RMS) of high-pass filtered relative vorticity of the 850 mb wind (hereafter RMS(ζ850)) is shown as a metric of changes in storm activity (Fig. 30c). The high-pass data were created by subtracting low-pass filtered data with a cutoff period of 10 days, using a Lanczos filter, from the daily time series. RMS(ζ850) is therefore a measure of the activity of storms with a time scale of less than 10 days. Though high-latitude changes in RMS(ζ850) are considerably weaker than changes in mean PMSL, mostly because of large intermodel variability (not shown), a connection between a poleward shift in storms and the high-latitude precipitation response can still be detected, especially in the Southern Hemisphere. Furthermore, the RMS(ζ850) metric more clearly shows decreases in storm activity in parts of the mid-latitudes and subtropics, the same areas that have the up-down-up or up-down precipitation response. The reduction in storm activity over these areas is likely from a combination of a poleward shift in the descending branch of the Hadley circulation and poleward migration of extratropical storm tracks (e.g., Lu et al. 2007; Seager et al. 2010). Decreases in storm activity over these regions may be tied to the decreased frequency of the middle part of the precipitation distribution representing moderate precipitation events (Lau et al. 2013). In the tropics, there are modest increases in RMS(ζ850) over some of the areas characterized by the "warmer get wetter" response (Figs. 22c, 30c), possibly reflecting changes in circulation induced by differential SST warming and subsequent feedbacks between convection and the low-level circulation (Trenberth 2003; Chou et al. 2009; Huang et al. 2013).

Over all locations but the driest subtropical subsidence regions, annual heavy precipitation is projected to increase in a warmer climate (e.g., Figs. 20, 25). In parts of

the subtropics and midlatitudes, increases in the heavy tail of the precipitation distribution occur despite decreases in overall storm activity (Fig. 30c). In some of these places, thermodynamic mechanisms for increases in heavy precipitation, such as enhanced atmospheric moisture, may overcompensate weakening of the atmospheric circulation during the most intense precipitation events (e.g., Allen and Ingram 2002; O'Gorman and Schneider 2009a,b). In other places, such as the midlatitudes, decreases in RMS(ζ850) may result primarily from less frequent or less intense storms that produce light-moderate precipitation and the circulation accompanying heavy precipitation may not weaken, resulting in increased heavy precipitation due primarily to thermodynamic mechanisms (e.g., Sugiyama et al. 2010; Lau et al. 2013). Areas characterized by a robust decrease in the heaviest precipitation events (e.g., Figs. 20, 25) are those in which percentage decreases in RMS(ζ850) are largest (Fig. 30c). This implies that circulation changes, possibly including enhanced subsidence over the already dry subtropical oceanic regions or a shift in the subsidence regions (e.g., Chou et al. 2009; Seager et al. 2010), wins over increased atmospheric moisture in determining the sign of changes in the heaviest events. A more in-depth exploration of the regional mechanisms for changes in the heavy tail of the precipitation distribution in CMIP5 models will be provided in chapter 4 of this dissertation.

Finally, the down-up-down-up precipitation response that occurs in small areas (Figs. 24a,c) is another topic of interest. When performing the cluster analysis for individual seasons, the down-up-down-up cluster emerges in December-February (DJF), March-May (MAM), and September-November (SON) though the signal is less robust (not shown). This shows that while the response is not an artifact of combining

potentially different seasonal precipitation characteristics together, the down-up-down-up response may not be significant or may emerge as a result of insufficient sampling. A more in-depth intermodel and regional analysis is necessary to shed more light on the potentially complex physical mechanisms responsible for precipitation change over these locations.

3.5 Discussion of broader impacts and limitations of the analysis

The analysis presented in this chapter demonstrates the usefulness of applying an objective methodology, k-means cluster analysis, to summarize and better understand projected changes in precipitation in climate model simulations. K-means clustering allows for the detection of regions with similar and coherent changes in the complex daily precipitation distribution, paving the way for further analysis within those regions. Such an approach may be more effective than using arbitrarily defined regions with little physical basis to understand the response of climate variables to global warming, which is common in previous studies. In addition to being an effective method to summarize daily temperature distributions (Loikith et al. 2013), the analyses in this chapter show that cluster analysis yields useful results even when applied to a spatially and temporally noisy variable like precipitation.

However, there are limitations in the application of cluster analysis to daily precipitation that are worth mentioning. The most notable is the large grid cell variability of precipitation histograms within cluster groupings, which exists even when considering places with small histogram distances from the assigned cluster histogram (e.g., Fig. 23). Thus, to some extent, the results of the cluster analysis applied to the precipitation

distribution may only faithfully represent the precipitation response averaged over broad regions. This is especially true when considering a model ensemble in which individual models have large variability in the regional patterns of precipitation change. A more in-depth analysis of individual models than presented here is required to better understand these intermodel differences. However, application of the analysis using 8 clusters to the individual CMIP5 models revealed histogram shapes that generally fell into one of the 4 types of Table 3 (not shown), demonstrating the robustness of those precipitation responses among the models.

Finally, the cluster analysis presented in this chapter focuses on annual precipitation, both for brevity and to increase the sample size from which precipitation histograms are generated. A brief look at individual seasons did not reveal the emergence of histogram shapes distinct from those shown throughout this chapter, but did reveal unique spatial patterns of the cluster assignments in different seasons (not shown). A further exploration of individual seasons may therefore provide a more complete physical understanding of regional precipitation changes in CMIP5 models (e.g., O'Gorman 2010; Huang et al. 2013).

4. Physical mechanisms for projected changes in heavy precipitation

4.1 Introduction

In this chapter, projected future changes in heavy to extreme daily precipitation are further explored in CMIP5 simulations. The thermodynamical and dynamical physical mechanisms responsible for changes in local heavy precipitation across the globe are qualitatively and quantitatively examined (see section 1.4 for a comprehensive discussion of potential mechanisms). In addition to investigating how local changes in vertical velocity influence changes in heavy precipitation, changes in the large-scale horizontal atmospheric circulation accompanying heavy precipitation are investigated with composite analysis. In section 4.2, the CMIP5 output and methodology are described. Projected changes in heavy precipitation and the thermodynamical and dynamical mechanisms for such changes are presented in section 4.3. In section 4.4, changes in the horizontal circulation features associated with heavy precipitation are explored with a comprehensive composite analysis, and potential mechanisms for changes in tropical circulation are discussed. A brief summary and discussion of limitations is given in section 4.5.

4.2 Data and Methodology

4.2.a CMIP5 output and general analysis methods

The same CMIP5 models that were used to study changes in the daily precipitation distribution in chapter 3 (Table 2) are used for the analysis of heavy

precipitation in this chapter. Additionally, the same CMIP5 experiments (RCP8.5 and historical), 21-year time periods (1979-99 and 2079-99), and 2.5°x2.5° common grid that are described in sections 2.5 and 3.2.a are used in this chapter.

Throughout this dissertation, the local 99th percentile of daily precipitation (computed from all days, including zeros) has been used as a threshold for heavy precipitation. The same methodology is applied in this chapter. The days when precipitation equals or exceeds this value are used to compute the mean intensity of heavy precipitation (P99M), the modified O'Gorman and Schneider 2009b (hereafter OS09b) thermodynamic scaling (described in section 4.2.b), and composites of atmospheric quantities during heavy events at each grid cell (described in section 4.2.c). The heavy precipitation metrics are computed using days from all seasons (~76 days per grid cell per 21-year simulation), from boreal winter (December-February, DJF, ~19 days), and from boreal summer (June-August, JJA, ~19 days). The analysis focuses these seasons for brevity and to highlight the winter and summer seasons of each hemisphere, when changes in atmospheric circulation vary most from the annual mean. In some models, the 99th percentile of daily precipitation is zero at some of the driest locations and seasons (e.g., northern Africa during DJF). If the 99th percentile is zero in at least one model in either the historical or RCP8.5 time period at a grid cell, that grid cell is excluded from all analyses. Additionally, the 99th percentile and above may contain days with very light precipitation at very dry locations. Thus the heavy precipitation metrics and composites presented in this chapter may only represent a "rainy day" at these places rather than heavy or extreme hydrological precipitation. However, in the context of all days in the record at a very dry location, having any precipitation may be considered a

rare occurrence and is likely associated with anomalous circulation patterns and thermodynamic conditions. Throughout the rest of this chapter, precipitation equaling or exceeding the 99th percentile is referred to as "heavy precipitation."

The analyses in this chapter focus on the multimodel mean to highlight common regional features of heavy precipitation change across the models, since spatial patterns of precipitation change can be very variable for individual models (e.g., Chou et al. 2009). Using the multimodel mean has the advantage of condensing the analysis to one "simulation," making the presentation manageable, and increasing the sample size of heavy precipitation days used to compute the metrics. While an exploration of differences between models may provide further insight into the mechanisms for changes in heavy precipitation, a detailed effort to understand why individual models have different responses is not attempted in this chapter.

4.2.b Thermodynamic scaling for heavy precipitation

In this chapter, a thermodynamic variation of the scaling for extreme precipitation presented by OS09b is computed for each grid cell on the global domain. The thermodynamic version, described in OS09b, simply eliminates vertical velocity from the computation (see Eq. 1). Retaining vertical velocity in the scaling but not allowing it to change between present and future climates in CMIP3 did not yield different results from eliminating it entirely in OS09b. Although including vertical velocity is important to explain the full sensitivity of extreme precipitation, the simplified scaling is used here only to quantify the thermodynamic component of the expected heavy precipitation response. Local differences in the actual heavy precipitation response from this scaling

will highlight areas where changes in the atmospheric circulation should be substantial, which are analyzed separately and in more detail with composite analysis (described in section 4.2.c). The mathematical expression for the thermodynamic OS09b scaling is

$$P_h \sim \int_{250}^{p_s} \frac{dp}{g} \frac{dq_s}{dp}\Big|_{\theta^*, T_h}, \qquad (1)$$

where P_h is the thermodynamic prediction of heavy precipitation intensity for a particular time period (historical or RCP8.5) and grid cell, noting that the units do not match that of precipitation since pressure velocity was removed from the expression. The pressure integral is from the surface, p_s, to 250 mb. Inside the integral, p is pressure, q_s is saturation specific humidity, and g is the gravity constant assumed 9.8 m s^{-1} in all calculations. The derivative $\frac{dq_s}{dp}$ is computed at each level assuming constant saturation equivalent potential temperature, θ^*, which in turn is determined from the temperature averaged over heavy precipitation days at that grid cell and level, T_h. The standard atmospheric levels available from CMIP5 that were used in the computation of Eq. (1) were 1000, 850, 700, 500, and 250 mb. Since surface pressure was generally unavailable from the CMIP5 archive, it was computed with the hydrostatic equation.

There are a few differences between the calculation of Eq. (1) in this chapter and that done by OS09b. For one, the 99th percentile is used as a threshold for heavy precipitation here, whereas OS09b use a more extreme threshold. The lower percentile is chosen here to increase the sample size of heavy precipitation events, as the scaling is computed at every grid cell. In OS09b, the scaling is computed for latitudinal bands where grid cells are first aggregated over longitude, increasing the sample from which extreme events are chosen. Due to the aggregation, the extreme percentiles in OS09b are

more representative of the wettest locations over a particular latitude band than the zonal mean. Thus, the method applied here has the advantage of showing detailed spatial variability in the scaling, but also has the limitations of using a relatively low precipitation threshold, as were described in section 4.2.a. Another difference between the methodology employed here and that of OS09b is that the pressure integral is computed up to a fixed level of 250 mb rather than computing a tropopause level as the upper limit. It is unclear what impact this simplification has on the results, but based on the limited number of atmospheric levels available from the CMIP5 archive and general agreements between the results shown here and that of OS09b, the simplification appears to be justified.

The final thermodynamic scaling can then be expressed as

$$S_h = 100 \times \left(\frac{P_{h,RCP8.5} - P_{h,hist}}{P_{h,hist}} \right) \Big/ \Delta T_g, \qquad (2)$$

where S_h is the scaling in units of % K^{-1}, $P_{h,hist}$ and $P_{h,RCP8.5}$ are the thermodynamic predictions computed from Eq. (1) for the historical and RCP8.5 time periods, respectively, and ΔT_g is the RCP8.5 minus historical difference in globally-averaged area-weighted climatological-mean 2-m air temperature. Normalizing the scaling by ΔT_g is consistent with the methodology of OS09b and Sugiyama et al. (2010) and is mainly intended to adjust for intermodel variability in climate sensitivity. Accounting for local variations in the change in temperature during extreme events (Fig. 31) is unnecessary in the normalization, as they are already accounted for in the computation of P_h. The scaling S_h is compared with the actual response of heavy precipitation R_h, defined as

$$R_h = 100 \times \left(\frac{P99M_{RCP8.5} - P99M_{hist}}{P99M_{hist}}\right) \Big/ \Delta T_g, \qquad (3)$$

where $P99M_{hist}$ and $P99M_{RCP8.5}$ are the historical and RCP8.5 values of P99M, respectively.

4.2.c Composite analysis

The composite analysis that was used in the evaluation of CMIP3 and CMIP5 over the late 20th century, described in sections 2.4 and 2.5, is very similar to that used in this chapter. Atmospheric quantities are averaged over days when daily precipitation equals or exceeds the 99th percentile at a particular location (as described in section 4.2.a). Many of the quantities that were analyzed in sections 2.4 and 2.5 are also analyzed here, including pressure at mean sea level (PMSL), geopotential height at 500 mb (Z500), and low-level (10-m to 500-mb average) wind. Additionally, relative vorticity of the wind at 850 mb (hereafter ζ850) is analyzed. Z500 is computed with the hypsometric equation using the standard CMIP5 pressure levels (1000, 850, 700, 500 mb), following the methodology of sections 2.4 and 2.5. LWND is also computed from these same levels. Composites of **Q**-vector convergence (QVC, described in section 2.4), are also shown in this chapter. QVC is used to assess whether changes in vertical velocity accompanying heavy precipitation are also associated with changes in the synoptic and meso-α-scale forcing for ascent (including warm air advection, positive vorticity advection, and large-scale frontogenesis). Since QVC is important in the lower troposphere, it is averaged over 850, 700, and 500 mb before being composited over heavy precipitation days. As a simple metric to quantify actual vertical motion, the

pressure velocity at 500 mb (ω500) is computed. The computation is performed assuming continuity, in which the wind divergence is vertically integrated from the surface to 500 mb using the standard CMIP5 atmospheric levels. For the calculation of all quantities involving multiple vertical levels, levels below the surface, determined from the surface pressure, are omitted from the calculation.

The z-scores for some of the quantities described above are also analyzed, which are computed in the same way as described in section 2.4. For most quantities, the z-scores for the RCP8.5 simulation are computed using the mean and standard deviation of the historical period, so that changes in z-scores from the historical to future periods include changes in both the mean and variability of the quantities. However, mean Z500 is expected to increase in a warmer climate as a result of warmer troposphere temperatures (not shown). When considering the large-scale patterns of Z500 during heavy precipitation events, it is desirable for changes in the z-score to better reflect changes in the circulation rather than the mean thermodynamic conditions. Therefore, the RCP8.5 z-score of Z500 is computed using the RCP8.5 (2080-98) mean and historical (1980-98) standard deviation, removing increases in Z500 caused by mean tropospheric warming. In the remainder of this chapter, the z-score of a particular quantity is identified with an asterisk (e.g., Z500* = z-score of Z500), and the terms “anomaly” and “z-score” are used interchangeably.

4.3 Projected changes in heavy precipitation

The historical patterns of P99M along with their change between the historical and RCP8.5 simulations are shown in Fig. 20 and were briefly discussed in section 3.3.a.

To review and summarize, heavy precipitation increases almost everywhere on the globe, with the exception of dry subtropical oceanic regions annually and some low-latitude land regions during certain seasons. Land regions with projected decreases in P99M include northern Africa in DJF and eastern South America, southern Africa, southern Europe, and northern Australia in JJA (Fig. 20h,i). In the broad sense, patterns of change in P99M follow the historical climatology of P99M, including decreased P99M in dry regions and the largest absolute increases in the tropics. These patterns are consistent with a general intensification of the hydrological cycle due to increased atmospheric moisture assuming small changes in the large-scale circulation (e.g., Held and Soden 2006; Seager et al. 2010). However, there are several regions where the relationship is not so simple. For instance, there are increases in P99M in the relatively dry high latitudes and equatorial east Pacific, and decreases in some wet regions and seasons, including the Bay of Bengal in DJF and the Indian Ocean adjacent to Australia in JJA. A better understanding of the mechanisms for such regional changes in P99M is attempted in this chapter.

Fig. 32 shows the metrics of heavy precipitation sensitivity (R_h, S_h, and their difference) that were introduced in section 4.2.b. In all cases, the CMIP5 multimodel average is shown. In computing the model average values for S_h and R_h, the individual components of Eqs. (2) and (3) (i.e., P_h, P99M, and ΔT_g) were first averaged over the models. An alternative approach is to calculate S_h and R_h for each model first and then compute the multimodel mean or median (as in OS09b); however, this method yields qualitatively similar but noisier spatial patterns (not shown). Predicted relative changes in heavy precipitation by the thermodynamic scaling S_h are much smoother than the

actual precipitation response R_h and are positive everywhere due to increasing T_h (and therefore moisture) everywhere on the globe (Figs. 31, 32a-f). In Fig. 32, R_h and S_h are plotted using a color scale that is centered at 7% K^{-1} to see how either quantity compares with the approximate scaling of low-level atmospheric moisture predicted by the Clausius-Clapeyron (hereafter C-C) relationship for global mean conditions. Compared with C-C scaling, S_h is smaller across much of the globe (Figs. 32d-f) because increases in $\frac{dq_s}{dp}\Big|_{\theta^*,T_h}$ with warming are smaller than increases in q_s itself due to a decrease in the moist adiabatic lapse rate (O'Gorman and Schneider 2009a). This makes S_h a better predictor of R_h at midlatitudes than C-C scaling, where the actual precipitation response is slightly less than 7% K^{-1} (Figs. 32a-f). At high latitudes, the inclusion of local temperatures during heavy events in the computation of S_h causes the predictions to be higher than C-C scaling (Figs. 32d-f), as warming at high latitudes is larger than the global mean (Fig. 31). This also makes S_h a better predictor of R_h than C-C scaling at high latitudes.

Despite the marginal improvements that the local thermodynamic OS09b scaling has over global-mean C-C scaling, the difference between R_h and S_h is large over many areas, especially in the low latitudes (Figs. 32g-i). As seen with the difference in ω500 averaged over heavy precipitation days ($\Delta\omega 500_h$, Figs. 32j-l), the differences between R_h and S_h are mainly a result of changes in vertical velocity, as was concluded in OS09b and Sugiyama et al. (2010). That is, upward velocity increases ($\Delta\omega 500_h < 0$) in areas where heavy precipitation increases faster than the thermodynamic prediction ($R_h > S_h$), and vice versa. $\Delta\omega 500_h$ not only explains low-latitude patterns of $R_h - S_h$ but is also negative (implying increased ascent) where S_h underpredicts R_h in northern high

latitudes. Accounting for changes in vertical velocity is thus important for explaining the heavy precipitation response to warming not only in the zonal mean sense (as shown in OS09b), but also locally. Based on a comparison of $R_h - S_h$ and $\Delta\omega 500_h$ in Fig. 32, it appears as though the full OS09b scaling (which is not explicitly computed here) would predict local patterns of R_h reasonably well in CMIP5 models.

Though the thermodynamic scaling S_h is not enough to explain the local heavy precipitation response at many locations, it performs better at the global spatial scale where local changes in circulation partially cancel. To quantify this, the global median grid cell value of S_h and R_h is computed for each model and the intermodel variability of the global median is shown with box-and-whisker diagrams in Fig. 33. The global median is used rather than the mean because it is less sensitive to outlier values of precipitation sensitivity at certain locations (not shown). From the ensemble perspective, the range of global median heavy precipitation sensitivities predicted by S_h is in good agreement with the range of actual sensitivities R_h, especially for the middle 50% of simulations, though the full range of model variability is larger for R_h (Fig. 33). Note that because statistics shown on the box-and-whiskers (e.g., the maxima) do not necessarily correspond to the same model, there may be larger differences for individual models that are masked.

Fig. 33 also shows the global sensitivity for specific percentiles of daily precipitation, computed for each day in the record above the 50th percentile (i.e., the maximum precipitation value, second maximum, etc.). To compute this, the sensitivity at each grid cell is computed in the same way as R_h is computed (Eq. 3), but for specific percentile values rather than the mean over the 99th-100th percentile. The global median

grid cell sensitivity value for each percentile and model is then computed and the intermodel variability of the sensitivities is shown on the graphs in Fig. 33. The global sensitivity of precipitation increases as the percentile becomes more extreme in all cases (annual, DJF, and JJA) (Fig. 33). Indeed, the annual global precipitation sensitivity is better centered at 7% K^{-1} in the model ensemble than in the range of S_h for the most extreme daily events (Fig. 33a). This suggests that increases in lower tropospheric water vapor, governed by the C-C relation, are a sufficient predictor of the global response of the most extreme daily precipitation, at least for the ensemble median. The rather large intermodel spread in the sensitivity of very extreme precipitation of 4-10% K^{-1} (Fig. 33a), is consistent with that found in Kharin et al. (2013) using different methods.

4.4 Composite analysis

4.4.a Composite patterns for selected locations

In this section, the changes in atmospheric circulation accompanying heavy precipitation events are explored in more detail. To begin, composite spatial patterns of relevant atmospheric quantities during heavy events are shown at selected locations (see sections 2.4 and 4.2.c for methodology). This section focuses on locations near and surrounding North America, where the evaluation of CMIP3 and CMIP5 in sections 2.4 and 2.5 shows that the atmospheric circulation features accompanying heavy precipitation events are realistic when compared to reanalysis. The composites in this section also focus on winter (DJF) because the circulation features tend to have better spatial definition during this season (see section 2.4). The motive behind showing

composites for individual grid cells is to 1) provide a taste of how the circulation features change at locations where the thermodynamic scaling S_h is a sufficient or poor predictor of the actual sensitivity of heavy precipitation, and 2) show examples of quantities that are relevant for describing the circulation at different latitudes, which will be used later in this chapter to summarize the circulation features at all grid cells globally.

A region where increases in heavy winter precipitation are reasonably constrained by thermodynamics and in which changes in vertical velocity during heavy events are small is the northeastern United States (Figs. 32h,k). In Fig. 34, composites are shown for a grid cell near New York City (NYC). Heavy winter precipitation events ($\geq 99^{th}$ percentile) at this location are, on average, associated with an area of low PMSL immediately southwest of the location, allowing the surface flow to direct moisture from the nearby Atlantic Ocean. The atmospheric circulation is also characterized by a large-scale anomaly pattern of Z500, with a minimum to the southwest and maximum to the northeast (Fig. 34a), and positive ζ850 closely centered over the surface low (Fig. 34d). QVC is also positive over the NYC grid cell (Fig. 34g), showing that large-scale dynamics are important for forcing ascent at this location. The center of maximum of QVC is over and northeast of the surface low, possibly reflecting low-level warm air advection from southeast winds acting on the strong winter land-sea temperature contrast. When comparing the composite patterns between the historical and RCP8.5 time periods, they are remarkably similar for all quantities plotted. Indeed, the RCP8.5-historical differences in Z500*, ζ850, and QVC (Figs. 34c,f,i) are close to zero despite the relatively large magnitudes of these quantities in either the historical or RCP8.5 composites. The differences in PMSL show a somewhat larger change, with the surface

high over the Atlantic being marginally stronger and surface low to the west also slightly stronger in the future period. This implies that the PMSL gradient is slightly greater in the future simulation, though this is hardly detectable when looking at the composites for the individual time periods.

The intermodel robustness and statistical significance of the RCP8.5-historical composite differences are evaluated by comparing the sign of change in each model with the model mean and performing a two-tailed t-test with α=0.5 for the change, at every grid cell on the composite map. If at least 12 of the 17 models agree with the model mean sign of change and at least 6 of those models also show a statistically significant change at a grid cell, the grid cell is highlighted with a dot for PMSL or cross for the color-filled quantities in Figs. 34-36. As can be seen in Fig. 34, these criteria are only met at stray grid cells away from the location experiencing heavy precipitation in the NYC case, unrelated to the local circulation. Decreases in PMSL to the west of the grid cell and increases to the east do not meet the robustness and significance criteria (Fig. 34c). The decrease in PMSL over northern Canada is partly influenced by decreases in climatological mean PMSL over the high latitudes in DJF (not shown). In summary, the strength and spatial patterns of the atmospheric circulation during extreme winter precipitation events near NYC are very similar between the historical and future CMIP5 simulations. This is not surprising since changes in heavy precipitation follow thermodynamic constraints and changes in vertical velocity are small (Figs. 32h,k).

In Fig. 35, the composite patterns for a grid cell where winter heavy precipitation and upward vertical velocity decrease in the future simulation is shown, located along the west coast of Mexico (Figs. 32b,k). Unlike the NYC case, the magnitude of ζ850 is

considerably smaller during heavy events (not shown), thus its z-score ζ850* is a better metric to characterize the anomalous circulation (Fig. 35d, note that ζ850* is not computed where the 850 mb level is below ground). Further, QVC is a poor metric to characterize the circulation at this location because it is maximized north of the grid cell due to topographical influences, and thus does not represent local synoptic forcing (not shown). The composite PMSL pattern associated with heavy precipitation at this location is not characterized by a closed low, but rather a trough of low PMSL extending from the south (Fig. 35a). PMSL*, on the other hand, has a closed minimum over the trough of low PMSL (Fig. 35g), making it a suitable metric to summarize closed features of the circulation pattern at this location. In the future simulation, all circulation features are weaker, most notably for the trough of PMSL and magnitude of negative PMSL*, in which the differences for both meet the robustness and significance criteria over a broad region centered over the grid cell (Figs. 35c,i). Changes in ζ850* appear to be small and less widespread partly because of missing values over and near the grid cell (Fig. 35f). Though the overall strength of the circulation is weaker in the future simulation, the circulation patterns (i.e., the PMSL pattern and positions of the minima or maxima of Z500*, ζ850*, and PMSL*) remain unchanged, as seen by the high spatial correlations between the historical and RCP8.5 composites (Figs. 35c,f,i). The overall weakening of the circulation is not surprising given the decrease in heavy precipitation and upward velocity over this location (Figs. 32b,k).

In the previous two cases, the climatological winter heavy precipitation (P99M) in the historical periods is relatively large (Fig. 20b). In Fig. 36, changes in the atmospheric circulation over a dry region with projected decreases in winter P99M, the low-latitude

North Atlantic (Fig. 20b,h), are shown. The same quantities are plotted as for the Mexico case. ζ850 and QVC are poor metrics to characterize the circulation at this location also, due to very low magnitudes and weak spatial definition (not shown). The pattern of PMSL during extreme winter events at this location has even less definition than for the Mexico case (Figs. 35a, 36a), perhaps because of the smaller climatological P99M. Nonetheless, there is a closed area of negative PMSL* over and west of the grid cell in the historical period (Fig. 36g) as well as notable areas of negative and positive Z500* and ζ850*, respectively (Figs. 36a,d). All anomalies have smaller magnitudes in the RCP8.5 simulation, as seen in the individual period composites and difference plots, with the robustness and significance criteria being met for ζ850* and PMSL* near the grid cell (Figs. 36f,i). There is even a small increase in PMSL near the grid cell, which is not detectable from the PMSL pattern in the composites for the individual periods (Figs. 36a-c). However, this increase only meets the robustness and significance criteria in few locations (Fig. 36c). Like in the Mexico case, the magnitudes of the anomalies associated with the circulation weaken even though the overall positions of these anomalies appear to remain constant in the future. This implies that the average physical mechanisms that are associated with heavy precipitation, such as anomalously high ζ850 northwest of the grid cell, are the same in the future but are weaker. The weakening circulation features associated with heavy precipitation at this location coincide with a rather large decrease in upward vertical velocity between the historical and future simulations during heavy winter precipitation events (Fig. 32k).

4.4.b Summary of composite patterns for all locations

In the previous section, decreases in the upward velocity associated with heavy precipitation appear to be associated with decreases in the strength of lower atmospheric circulation anomalies, while changes in the circulation pattern are small. Does this relationship hold at other locations, and does the horizontal circulation strengthen in areas with projected increases in upward velocity? To address these questions, the composite analysis is expanded to all grid cells. Rather than showing plots like Figs. 34-36 for many more locations, the circulation features associated with heavy precipitation are summarized using various metrics (described next), which are displayed on a global map.

Since PMSL* effectively characterizes the pattern and strength of surface circulation anomalies associated with heavy precipitation at most places, it is useful to summarize its pattern and strength with a simple metric. After computing the multimodel mean PMSL* composite for a grid cell (analogous to Figs. 35g,h), the PMSL* pattern for each time period (historical and RCP8.5) is summarized by determining the position and magnitude of the nearest closed minimum of PMSL* to the grid cell (for example, the area just northwest of the grid cell in Fig. 35g). The PMSL* minimum is found using a simple algorithm that searches in an expanding box centered on the grid cell experiencing heavy precipitation. The searching is stopped and no minimum is found if 1) the distance from the center grid cell to the east (or west) edge of the search box exceeds 1000 km (hereafter search radius), 2) the north or south edge of the box exceeds the polar boundaries, or 3) any missing values are encountered in the box. Since minima in PMSL* are usually detected close to the grid cell experiencing heavy precipitation (Figs. 35-36), minima more than 1000 km away may not be relevant for the local precipitation, and such minima are excluded from the analysis. As seen later, this only happens in the

deep tropics. The above procedure is performed for every grid cell on the domain. Once the nearest minimum PMSL* is found for a grid cell, the magnitude of the minimum is displayed with color fill (Fig. 37 left column) and the position of the minimum relative to the grid cell with an arrow (indicating direction) and color fill (indicating distance) (Fig. 37 right column), both plotted at the grid cell experiencing heavy precipitation. In other words, the values at each grid cell in Fig. 37a do not represent local values of PMSL*, but rather the magnitude of the nearest closed minimum of PMSL* associated with heavy precipitation events at the grid cell. The vectors in the right panels of Fig. 37 point in the direction of the nearest minimum and the distance of the minimum from the grid cell experiencing heavy precipitation is color filled. The analysis focuses on annual heavy precipitation for brevity, though the results are qualitatively similar when focusing on just DJF or JJA, but with some regional differences (not shown). More days are also available from the annual sample of heavy events, allowing for the emergence of smoother patterns (not shown).

The magnitudes of PMSL* minima associated with heavy precipitation in the subtropical regions are largest out of anywhere on the domain, while they are considerably smaller for heavy precipitation events near the storm tracks of both hemispheres (Fig. 37a). This is the result of both larger climatological mean and lower variability of PMSL in the subtropical latitudes (not shown). Near the storm tracks (North Atlantic and Pacific and Southern Ocean), PMSL minima associated with heavy precipitation are not much lower than the climatological PMSL relative to the local variability, especially in the Northern Hemisphere (NH). This means that heavy precipitation is generally not also associated with extreme anomalies of PMSL, as the

PMSL minima are only within 1-1.5 standard deviations of the mean PMSL. This is consistent with the recent work of Pfahl and Wernli (2012), who found that cyclones producing extreme precipitation are often not stronger than the average cyclone over NH storm tracks in observations. In terms of position, the nearest PMSL* minimum is often equatorward and west of locations experiencing heavy precipitation across much of the subtropics to high latitudes (Fig. 37b). During heavy precipitation events in the midlatitude oceans, PMSL* minima are rather distant, sometimes more than 800 km away, when heavy precipitation occurs. In the tropics, PMSL* minima are either detected right at the grid cell or within one grid cell in either direction (usually west), though the strength of the minima are weak (Figs. 37a,b).

The position and strength of PMSL* minima associated with local heavy precipitation in the RCP8.5 period and their difference from the historical period are also shown in Fig. 37. PMSL* minima associated with heavy precipitation in the low latitudes generally weaken in the future climate (Fig. 37e). The weakening is consistent with decreases in upward vertical velocity during heavy events over some places, such as Australia and the nearby Indian Ocean and subtropical dry regions in the Pacific and Atlantic (Fig. 32j). Thus, the responses shown for individual locations in Figs. 35-36 apply to other locations with similar climatology as well, such as the subtropical South Pacific. However, PMSL* minima also weaken over Indonesia and the northern Indian Ocean, where upward velocity strengthens (Figs. 32j, 37e). Additionally, PMSL* minima marginally strengthen over the South Atlantic in places where upward vertical velocity weakens (Figs. 32j, 37e). The very low magnitudes and sporadic positions of detected PMSL* minima during heavy precipitation at these locations (Fig. 37a,b) makes

one question whether PMSL* is an adequate quantity to summarize the atmospheric circulation. In the high latitudes, the general strengthening in PMSL* minima (Fig. 37e) may be associated with a poleward shift and/or strengthening of the storm tracks (e.g., O'Gorman 2010; Chang et al. 2012). In both northern and southern high latitudes, there are small increases in upward vertical velocity during heavy precipitation events in the future over some of the same places with this strengthening (Fig. 32j). However, the relationship between $\Delta\omega 500_h$ and changes in PMSL* minima magnitude appears stronger in the NH than Southern Hemisphere (SH) (Figs. 32j, 37e). Changes in pressure velocity at 700 mb ($\Delta\omega 700_h$), which are perhaps more relevant for the middle to high latitudes, were also assessed and generally have the same qualitative characteristics as changes in $\omega 500_h$ (not shown). However, changes in $\omega 700_h$ are generally smaller in magnitude than those in $\omega 500_h$ and in some places are more positive ($\Delta\omega 700_h > 0$), such as the North Atlantic where $R_h - S_h < 0$ (not shown).

Changes in the position of the detected PMSL* minima associated with heavy precipitation are small across much of the domain, as seen from the similar position vectors for the individual time periods (Figs. 37d,b) and the small difference in distance (Fig. 37f). Note that differences in distance as large as 300 km often only indicate a shift of one grid cell in the position of the detected PMSL* minimum, which may be partly attributed to noise rather than a robust change in the center of minimum. Also, changes in distance (Fig. 37f) do not form coherent regions, further suggesting that they are not physically meaningful. To summarize, anomalies of PMSL associated with heavy precipitation events change in strength in many places, but the spatial patterns of the anomalies do not substantially change, consistent with the analysis of individual locations

(Figs. 34-36). However, changes in PMSL* minima strength and changes in $\omega 500_h$ are not always consistent (e.g., in the Indian Ocean, Indonesia, South Atlantic, and SH high latitudes), suggesting that other circulation characteristics may be relevant for changes in vertical velocity during heavy precipitation events.

The same analysis as above was performed for the nearest *maximum* in ζ850*, again using a search radius of 1000 km. Prior to detecting the nearest maximum, ζ850* values in the SH were multiplied by -1, such that positive ζ850* represents anomalous cyclonic vorticity everywhere on the globe. The analysis is shown in Fig. 38. Unlike with PMSL*, nearest maxima in ζ850* associated with heavy precipitation are detected across much of the tropics, allowing for a more in-depth analysis there, though they are small in magnitude near the equator (Fig. 38a). The ζ850* maxima are relatively strong across much of the domain outside of the deep tropics. Like with PMSL*, largest anomalies of ζ850, relative to local variability, occur in association with heavy precipitation in the subtropical oceanic regions, while they are somewhat smaller for locations near the storm tracks of either hemisphere. Maxima in ζ850* occur much closer to the grid cell experiencing heavy precipitation than in the case of PMSL*, with the maxima detected right over the grid cell in coherent parts of the tropics and high latitudes (Fig. 38b). In places where the maxima are located away from the grid cell, the position is almost ubiquitously to the west, though in some cases also with an equatorward displacement, especially in southern mid-high latitudes.

Projected changes in the magnitude of ζ850* maxima associated with heavy precipitation are in many places consistent with changes in PMSL* minima. For instance, ζ850* maxima weaken in strength in parts of the subtropics where $\Delta\omega 500_h > 0$

(decreased upward velocity) and heavy precipitation decreases (Figs. 32a,j, 38e). There are also increases in ζ850* maxima strength in the northern high latitudes where PMSL* minima strengthen, though changes in ζ850* maxima are somewhat smaller (Figs. 37e, 38e). Changes in ζ850* maxima strength in the southern high-latitudes near Antarctica cannot be adequately assessed because ζ850* maxima are not detected due to the nearby topography. One notable difference between changes in ζ850* maxima and PMSL* minima strength is in the western equatorial Pacific and Indonesia, where there is a strengthening of ζ850* maxima associated with heavy precipitation and $\Delta\omega 500_h < 0$ (enhanced upward velocity) (Figs. 32j, 38e). Recall that changes in PMSL* minima in these areas were inconsistent with $\Delta\omega 500_h$, suggesting that ζ850* more effectively characterizes the circulation in this region. Changes in ζ850* maxima strength are also more consistent with those in $\omega 500_h$ in the South Atlantic than was the case with PMSL* minima (Figs. 32j, 38e). There is a potent strengthening of ζ850* maxima associated with heavy precipitation in the central and eastern Equatorial Pacific, where PMSL* minima were not detected, consistent with increases in upward velocity there (Figs. 32j, 38e). As was the case with PMSL*, however, changes in ζ850* maxima during heavy events over and near the northern Indian Ocean are less consistent with changes in $\omega 500_h$. The mechanisms for changes in $\omega 500_h$ in these regions may therefore be more complicated than can be summarized with the characteristics of low-level circulation anomalies such as PMSL* or ζ850*. Changes in the position of ζ850* maxima relative to places experiencing heavy precipitation are small and sporadic (Fig. 38f), particularly in areas where changes in ζ850* maxima magnitude are largest. This

once again supports the conclusion that changes in the strength of circulation features associated with heavy precipitation are more substantial than changes in the pattern.

To further explore projected changes in vertical velocity and how it relates to the large-scale circulation in the extratropics, composites of QVC for each grid cell are summarized. One goal of this analysis is to see whether increases in the strength of high-latitude circulation features during heavy precipitation events, such as PMSL* minima or ζ850* maxima (Figs. 37e, 38e), are also associated with greater large-scale synoptic forcing for accent, and thus larger QVC. Since QVC is associated with upward vertical motion locally (Fig. 34g), the composites of QVC for each grid cell are summarized by linearly averaging QVC over a 3x3 grid cell box centered on the grid cell experiencing heavy precipitation. The resulting average is then plotted at the grid cell experiencing heavy precipitation on a global map. The 3x3 box averaging is used to reduce noise and also account for nearby circulation features that may be relevant to the overall precipitating system. QVC is not evaluated unless the 850 mb level is above the surface. This allows one to focus on lower elevation areas, where positive QVC is a reflection of the horizontal circulation features rather than influences from topography. The tropics (30°S-30°N) are omitted from this analysis because QVC is generally less relevant for heavy precipitation there, due to weaker and less baroclinic circulation features.

The QVC results are plotted in Fig. 39 for the NH using a polar stereographic projection. Unlike in the nearest minima/maxima plots of Figs. 37-38, color fills are representative of local values of QVC during heavy events at each grid cell. QVC associated with heavy precipitation is largest near the storm tracks (North Pacific and North Atlantic) and smaller in the lower latitudes (Figs. 39a-c). This is not surprising,

since storm track regions are typically associated with stronger horizontal gradients in geopotential height and temperature, which tend to make QVC larger. Changes in QVC from the historical to future periods are most substantial and geographically coherent in the North Pacific, where QVC *decreases* in the future, especially during DJF (Fig. 39d-f). These decreases are somewhat surprising, since they occur over an area where upward vertical velocity marginally increases (i.e., $\Delta\omega 500_h < 0$) in the future (Fig. 39g-i). Thus, changes in the forcing for ascent associated with synoptic-scale circulation patterns, such as temperature and vorticity advection and large-scale frontogenesis, may not to be important for enhanced upward motion during heavy precipitation events in this area. Indeed, decreases in QVC suggest that changes in the synoptic forcing may counteract increases in upward motion, perhaps due to weaker horizontal temperature gradients in the lower troposphere in the RCP8.5 simulation (Chang et al. 2012). Furthermore, QVC also decreases over some of the same locations with projected strengthening in PMSL* minima and ζ850* maxima, such as between Alaska and Russia near 180°W (Figs. 37e, 38e, 39d). This implies that intensification of the low-level circulation anomalies (i.e., PMSL* and ζ850*) do not strengthen the large-scale synoptic forcing quantified with QVC. That is, enhanced upward motion may simply be arising from increased low-level convergence associated with the stronger circulation, rather than stronger gradients of the temperature, geopotential height, or vorticity fields which can also force rising motion. In the SH, changes in QVC averaged over heavy events are somewhat more consistent with changes in $\omega 500_h$, especially when considering events from all seasons, but both are small in magnitude and the pattern of change is noisier (not shown).

Another aspect of the atmospheric circulation worth investigating is the low-level wind flow during heavy precipitation events, which is related to moisture transport and local horizontal gradients in pressure in the lower atmosphere. At each grid cell, the local average low-level wind (defined in section 4.2.c) during days with heavy precipitation (including all seasons) is computed. The results are displayed in Fig. 40, where vectors indicate wind direction and color fills show wind speed in the top panels (note that Fig. 40a is the same as Fig. 17c, but for the entire global domain). The winds associated with heavy precipitation have a substantial poleward component across much of the domain outside of the tropics, consistent with the transport of warmer and moister air from lower latitudes to support heavy precipitation (Fig. 40a). Indeed, winds in the highest latitudes are almost entirely directed from lower latitudes, while they have a more westerly component in the midlatitudes. The winds are strongest in the midlatitudes of either hemisphere, particularly over oceans, suggesting that large horizontal pressure gradients often arise in these regions in association with heavy precipitation. The relatively smooth ocean surface allows for stronger winds over the ocean than over land areas at the same latitudes. The above features are in contrast to climatological mean winds, which are almost entirely westerly and weaker in the midlatitudes (not shown). Winds associated with heavy precipitation in the tropics typically have an easterly component and are small in magnitude, with the exception of the Indian Ocean where the local circulation patterns favor westerly winds over many places.

Projected changes in the wind speeds associated with heavy precipitation are shown in Fig. 40c. The most substantial changes are in the mid-high latitudes of the SH, where wind speeds increase as much as 2 m s^{-1} in the future between 40°S and 60°S (Fig.

40c). These increases appear to be the result of a poleward expansion of the band of strongest winds in the historical period (Figs. 40a,b), perhaps associated with a poleward shift and/or strengthening of the storm track. It is interesting that changes in vertical velocity over this region are small (Fig. 32j), despite strengthening of the low-level flow. This shows that the low-level circulation associated with heavy precipitation may still change over places where increases in heavy precipitation are reasonably predicted with thermodynamic constraints (e.g., S_h) and vertical velocity changes are small. Likewise, it shows that changes in the low-level horizontal flow may not influence the vertical velocity, perhaps because of other compensating changes in the horizontal circulation characteristics which are not analyzed here. In lower latitudes, winds associated with heavy precipitation generally weaken, in some places where upward vertical velocity also weakens, but also in places where it strengthens, such as the eastern Equatorial Pacific (Figs. 32j, 40c). The general weakening of tropical low-level winds during heavy events may be a reflection of the weakening mean tropical overturning circulation in response to global warming (Held and Soden 2006; Vecchi et al. 2006; Vecchi and Soden 2007; Chou et al. 2013). Changes in wind speeds associated with heavy precipitation in the NH midlatitudes are smaller and form less coherent patterns than in the SH (Fig. 40c). Over all locations, the wind direction remains relatively constant in the future despite changes in wind magnitude (Figs. 40a,b). When repeating the analysis for DJF and JJA, the strengthening of winds in the SH midlatitudes remains, demonstrating that it is a robust multi-season response, though the strengthening is weaker in JJA (not shown).

4.4.c Discussion of potential mechanisms for low-latitude circulation changes

While a poleward shift in extratropical storm activity appears to influence the projected changes in atmospheric circulation associated with heavy precipitation events in the mid-high latitudes, the mechanisms governing changes in low-latitude circulation features are more complex and regionally dependent. In the low latitudes, changes in vertical velocity accompanying heavy precipitation are large and S_h is a poor predictor of the actual precipitation response (Fig. 32). Enhanced upward vertical velocity is generally associated with strengthening anomalies of ζ850 (Fig. 38e), while decreases in upward velocity are associated with weakening anomalies of PMSL and ζ850 (Figs. 37e, 38e). In either case, the anomalies change strength, while their spatial patterns remain relatively unchanged. A number of recent studies have explored the physical mechanisms responsible for changes in tropical mean precipitation and circulation. It is possible that many of these same mechanisms are important for the changes in atmospheric circulation accompanying heavy precipitation as well.

Increases in heavy precipitation and its associated increased upward velocity in the equatorial Pacific occur over a region of enhanced oceanic warming relative to surrounding areas (Figs. 31-32). The pattern of oceanic warming is associated with increased upward vertical velocity near the equator, enhanced oceanic upward heat flux, positive cloud-radiative feedbacks, and a shift in convective margins toward areas with the enhanced warming, in the climatological mean (Chou et al. 2009; Huang et al. 2013). Considering that the entire daily precipitation distribution shifts toward wetter conditions in this part of the tropics in climate models (see section 3.3.b), it is plausible that the local oceanic warming is also responsible for increases in heavy precipitation intensity and circulation strength. Fig. 31 shows that the enhanced equatorial Pacific warming in

surface temperature is not only present in the climatological mean, but also to a lesser extent when averaged over just heavy precipitation days ($\geq 99^{th}$ percentile). This further supports the hypothesis that the local oceanic warming has a direct influence on the dynamics associated with heavy precipitation. Since latent heat release during tropical heavy precipitation is significant, it is also possible that enhanced heavy precipitation produces a positive feedback on the buoyancy associated with convective updrafts, further strengthening the upward velocity and associated low-level circulation (e.g., Trenberth et al. 2003; Pall et al. 2007). Thus, the mechanisms responsible for the stronger circulation associated with heavy precipitation in the equatorial Pacific may be from a combination of the oceanic warming and positive latent heat feedbacks.

In other parts of the tropics, increases in both heavy precipitation and upward velocity occur over areas with already large P99M in the historical simulation (i.e., the equatorial Atlantic, equatorial Indian Ocean, and Indonesia, Figs. 20, 32). Enhancement of precipitation over wet regions has generally been attributed to increases in the climatological moisture convergence as a result of increased water vapor in a warmer atmosphere (Chou and Neelin 2004; Held and Soden 2006; Chou et al. 2009; Seager et al. 2010). Enhanced mean precipitation over these regions is characterized by a shift in the entire daily precipitation distribution (section 3.3.b), thus also enhancing heavy precipitation. But what causes upward velocity to increase and the low-level circulation anomalies to strengthen during heavy precipitation events? The same latent heat feedback discussed above for the east Equatorial Pacific likely plays a role in these tropical regions as well, especially since precipitation is heavier and associated with substantial latent heat release. Changes in gross moist stability may also be playing a

role. In an analysis of moisture and energy budgets in the tropics, increases in upward velocity accompanying increases in precipitation over parts of convergence zones were shown to be dominated by a convergence feedback arising from decreases in gross moist stability (Chou and Neelin 2004; Chou et al. 2009). It is tempting to suggest that decreases in gross moist stability are also relevant for the increases in upward velocity accompanying heavy precipitation over convergence zones. However, Chou et al. (2013) show that in the climatological and ensemble mean, gross moist stability *increases* almost ubiquitously in the tropics in CMIP5 models, using many of the same models used in this dissertation. Thus, regional decreases in gross moist stability in individual models, which typically only occur over a fraction of the convergence zones (Chou et al. 2009), likely cancel in the ensemble mean. Nonetheless it is possible that the factors controlling changes in gross moist stability, such as the vertical profile of vertical velocity (Chou et al. 2013), behave differently when considering heavy precipitation rather than climatological mean precipitation, such that regional decreases in gross moist stability are important for changes in heavy precipitation even in the ensemble mean. Further analysis would be necessary to explore this interesting possibility.

One final region of interest is the subtropics, where changes in heavy precipitation are not well predicted with thermodynamic constraints and heavy precipitation decreases in some places. The upward velocity and low-level circulation features associated with heavy precipitation weaken over these areas, perhaps most robustly out of any region studied in this chapter. The areas with heavy precipitation decreases coincide with climatological subsidence regions and very low P99M in the historical record (Fig. 20). Over these regions, diabatical heating from large-scale subsidence is balanced by

outgoing longwave radiation in the long-term mean (Chou et al. 2009). Future atmospheric warming and decreases in cloudiness may result in enhanced subsidence to maintain this radiative balance (Chou et al. 2009). It is likely that the enhanced subsidence affects the frequency and intensity of heavy precipitation, which is supported by a shift toward drying in the entire daily precipitation distribution over these regions (section 3.3.b, Fig. 25). Decreasing upward vertical motion during heavy events may therefore be a direct consequence of including more days with very light precipitation (i.e., with weaker ascent or even descent) in the sample of days with precipitation equaling or exceeding the 99th percentile in the future period. Changes in the Hadley circulation may also be influencing the circulation characteristics during heavy precipitation. A closer inspection of Fig. 20 reveals that areas of decreasing P99M are somewhat displaced poleward from the centers of low P99M in the historical period, especially in the South Pacific and South Atlantic subsidence regions. This is consistent with a widening of the Hadley circulation in response to global warming (e.g., Lu et al. 2007; Gastineau et al. 2008; Seager et al. 2010).

There are also areas in the subtropics where heavy precipitation increases while the vertical velocity and low-level circulation associated with it weaken (Fig. 32). One may recognize that these regions often coincide with areas of high climatological tropical cyclone occurrence, and might conclude that decreases in tropical cyclone frequency or intensity in the models contribute to the decreased composite circulation strength. However, recent analysis of tropical cyclones in CMIP5 models not only shows that the models underestimate tropical cyclone frequency and have unrealistic track climatologies, but that projected changes in tropical cyclone frequency are not robust in

any ocean basin (Camargo 2013; Villarini and Vecchi 2013). Therefore, it is unlikely that changes in tropical cyclone frequency play a role in the projected decreased strength in atmospheric circulation in the analysis presented here. Changes in tropical cyclone intensity are usually quantified with large-scale parameterizations rather than cyclone tracking in course resolution simulations such as in CMIP5 (Camargo 2013; Villarini and Vecchi 2013), so it is unclear how changes in tropical cyclone intensity may be related to the changes in the composite circulation strength shown here. Projected decreases in upward velocity and low-level circulation strength in areas with increases in heavy precipitation may simply be a reflection of the climatological weakening of the tropical overturning circulation that has been comprehensively discussed in previous studies (e.g., Held and Soden 2006; Vecchi and Soden 2007). In the long-term mean, decreased upward velocity despite increases in precipitation can be explained through energy balance arguments, in which increases in gross moist stability over converging regions results in a negative feedback on the upward velocity, reducing ascent (Chou and Neelin 2004; Chou et al. 2009). Since mean vertical velocity during heavy precipitation events is upward (i.e., positive convergence) over these areas (not shown) and gross moist stability likely increases (Chou et al. 2013), it is plausible that this same dynamical feedback operates during heavy precipitation events.

4.5 Summary and discussion of limitations

The regional projected changes in heavy precipitation were comprehensively explored in this chapter. A thermodynamic scaling proposed by O'Gorman and Schneider 2009a,b), which accounts for local increases in atmospheric moisture and

changes in the moist adiabatic lapse rate with warming, performs better than simple Clausius-Clapeyron scaling when predicting increases in local heavy precipitation in response to warming. However, thermodynamic changes alone cannot explain projected changes in heavy precipitation in the low and high latitudes, where changes in the vertical velocity accompanying heavy precipitation are substantial, and heavy precipitation decreases in some places. In the low latitudes, the large-scale low-level circulation anomalies change strength in accordance with vertical velocity. The relationship between vertical velocity and the horizontal circulation is more complex in the mid to high latitudes; in the Southern Hemisphere, changes in the large-scale horizontal circulation are not always associated with those in vertical velocity; in the Northern Hemisphere, the large-scale synoptic forcing for ascent (quantified with **Q**-vector convergence) does not change in the same qualitative sense as vertical velocity. One robust finding from this chapter is that the atmospheric circulation patterns accompanying heavy precipitation do not change despite changes in the strength of the circulation features over some places. This suggests that the physical mechanisms that produce local heavy precipitation, including surface cyclones, fronts, or shortwave troughs, may remain the same in a future climate but may strengthen or weaken.

There are a few limitations in the analysis presented in this chapter that are worth noting. For one, the physical mechanisms unique to individual extreme precipitation events may be averaged out when developing composites for a sample of heavy precipitation events as done here. A better understanding of the variety of atmospheric phenomena that produce extreme precipitation at individual locations and how they may change in the future would require further analysis. Another limitation of the analysis is

that CMIP5 models do not adequately simulate some of the mechanisms that are important for heavy precipitation, such as tropical cyclones and the MJO (Jones and Carvalho 2012; Camargo 2013; Hung et al. 2013). Thus, the impacts of such mechanisms on heavy precipitation intensity and its associated circulation are not well represented. Finally, the relatively coarse resolution of the climate model output analyzed here does not allow for the investigation of small-scale processes that may be important for changes in extreme precipitation locally, such as mesoscale precipitation bands or convective systems, and may also result in underestimations in projected increases in heavy precipitation (e.g., Allan and Soden 2008; Min et al. 2011; Wuebbles et al. 2013). The analysis is therefore limited to large-scale heavy precipitation and its associated large-scale circulation features. Based on the ability of climate models to realistically simulate the large-scale circulation associated with heavy precipitation (see chapter 2), however, we may have some confidence in projections at this spatial scale.

5. Discussion and Conclusions

5.1 Summary of CMIP3 and CMIP5 evaluation

Various aspects of daily precipitation statistics from an ensemble of 17 CMIP3 models were evaluated by comparing the model output with gridded observations from the CPC over North America. Heavy and extreme precipitation intensities are too light in the models over the southeastern United States, southern Mexico, and along the Pacific coast, and are too heavy in intermountain regions of western North America including north-central Mexico. These model biases are quite robust amongst most or all of the CMIP3 models studied. When looking at the entire daily precipitation distribution in CMIP3, the models overestimate light precipitation intensities and underestimate heavy precipitation intensities to an extent that varies with geographic location. On a positive note, the CMIP3 models generate fairly realistic heavy precipitation in northeastern North America and capture the seasonal cycle of heavy precipitation quite well over parts of the study domain. These findings are consistent with previous studies that have evaluated global and regional climate models over a wide variety of geographical locations, using various observational data sources and different methods to quantify heavy and extreme precipitation.

An analysis of the large-scale physical mechanisms associated with extreme precipitation events was conducted for a subset of the CMIP3 models that were used to study precipitation statistics. The models realistically simulate the gross patterns of sea level pressure and geopotential height anomalies associated with extreme events across most of North America. However, there is a tendency for the models to overestimate

gradients in sea level pressure and geopotential height anomalies during extreme events, which in turn results in overestimated low-level winds, column integrated moisture anomalies, and **Q**-vector convergence over parts of the domain. This analysis showed that there is no simple relationship between model biases in circulation strength and biases in heavy precipitation, as the models produced realistic or too strong circulations in regions where heavy precipitation was underestimated, overestimated, or realistic. This suggests that other physical deficiencies in the models are important for model biases in heavy precipitation. Such deficiencies may include problems simulating convective precipitation and tropical cyclones, unrealistically smooth topography as a result of the coarse model resolutions over mountainous regions, and problems simulating mesoscale processes. Previous studies indicate that a combination of increasing the resolution at which climate models are run and adjusting various aspects of convective parameterizations may substantially improve the biases in simulated high frequency precipitation generated by such physical problems (Colle and Mass 2000; Iorio et al. 2004; Emori et al. 2005; Kimoto et al. 2005; Kharin et al. 2007; Wilcox and Donner 2007; Wehner et al. 2010; Dulière et al. 2011; Li et al. 2012).

An ensemble of 17 CMIP5 models were also evaluated and compared with CMIP3. Heavy precipitation biases in CMIP5 are generally similar to those in CMIP3. However, underestimations in heavy precipitation in the southeastern United States are smaller in CMIP5, and overestimations in the intermountain regions are somewhat larger. An analysis of the atmospheric circulation associated with heavy to extreme daily precipitation events in the CMIP5 ensemble also revealed no simple relationship between biases in atmospheric circulation and those in heavy precipitation. Indeed, the large-scale

atmospheric dynamics accompanying heavy precipitation events are nearly identical in the CMIP3 and CMIP5 ensembles. This suggests that other physical differences between the CMIP ensembles, including the typical horizontal resolutions and convective parameterizations, are important for the small improvements in CMIP5 over CMIP3.

The results of the model evaluation presented in this dissertation are encouraging because they show that CMIP3 and CMIP5 models simulate the atmospheric circulation associated with extreme precipitation events rather well even though they incorrectly simulate the frequency and intensity of daily precipitation over many places. This suggests that climate models may be useful for predicting and understanding future changes in the large scale physical mechanisms associated with extreme precipitation in response to global warming. However, a better understanding of the physical deficiencies in climate models is necessary to be able to use these models to reliably predict quantitative changes in high frequency precipitation statistics in response to global warming. Such an understanding requires additional studies that evaluate climate model components in a more detailed and controlled fashion than presented here.

5.2 Summary of projected changes in the daily precipitation distribution

The CMIP5 models were used to study projected changes in the daily precipitation distribution in response to atmospheric warming. Histograms of daily precipitation were produced at every grid cell for both the historical and RCP8.5 simulations, and the historical histograms were subtracted from the RCP8.5 histograms. K-means cluster analysis was applied to the difference histograms at all grid cells to summarize the regional patterns of projected changes in the daily precipitation

distribution. From the analysis, four distinct responses of the precipitation distribution were detected in the CMIP5 ensemble mean, characterized by down-up, up-down-up, up-down, and down-up-down-up shapes (see Table 3 for further description and summary of where the responses occur). Changes in the precipitation distribution that fall into one of the categories of Table 3 were detected at individual grid cells as well as in the regional mean with fairly high robustness, suggesting that individual locations may experience precipitation changes characterized by one of these categories in response to future warming. However, due to the inherently noisy nature of daily precipitation, there is still a fair amount of scatter in the precipitation response at individual locations. Thus, projected changes in the precipitation distribution shown in this dissertation are most robust only when considering large-scale regional averages. The individual CMIP5 models disagree on the exact spatial patterns of the daily precipitation distribution response. However, when averaged over large regions with similar changes in the precipitation distribution determined from the ensemble mean, the individual models closely agree on the general shape of changes in the precipitation distribution.

The most robust responses of the daily precipitation distribution, characterized by the down-up or up-down-up shapes of the difference histograms, appear to correspond broadly with projected changes in surface temperature and atmospheric circulation. That is, tropical regions with the increased precipitation down-up behavior coincide with regions where mean oceanic warming exceeds surrounding areas. Additionally, a poleward shift in storm activity appears to be related to increased precipitation of all intensities in the high latitudes and decreased light to moderate precipitation at lower latitudes. Changes in the Hadley circulation may be linked to decreases in precipitation

of all intensities over dry subtropical subsidence regions (e.g., Lu et al. 2007; Gastineau et al. 2008; Chou et al. 2009; Seager et al. 2010). Projected changes of the daily precipitation distribution over the tropical oceans may also reflect a redistribution of cloud/precipitation regimes in response to changes in sea surface temperatures and atmospheric circulation (Lau and Wu 2011).

In Loikith et al. (2013), cluster analysis was used to study the regional variability of the daily temperature distribution in the present climate. Here, cluster analysis was not only applied to daily precipitation, a variable that is spatially noisier and has a more skewed distribution, but also to differences in the distribution between two climate scenarios. This shows the general applicability of cluster analysis to objectively summarize spatial characteristics of the high-frequency distribution of atmospheric variables and their response to climate forcing. As shown here, cluster analysis may be used to objectively classify individual locations into regions with physically meaningful similarities in the precipitation response to atmospheric warming. Developing regions in this way is arguably better than arbitrarily defining them based on political boundaries or other criteria that have little physical basis.

5.3 Summary of physical mechanisms for heavy precipitation changes

Projected regional changes in heavy precipitation and the circulation characteristics accompanying heavy events were comprehensively explored in the CMIP5 ensemble. In the future (RCP8.5) simulation, heavy precipitation is projected to increase almost everywhere globally, with the exception of dry subtropical oceanic regions. Seasonally, some of these areas of decrease are more widespread and include nearby land

regions. A thermodynamic scaling introduced by O'Gorman and Schneider (2009b), which accounts for local increases in atmospheric moisture and changes in the moist adiabatic lapse rate with warming, reasonably predicts increases in midlatitude heavy precipitation in the model ensemble. However, changes in heavy precipitation in the northern high latitudes and parts of the tropics are larger than predicted with the scaling, while they are smaller than the scaling (or negative) in other parts of the tropics. In these regions, changes in upward vertical velocity are necessary to explain the local response of heavy precipitation, consistent with the findings in O'Gorman and Schneider (2009b) and Sugiyama et al. (2010). When considering the global median sensitivity of heavy precipitation, however, local changes in vertical velocity are less relevant and the thermodynamic scaling is a sufficient predictor. Annually, the global sensitivity of the most extreme daily precipitation events is centered at 7% K^{-1} in the model ensemble, suggesting that simple Clausius-Clapeyron water vapor scaling is a sufficient global predictor for these most extreme cases.

The horizontal atmospheric circulation features associated with heavy precipitation were explored to more closely see how changes in these features relate to changes in heavy precipitation and upward vertical velocity. The analysis was based on composites of the atmospheric circulation during heavy precipitation events at individual grid cells. In the tropics, low-level circulation features associated with heavy precipitation weaken where there are decreases in heavy precipitation and upward velocity. In particular, the weakening is characterized by smaller standardized anomalies of sea level pressure, 850 mb vorticity, and 500 mb geopotential height in the future simulation. When exploring composite patterns at individual locations, the sign of

changes for some of these quantities is robust among individual models and the changes are statistically significant over coherent areas. In parts of the deep tropics, increases in heavy precipitation that exceed thermodynamic predictions coincide with strengthening anomalies of 850 mb vorticity and enhanced upward vertical motion. Other metrics that were explored, such as anomalies in sea level pressure, seem to have little spatial definition in deep tropical regions. In all cases where the low-level circulation changes strength, the spatial patterns of the composite circulation remain relatively unchanged in the future. This suggests that the physical mechanisms relevant for local heavy precipitation may not change in the future, but may be characterized by stronger or weaker features. However, a more in-depth investigation of the physical mechanisms associated with individual extreme precipitation events, rather than the composite of many events, may be necessary to confirm that this is true. The broader mechanisms responsible for changes in the atmospheric circulation associated with heavy precipitation in the tropics may be complex and depend on the region and sign of change. They include an equatorial enhancement in oceanic warming, increases in moisture over already convergent regions, feedbacks between latent heat release and upward velocity, changes in the strength and pattern of subsidence, and possible dynamical feedbacks associated with changes in gross moist stability.

The atmospheric circulation accompanying heavy precipitation also changes in high-latitude regions. These changes, including strengthening low-level circulation anomalies in both hemispheres and stronger low-level winds in the southern hemisphere, appear to be related to a poleward shift and possibly intensification of climatological storm tracks (e.g., Yin 2005; O'Gorman 2010; Chang et al. 2012). Like in the case of

low latitudes, changes in circulation strength occur while spatial patterns of the circulation remain unchanged. Changes in circulation strength in high latitudes do not necessarily translate to changes in vertical velocity associated with heavy precipitation, however. In the Southern Hemisphere, changes in vertical velocity are small and increases in heavy precipitation are reasonably predicted with the thermodynamic scaling, despite the rather potent strengthening of sea level pressure anomalies and low-level wind accompanying heavy precipitation. In the Northern Hemisphere, increases in upward vertical velocity occur in the same areas that low-level circulation anomalies strengthen, but decreases in **Q**-vector convergence also occur over some of these areas. This suggests that the strengthening circulation anomalies are not also accompanied by strengthening in gradients of pressure, temperature, and vorticity, which may also force ascent. The results show that the relationship between low-level circulation and upward velocity in the extratropics is more complex than at lower latitudes, and that changes in low-level circulation may occur even if vertical velocity remains relatively constant. A more comprehensive analysis of the large-scale circulation over these regions than presented here would be necessary to better understand these complex circulation changes. In the midlatitudes, changes in the horizontal and vertical circulation during heavy precipitation were shown to be small in all analyses, consistent with earlier studies (Gutowski et al. 2008b; Sugiyama et al. 2010). However, mechanisms that may be important for changes in midlatitude heavy precipitation, such as tropical cyclones and teleconnections associated with the MJO, may not be well represented in the CMIP5 models used for this analysis (Jones and Carvalho 2012; Camargo 2013; Hung et al. 2013).

5.4 Discussion of implications, limitations, and future directions

An in-depth analysis of state-of-the-art coupled climate simulations shows that there may be substantial and profound regional changes in the frequency distribution of daily precipitation in response to future global warming. Over most land regions, the frequency and intensity of heavy to extreme precipitation is projected to increase. These increases may result in increased flooding and subsequently loss of life and property over many places. At the same time, light to moderate precipitation events may become less frequent over places with projected increases in heavy precipitation and which have large population densities, such as middle and low-latitude land regions. This may result in more frequent, longer, and/or more intense droughts in between extreme precipitation events, which would likely impact agriculture and water resources in a significant way. It is clear that the effect of global warming on precipitation may have serious impacts on human life, property, and ecosystems around the world.

The projected changes in daily precipitation statistics presented in this dissertation come with substantial uncertainty, mostly because of disagreements between individual models and substantial biases in the simulation of observed precipitation statistics over the recent past. The models generally underestimate heavy precipitation over wet regions. If such biases translate to projected changes in response to warming (i.e., underestimating increases in heavy precipitation over wet regions), future increases in heavy precipitation over areas already susceptible to extreme precipitation may be larger than climate models predict. One limitation in this dissertation is that the analysis period was too short to evaluate late 20^{th} century changes in heavy precipitation. However,

several previous studies that have evaluated late 20th century changes (discussed and cited in section 1.2) suggest that the underestimation of future increases in extreme precipitation in climate models is likely. Another aspect of model biases to be considered is overestimations in light precipitation, which occur nearly everywhere (Fig. 5). If these overestimations translate to projected changes, it is possible that the models may *overestimate* the projected decreases in the frequency of light to moderate precipitation over some places. Though light-moderate precipitation has decreased with warming over large tropical regions in observations, consistent with model projections of future climate (Lau and Wu 2011; Lintner et al. 2012), some studies show that light-moderate precipitation has increased over midlatitude regions where the models simulate decreases (Karl and Knight 1998). The latter may be consistent with climate models over-exaggerating the decreased frequency of light-moderate precipitation in response to warming as a result of too high frequencies of light precipitation in the present climate. Another possibility is that local processes relevant for changes in the precipitation distribution, such as changes in land use and irrigation, are not adequately represented in the models (e.g., DeAngelis et al. 2010). There is a need for more comprehensive regional analyses of observed changes in the frequency distribution of precipitation to better assess the plausibility of the projected regional changes in the CMIP5 ensemble. This need is challenged by the lack of a reliable, spatially homogeneous, and temporally sufficient network of high frequency precipitation observations over global land and oceans.

Large intermodel variability in the projected changes of precipitation represents another source of uncertainty for future projections. Taking the ensemble mean allows

for the emergence of regional precipitation changes that are potentially more robust across the models, but does not necessarily lead to the most realistic projections; it is possible that certain individual models are more reliable than the ensemble mean. Determining which models are more reliable requires an in-depth understanding of the physical reasons for the large intermodel spread and an intensive comparison of simulations with observations. As mentioned in section 5.1, there is a need for more comprehensive climate model evaluations focusing on the intercomparison of individual models and their physical components. Additionally, a better understanding of the relationship between changes in precipitation and changes in other physical processes in climate models, such as radiation or circulation, is necessary and may prove useful. Assuming that these relationships hold in the real climate system, observations of variables related to the physical processes, which may be more reliable than precipitation observations, could possibly be used to constrain the intermodel spread in projections.

The relatively realistic simulation of the large-scale thermodynamical and dynamical forcing for extreme precipitation in the CMIP models is reassuring. It suggests that the physical mechanisms for changes in heavy precipitation are reliable and that the qualitative response of heavy precipitation is also reliable. However, the methodology employed in this dissertation to explore changes in heavy precipitation has limitations; in order to comprehensively explore spatial variability at the grid cell scale, heavy precipitation was averaged over individual events as well as many models. Taking the model ensemble mean masks unique regional precipitation changes and physical mechanisms that are important in the real climate system but do not emerge in the ensemble mean due to large intermodel variability. For instance, regional decreases in

gross moist stability or advection of dry air near convective margins, the latter known as the “upped-ante” mechanism (Neelin et al. 2003), are important in individual simulations but typically occur in different places in different models (e.g., Chou et al. 2009). Averaging over many heavy precipitation events has the potential to smooth over a variety of potentially important physical mechanisms unique to individual events, possibly generating misleading results. It is possible that the proportion of extreme precipitation events associated with certain phenomena, such as convection or extratropical cyclones, changes in the future, which may not be obvious in a composite analysis. Since the average daily intensity of precipitation originating from certain types of events, such as convection, may be larger than from other types (Haerter and Berg 2009), it is important to know if the proportion of such events changes.

To address the shortcomings discussed above and to obtain a more thorough understanding of the complex dynamical mechanisms responsible for changes in heavy precipitation over certain locations, a more in-depth intermodel and individual event analysis over particular regions would be necessary. Regions of interest include 1) the deep tropics, where the large-scale circulation features in a composite have weak spatial definition, 2) the midlatitudes, which may be susceptible to changes in the fraction of extreme events caused by convection, synoptic-scale cyclones, or other phenomena, and 3) the storm track regions where complex features of the atmospheric circulation are important for producing upward vertical velocity. In performing the above regional analyses, higher resolution regional models should also be used in conjunction with coarser resolution global models to better represent and evaluate the role of tropical cyclones and mesoscale processes. Finally, the 21-year time periods used in this

dissertation were potentially too short to capture the rarest and most impactful precipitation events that affect individual locations. To quantify truly extreme precipitation, the use of longer time periods or more elaborate statistical procedures would be necessary.

Tables

Modeling Group	Country	Model Name	Run #	Spatial Resolution (lon x lat)
Canadian Centre for Climate Modelling & Analysis	Canada	CCCMA-CGCM3.1(T47)* CCCMA-CGCM3.1(T63)*	1 1	3.75° x 3.75° 2.81° x 2.81°
Centre National de Recherches Météorologiques	France	CNRM-CM 3*	1	2.81° x 2.81°
CSIRO Atmospheric Research	Australia	CSIRO-Mk3.0* CSIRO-Mk3.5*	1 1	1.88° x 1.88° * 1.88° x 1.88° *
Geophysical Fluid Dynamics Laboratory	USA	GFDL-CM2.0* GFDL-CM2.1*	1 2	2.50° x 2.00° * 2.50° x 2.00° *
Goddard Institute for Space Studies	USA	GISS-AOM* GISS-EH* GISS-ER*	1 5 1	4.00° x 3.00° 5.00° x 3.91° 5.00° x 3.91°
Institute of Atmospheric Physics	China	IAP-FGOALS-g1.0	1	2.81° x 3.00°
Institute for Numerical Mathematics	Russia	INM-CM3.0	1	5.00° x 4.00°
Center for Climate System Research, National Institute for Environmental Studies, and Frontier Research Center for Global Change	Japan	MIROC3.2(medres)	1	2.81° x 2.81°
Max Planck Institute for Meteorology	Germany	MPI-ECHAM5*	1	1.88° x 1.88° *
Meteorological Research Institute	Japan	MRI-CGCM2.3.2*	1	2.81° x 2.81°
National Center for Atmospheric Research	USA	NCAR-CCSM3 NCAR-PCM	1 1	1.41° x 1.41° * 2.81° x 2.81°

Table 1. List of the CMIP3 models used for analysis in chapter 2 of the dissertation. All 17 models were used for the analysis of precipitation statistics. Due to output availability, only the 12 models with asterisks next to the model name were included in the analysis of physical mechanisms associated with extreme precipitation events. These same 12 models were used in the comparison with CMIP5 in section 2.5, for both precipitation statistics and the physical mechanisms accompanying heavy precipitation. The approximate spatial resolutions were calculated by dividing 360° or 180° by the number of grid cells in the longitude or latitude dimensions, respectively. Asterisks next to spatial resolution denote climate models whose grids were transformed to the common 2.5°x2.5° resolution using area averaging. All others were transformed using linear

interpolation. The ensemble member number used for each model is indicated. [Further documentation for individual models, including expansions of all acronyms, is available online at http://www-pcmdi.llnl.gov/ipcc/model_documentation/ipcc_model_documentation.php.]

Modeling Group	Country	Model Name	Spatial Resolution (lon x lat)
Beijing Climate Center, China Meteorological Administration	China	BCC-CSM1.1	2.81° x 2.81°
Canadian Centre for Climate Modelling and Analysis	Canada	CanESM2	2.81° x 2.81°
Centre National de Recherches Meteorologiques / Centre Europeen de Recherche et Formation Avancees en Calcul Scientifique	France	CNRM-CM5	1.41° x 1.41° *
Commonwealth Scientific and Industrial Research Organization in collaboration with Queensland Climate Change Centre of Excellence	Australia	CSIRO-Mk3.6.0	1.88° x 1.88° *
LASG, Institute of Atmospheric Physics, Chinese Academy of Sciences	China	FGOALS-s2	2.81° x 1.67° *
NOAA Geophysical Fluid Dynamics Laboratory	USA	GFDL-ESM2G GFDL-ESM2M	2.50° x 2.00° * 2.50° x 2.00° *
Met Office Hadley Centre	UK	HadGEM2-CC	1.88° x 1.25° *
Institute for Numerical Mathematics	Russia	INM-CM4	2.00° x 1.50° *
Institut Pierre-Simon Laplace	France	IPSL-CM5A-LR IPSL-CM5A-MR	3.75° x 1.88° 2.50° x 1.26° *
Japan Agency for Marine-Earth Science and Technology, Atmosphere and Ocean Research Institute (The University of Tokyo), and National Institute for Environmental Studies	Japan	MIROC-ESM MIROC-ESM-CHEM	2.81° x 2.81° 2.81° x 2.81°
Atmosphere and Ocean Research Institute (The University of Tokyo), National Institute for Environmental Studies, and Japan Agency for Marine-Earth Science and Technology	Japan	MIROC5	1.41° x 1.41° *
Max Planck Institute for Meteorology	Germany	MPI-ESM-LR MPI-ESM-MR	1.88° x 1.88° * 1.88° x 1.88° *
Meteorological Research Institute	Japan	MRI-CGCM3	1.13° x 1.13° *

Table 2. As in Table 1 but for the CMIP5 models used for analysis in this dissertation (sections 2.5 and chapters 3-4). All models listed have archived output of precipitation and other variables necessary for the study of physical mechanisms. Ensemble member run # 1 was used for all models.

Type	Description	Location	Robustness
down-up	Decreasing zero/trace days (and also very light events in some cases), increasing larger events of all sizes	High latitudes, parts of the tropical oceans near the equator, east Africa and adjacent Indian Ocean	High
up-down-up	Increasing zero/trace days (and also very light events in some cases), decreasing light-moderate events, increasing heavy events	Midlatitudes, subtropics, and parts of the tropics	Fairly high
up-down	Increasing zero/trace days (and also very light events in some cases), decreasing light, moderate, and heavy events	Tropical and subtropical oceanic dry areas with projected decreases in mean and heavy precipitation	Fairly high in small regions
down-up-down-up	Decreasing zero/trace days, increasing very light events, decreasing light-moderate events, increasing heavy events	Scattered small oceanic areas within 10-30° latitudes	Low

Table 3. Summary of the distinct regional responses of the daily precipitation distribution resulting from the cluster analyses in chapter 3 of the dissertation. The robustness was subjectively determined from the spread of count differences among individual grid cells within the clusters corresponding to each type, the geographical coherence and extent of the type, the dominance in the emergence of the type from the cluster analyses, and the intermodel agreement of the precipitation response.

Figures

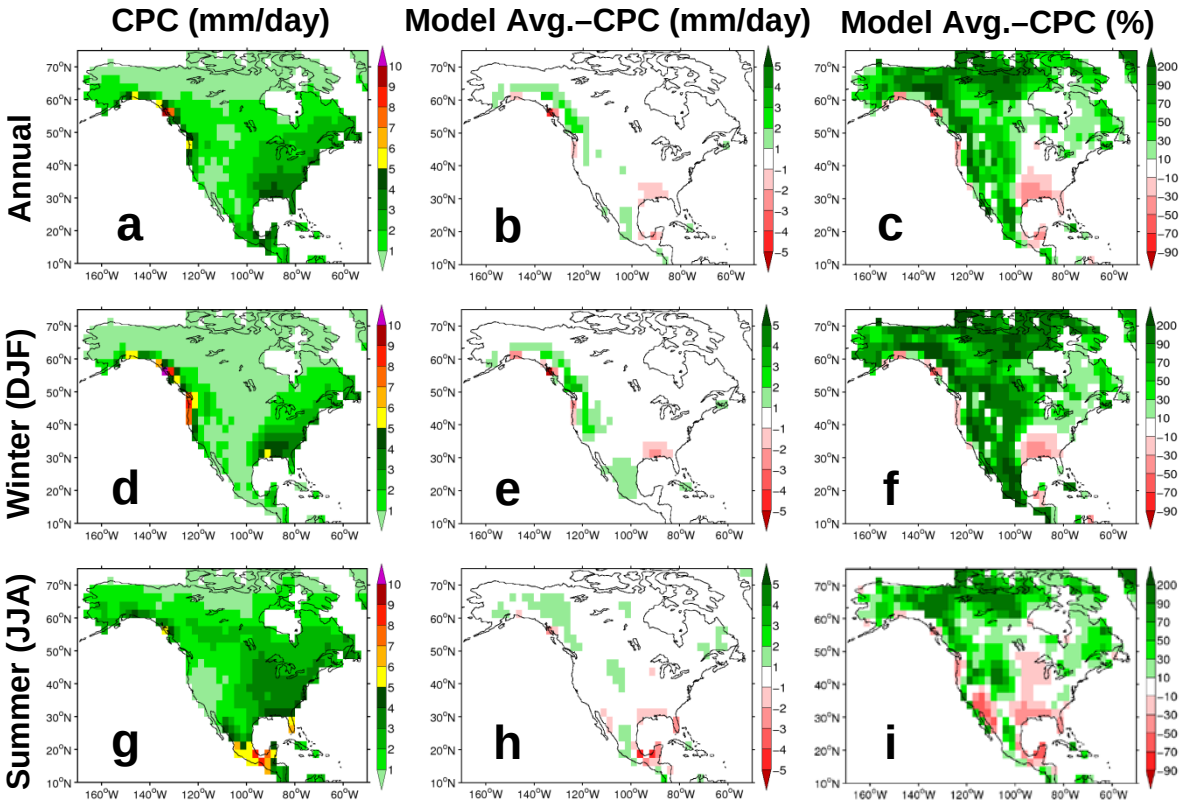

Figure. 1. Daily mean precipitation over the period 1979-99 at each grid cell on the 2.5° grid for (a)-(c) all seasons, (d)-(f) winter, and (g)-(i) summer. (left) Mean precipitation for the CPC observations, (middle) the difference between the CMIP3 model average and CPC in units of mm day^{-1}, and (right) the percent difference between the CMIP3 model average and CPC.

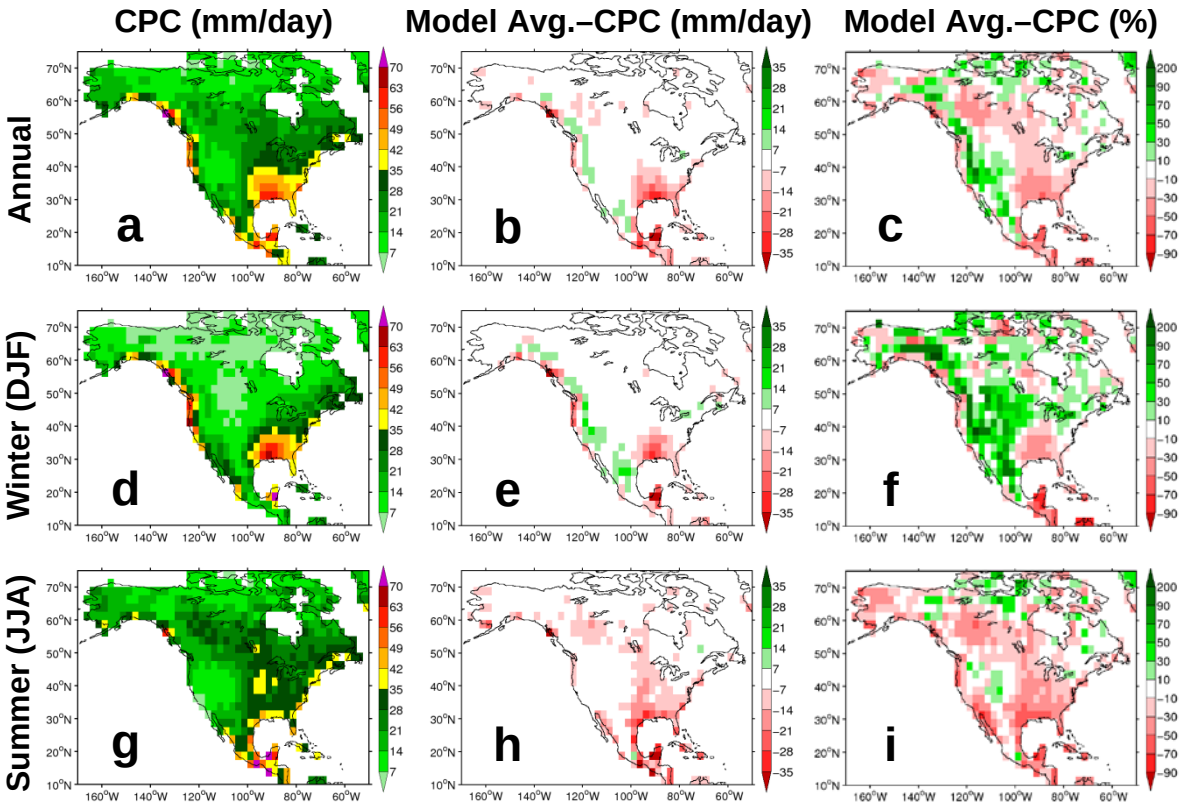

Figure. 2. As in Fig. 1, but for the mean precipitation falling from the wettest 1% of days (P99M, as defined in section 2.3).

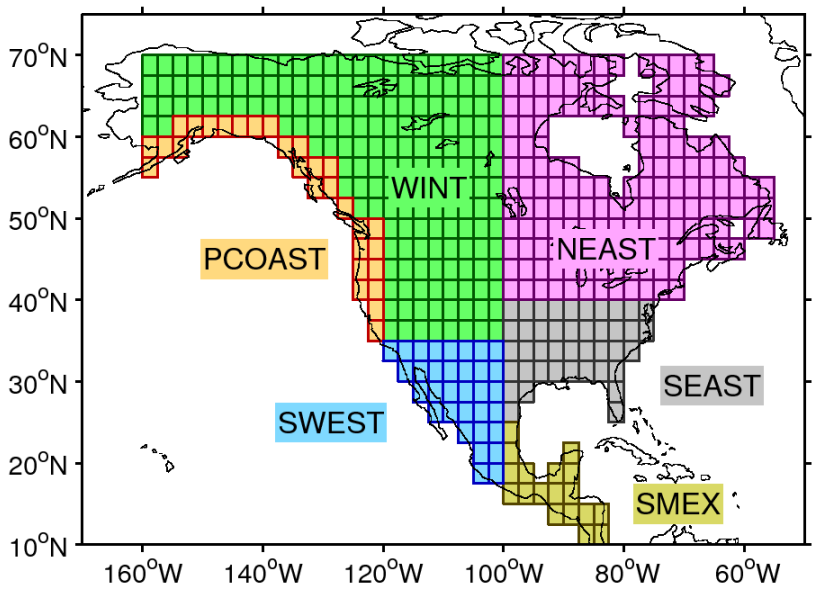

Figure. 3. Analysis regions used to study the model variability of P99M biases and daily precipitation distributions (Figs. 4 and 5, respectively). The specific 2.5°x2.5° grid cells constituting each region are shown. The regions are named according to geographic location: Pacific Coast (PCOAST), West Interior (WINT), Northeast (NEAST), Southeast (SEAST), Southwest (SWEST), and Southern Mexico/ Central America (SMEX). Note that grid cells along the far northern, western, and eastern parts of the domain were omitted from the regions due to potential uncertainties in the CPC observations over these locations (Chen et al. 2008c).

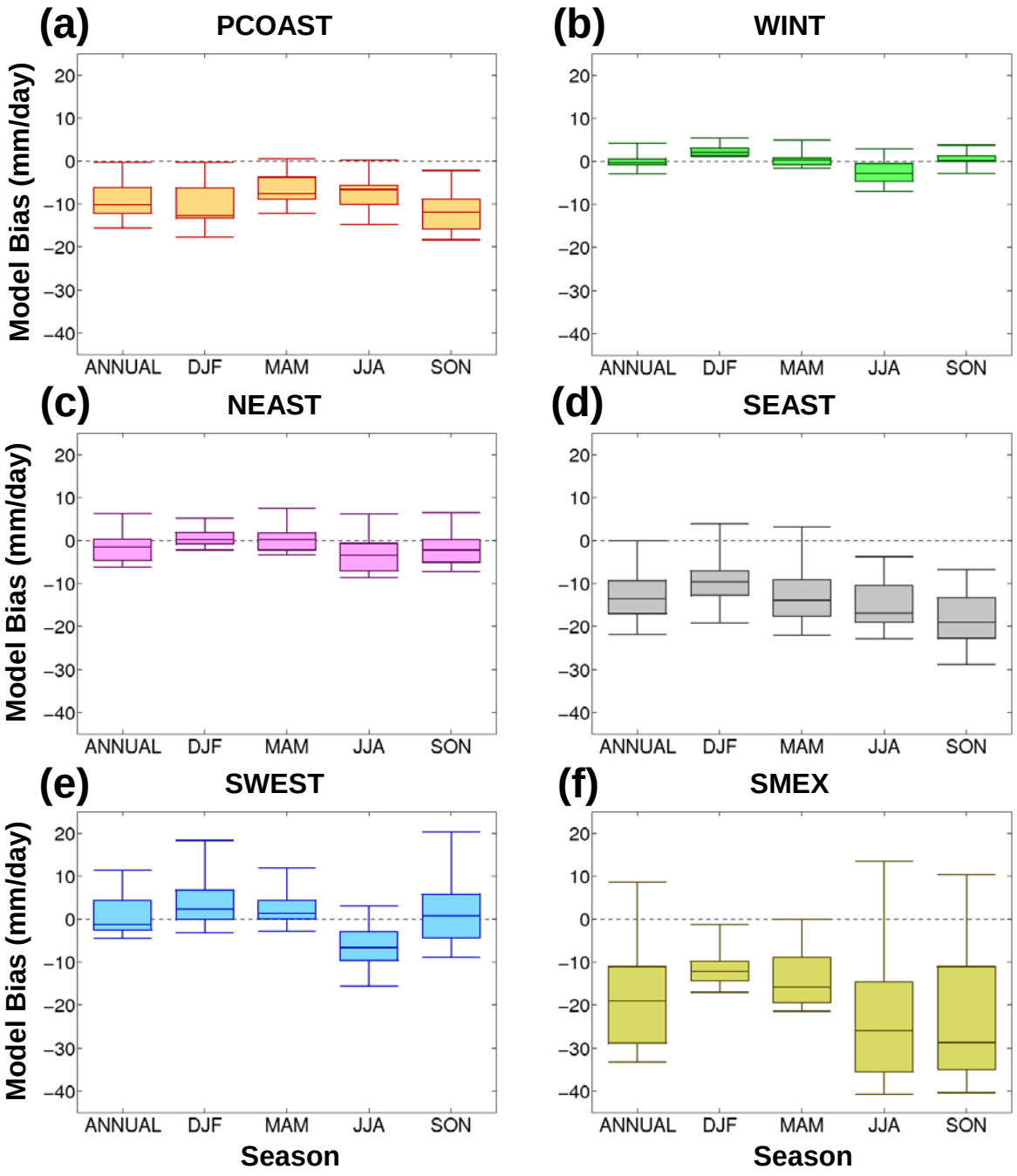

Figure. 4. Box-and-whisker plots showing the variability of CMIP3 model biases in P99M averaged over the specified regions (Fig. 3). The horizontal lines on the box-and-whiskers indicate the minimum, 25th percentile, median, 75th percentile, and maximum biases of the individual models.

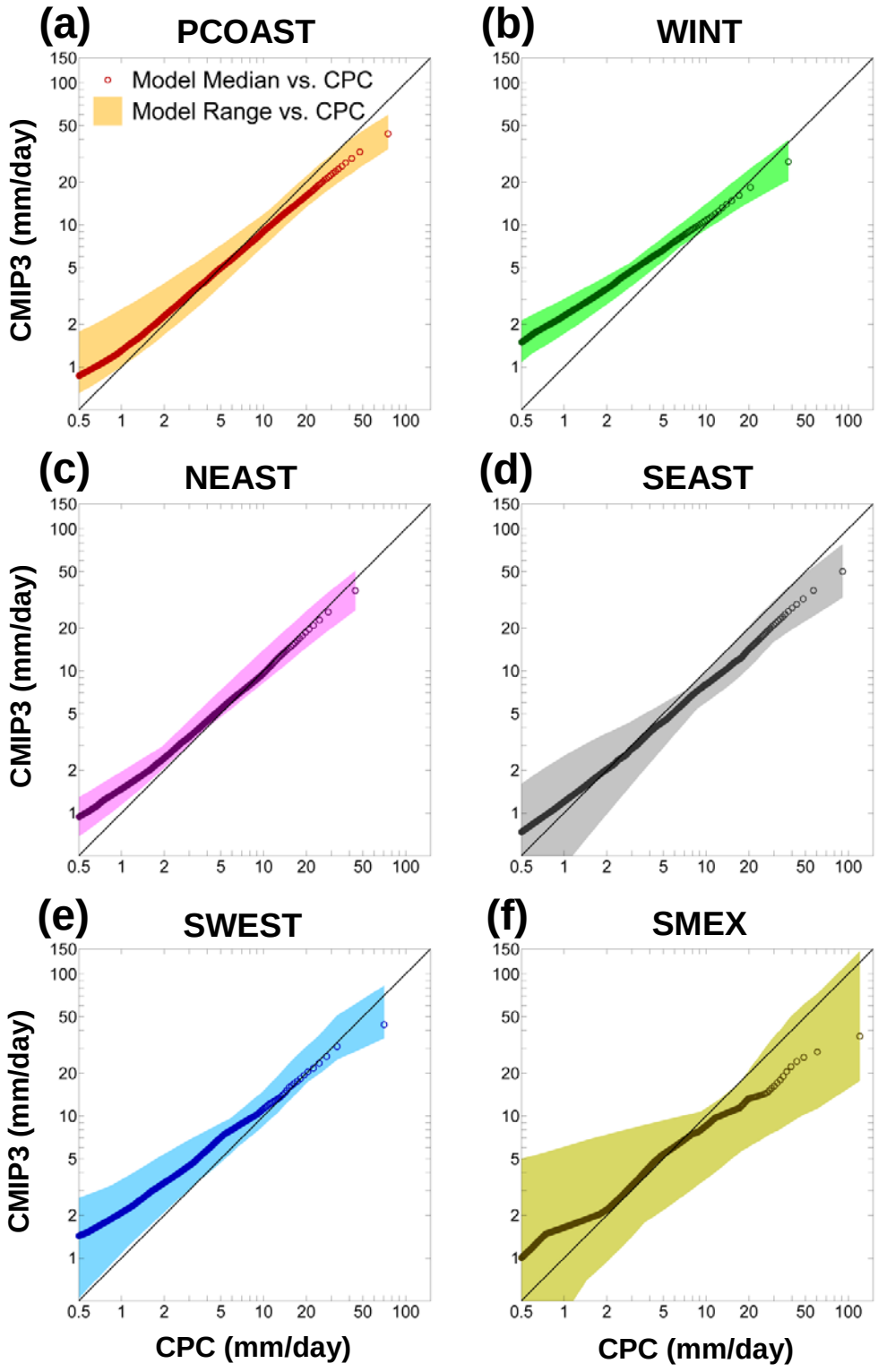

Figure. 5. *Q-Q* plots comparing the annual daily precipitation distribution between the CPC observations and CMIP3 models for each of the regions shown in Fig. 3 (see section

2.3 for details). In all cases, the circles are showing the model median precipitation value corresponding to each CPC value. The shading is showing the lowest to highest CMIP3 model precipitation value for each corresponding CPC value. Values are plotted only for percentiles for which the CPC precipitation is at least 0.5 mm day^{-1}. The abscissa and ordinate axes are on a logarithmic scale due to the nonlinearity of daily precipitation distributions. The solid black line is a 1:1 line indicating where all data points would fall if there were perfect agreement between the models and observations.

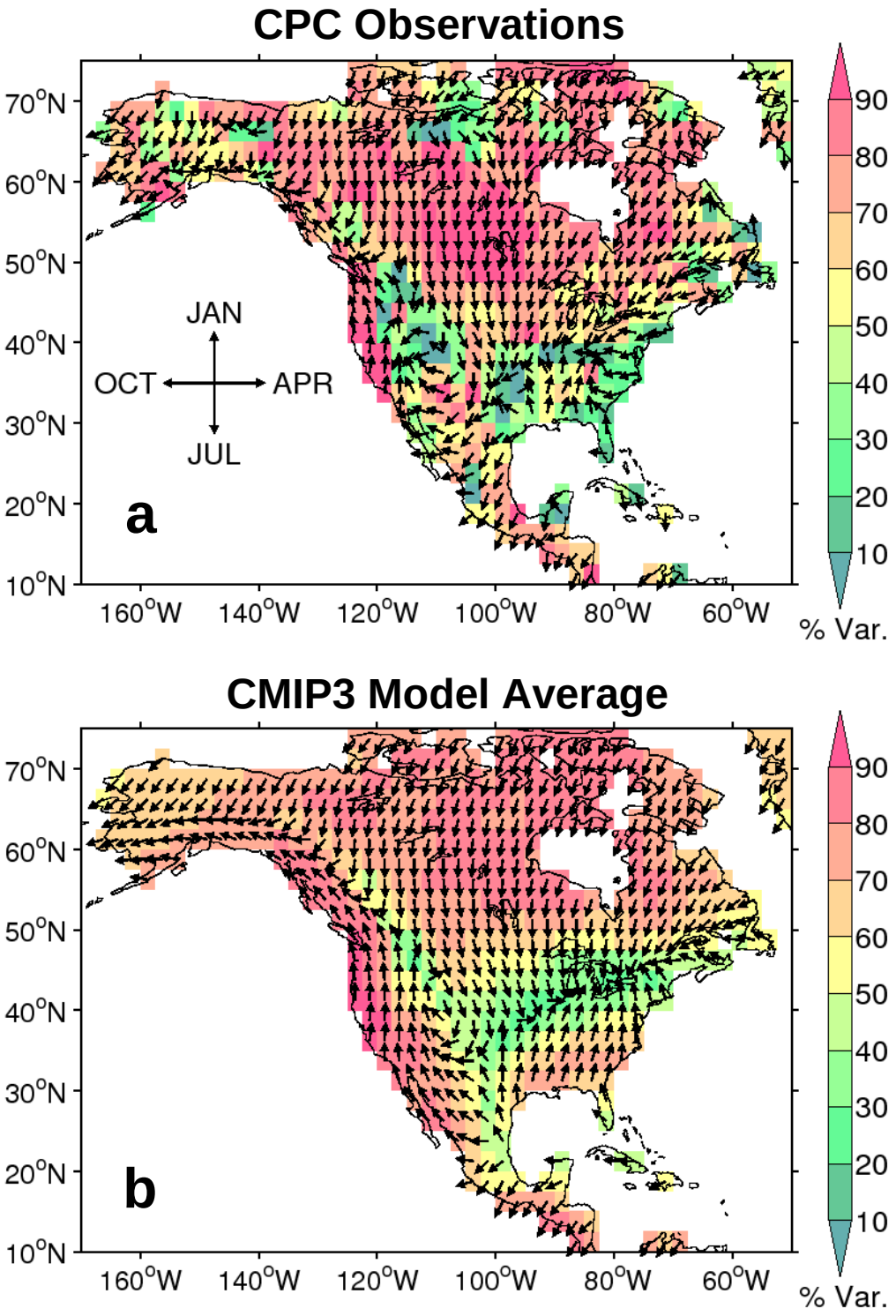

Figure. 6. The seasonal cycle of heavy precipitation, as determined by the first harmonic of the P99M precipitation for each calendar month (see section 2.3 for details) for (a) the

CPC observations and (b) the CMIP3 model average. The vectors point in the direction of the seasonal maximum of P99M objectively determined by the harmonic fit, following the legend shown in (a). Color fills show the percentage of total variance of monthly P99M that the first harmonic explains.

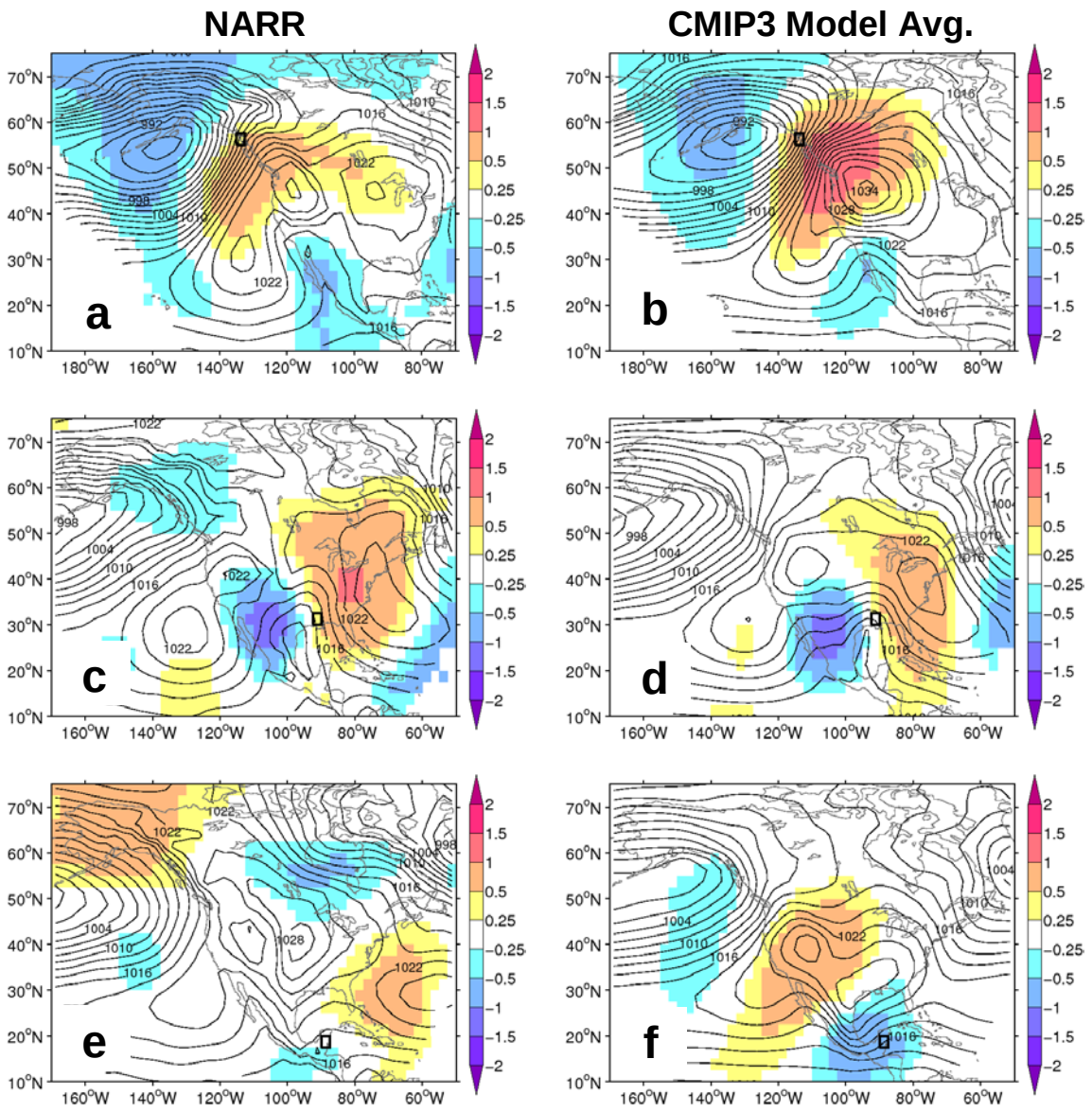

Figure. 7. Composites of pressure at mean sea level (PMSL, hPa, contours) and 500 mb geopotential height standardized anomalies (Z500*, dimensionless, color fills) for the 21 most extreme winter (DJF) precipitation events at selected grid cells (indicated by black rectangles) over which the models severely underestimate P99M precipitation. Sea level pressure is contoured every 2 hPa. (left) Composites based on NARR and (right) those averaged over all CMIP3 models.

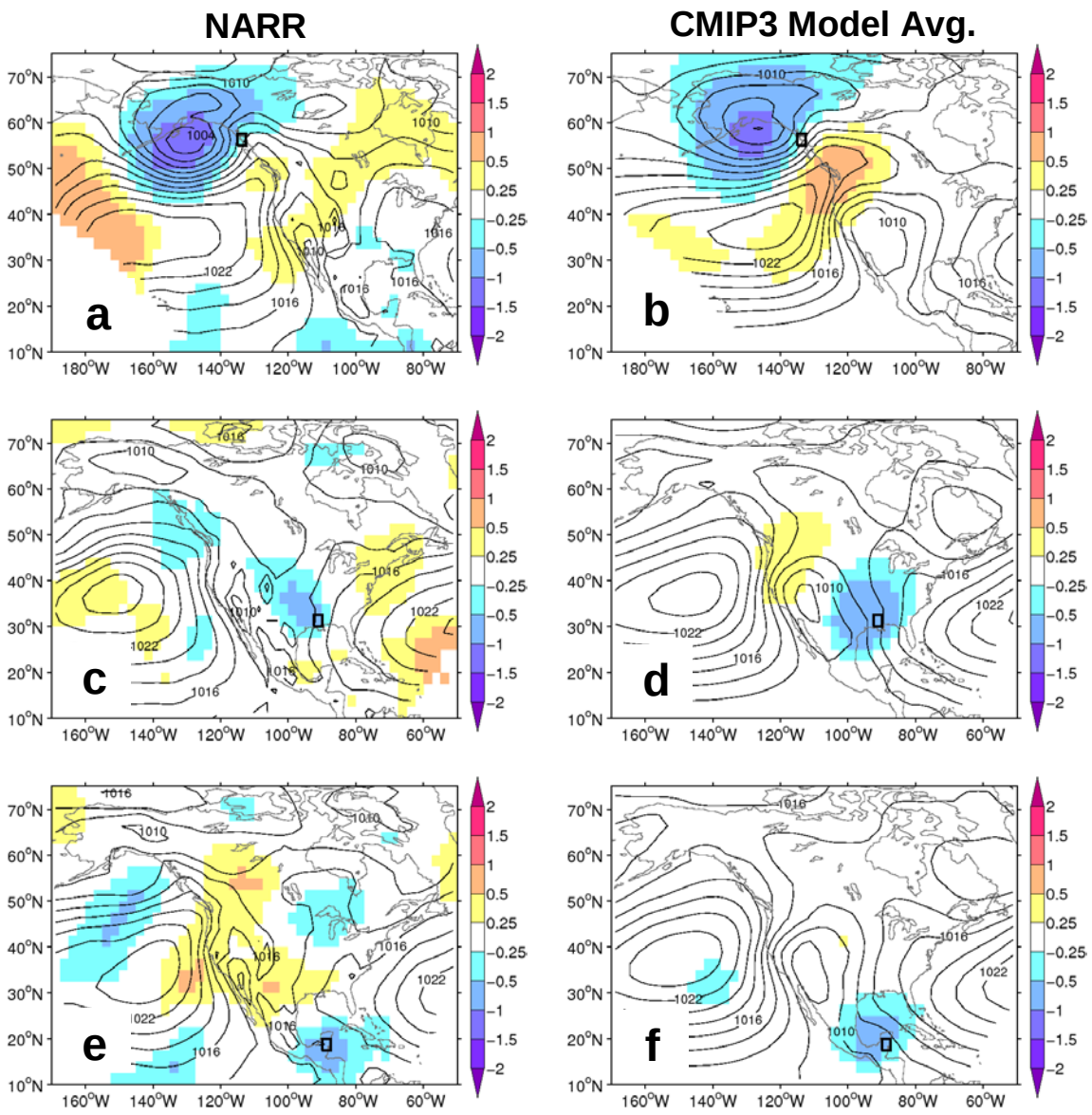

Figure. 8. As in Fig. 7 but for extreme summer (JJA) precipitation events.

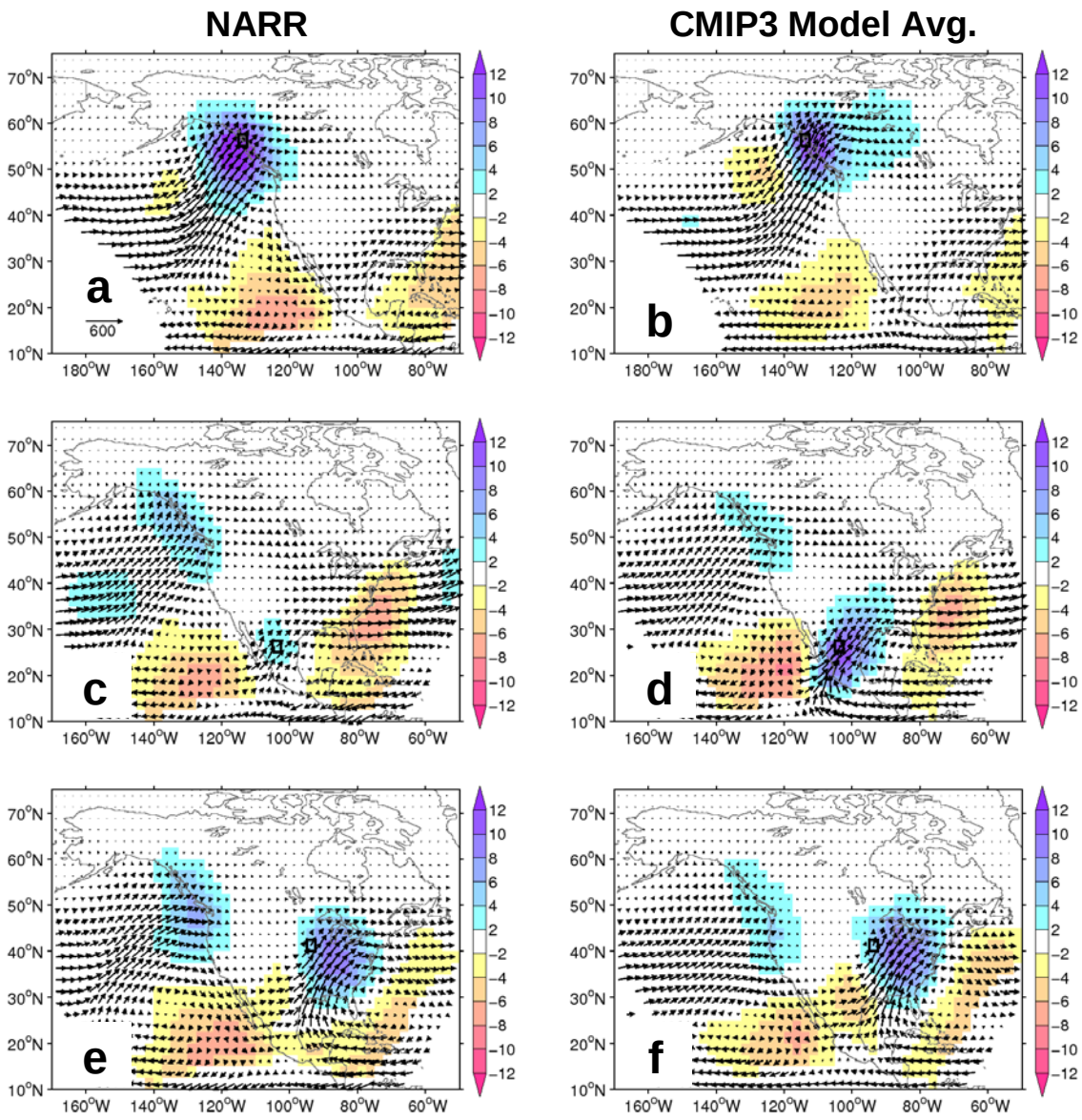

Figure. 9. Composites of vertically integrated water vapor flux (VIWVF, kg m^{-1} s^{-1}, vectors) and the convergence of vertically integrated water vapor flux (C(VIWVF), mm day^{-1}, color fills) for the 21 most extreme winter (DJF) precipitation events at selected grid cells (indicated by black rectangles). The C(VIWVF) was smoothed with a five-point box smoother before plotting. (left) Composites based on NARR and (right) those averaged over all CMIP3 models.

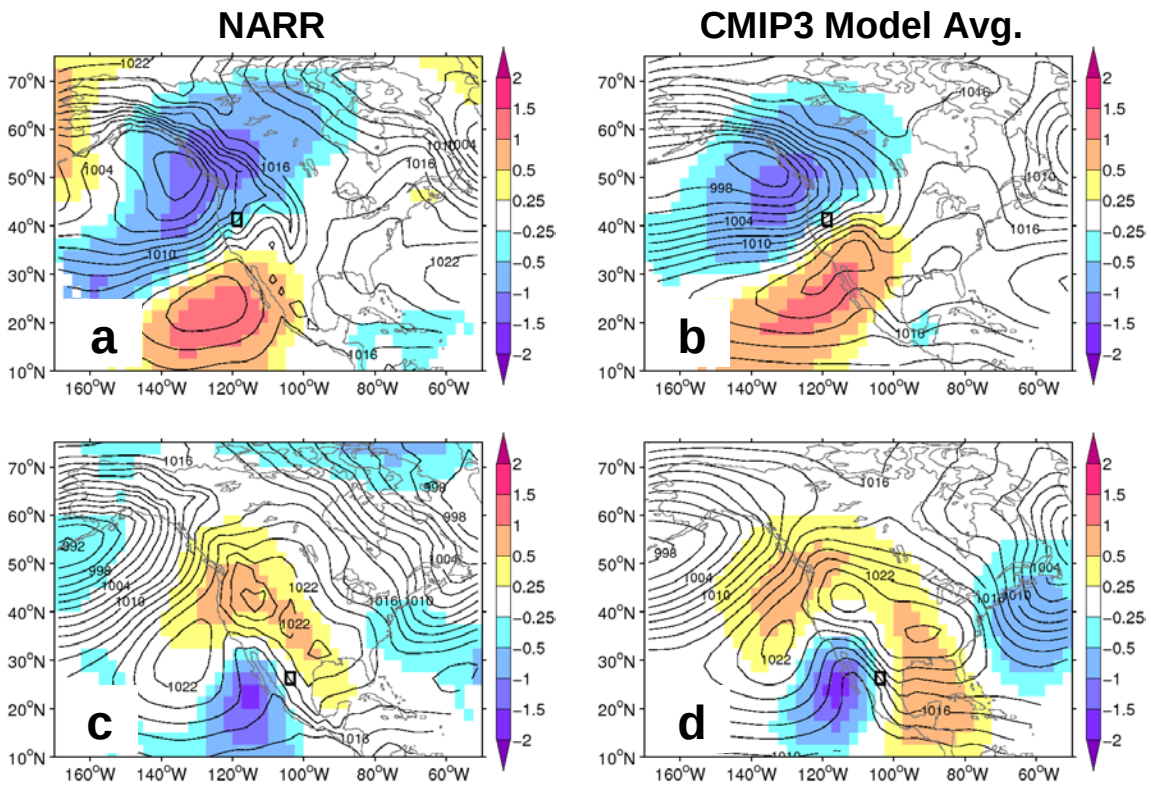

Figure. 10. As in Fig. 7, but for selected grid cells over which models overestimate winter P99M precipitation.

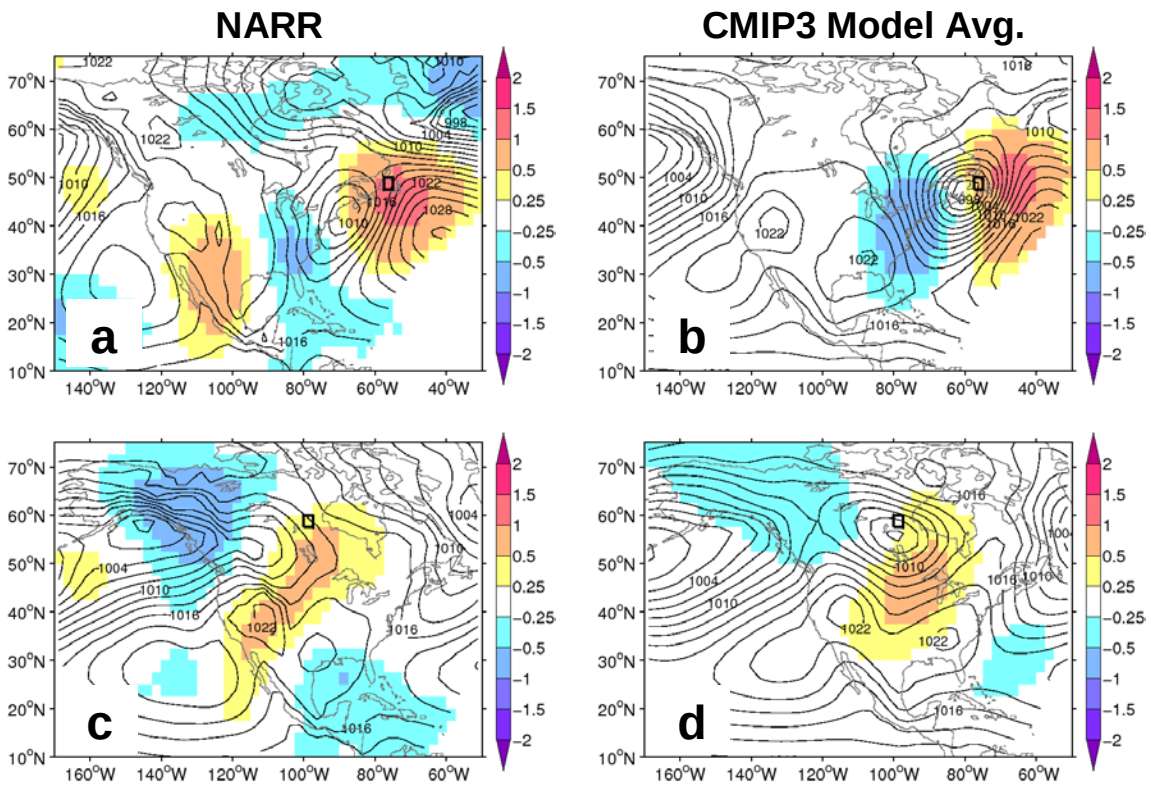

Figure. 11. As in Fig. 7, but for selected grid cells over which models produce realistic winter P99M precipitation.

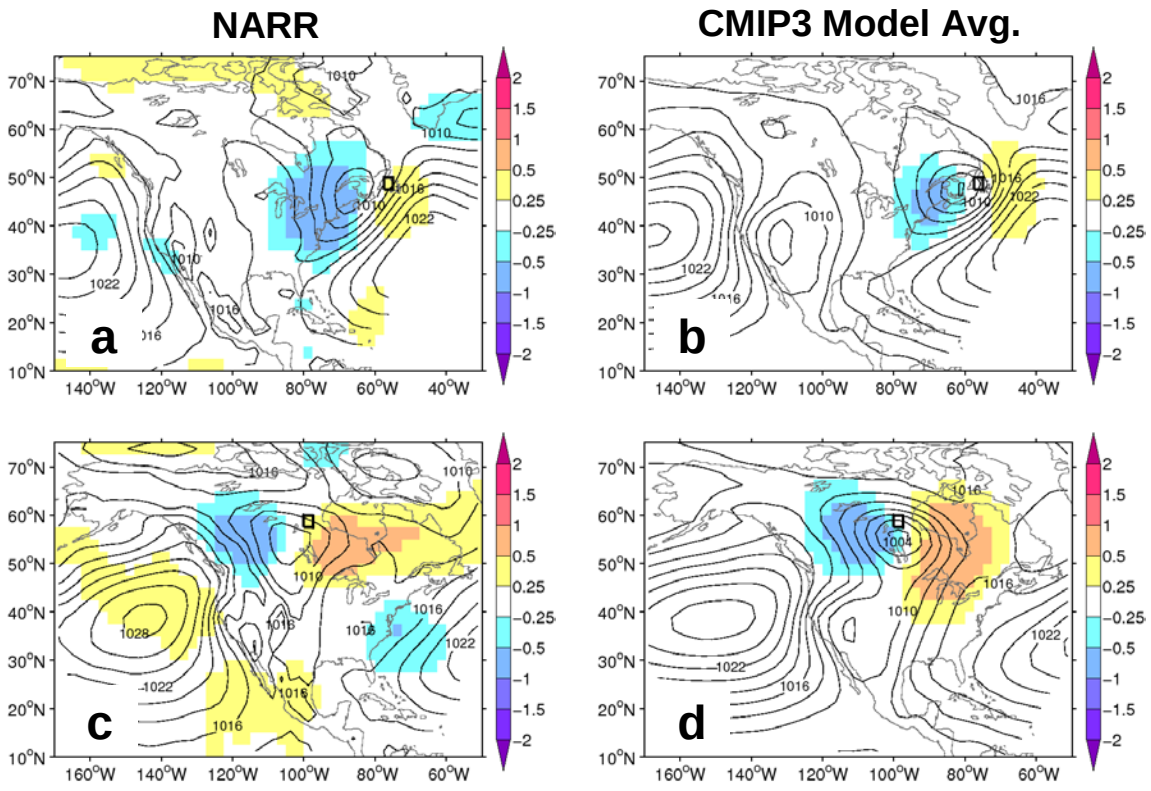

Figure. 12. As in Fig. 11, but for extreme summer (JJA) precipitation events.

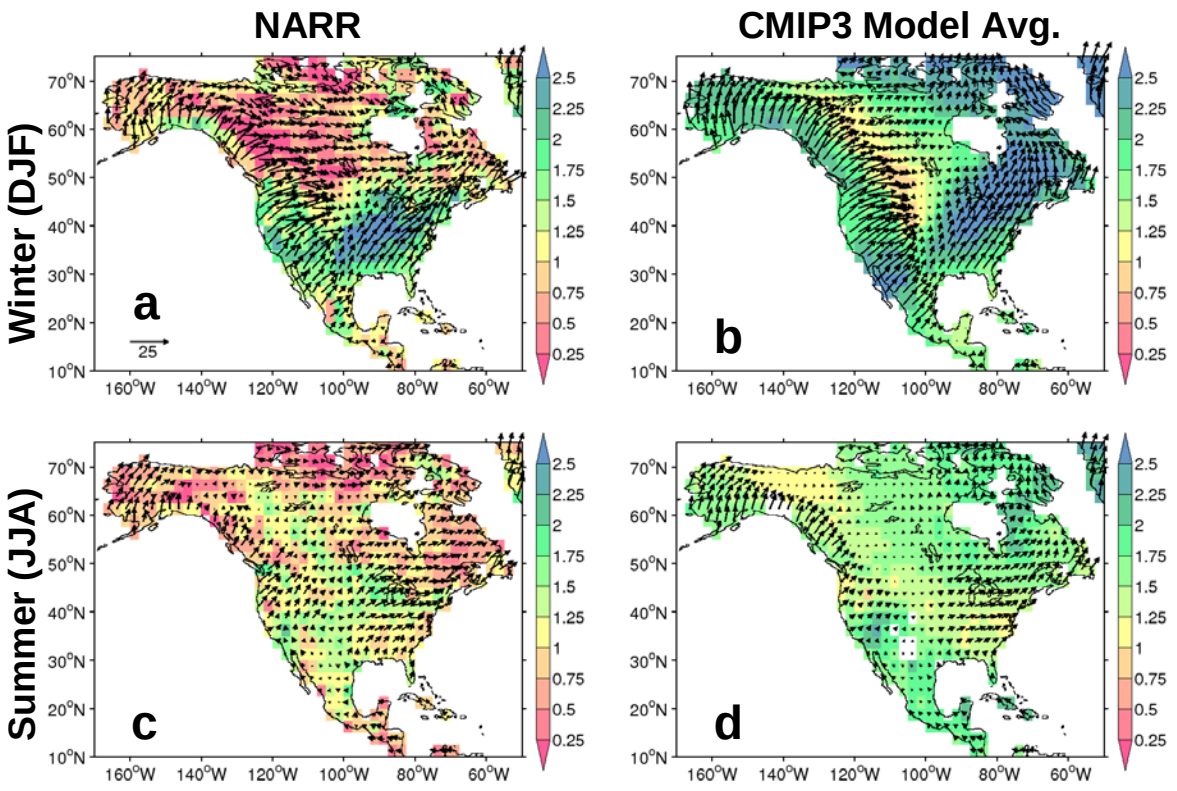

Figure. 13. The average local low-level (10-m to 500-mb average) winds (m/s, vectors) and vertically integrated water vapor standardized anomalies (VIWV*, dimensionless, color fills) during the 21 most extreme winter (top) and summer (bottom) precipitation events at every grid cell on the domain. (left) NARR and (right) CMIP3 model average. Missing grid cells in (d) are the result of missing specific humidity values for some days in the CSIRO-Mk3.0 model output.

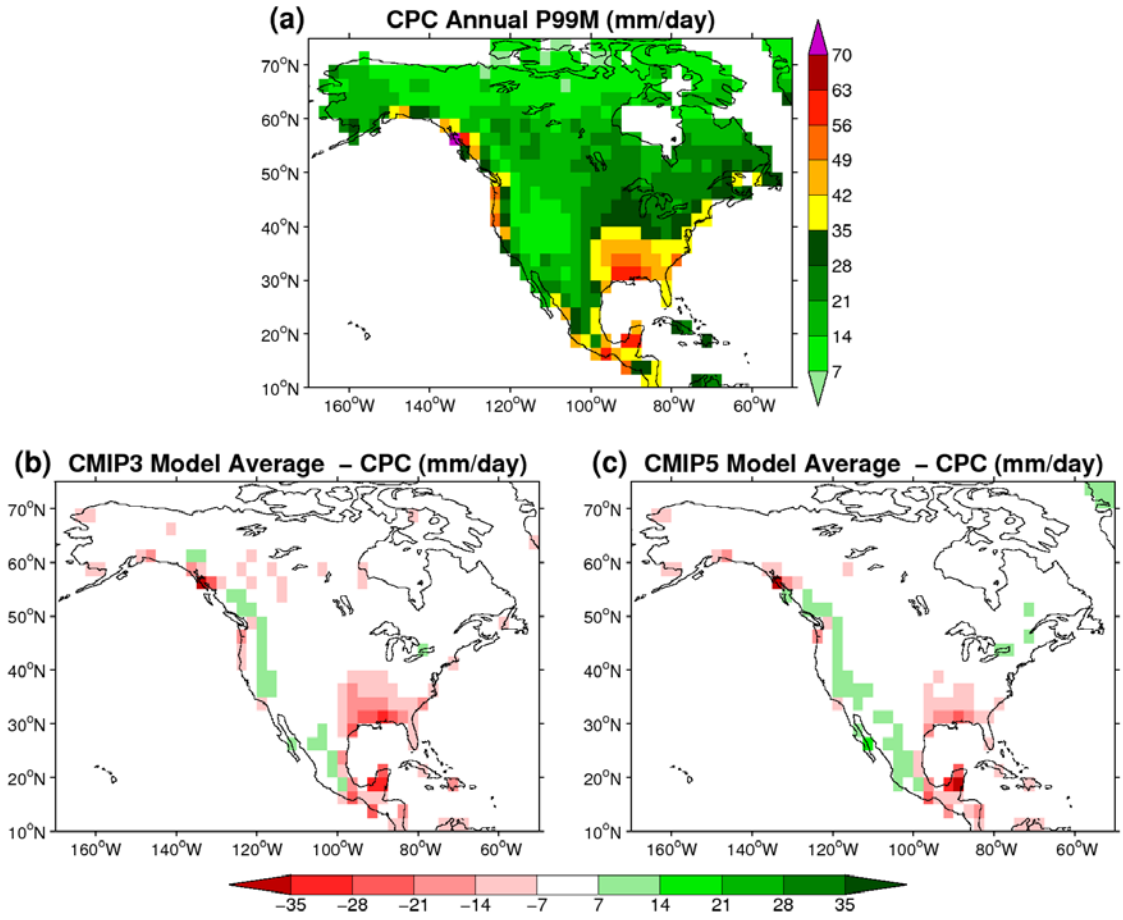

Figure 14. A comparison of annual P99M (1979-99) between (a) the CPC observations, (b) the CMIP3 multimodel average, and (c) the CMIP5 multimodel average. In (b) and (c), the difference between the corresponding multimodel average and CPC observations is shown in mm day^{-1}.

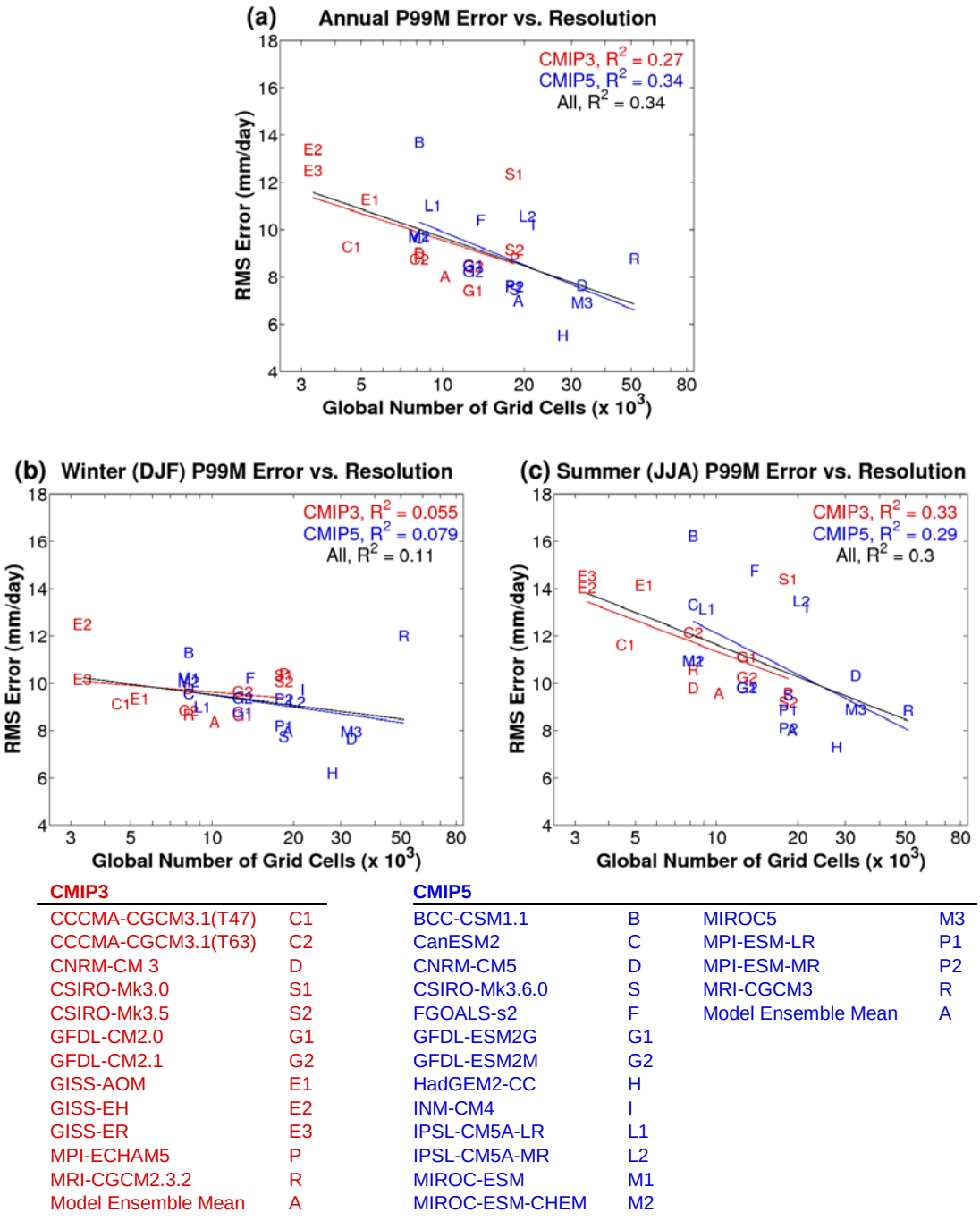

CMIP3	
CCCMA-CGCM3.1(T47)	C1
CCCMA-CGCM3.1(T63)	C2
CNRM-CM 3	D
CSIRO-Mk3.0	S1
CSIRO-Mk3.5	S2
GFDL-CM2.0	G1
GFDL-CM2.1	G2
GISS-AOM	E1
GISS-EH	E2
GISS-ER	E3
MPI-ECHAM5	P
MRI-CGCM2.3.2	R
Model Ensemble Mean	A

CMIP5			
BCC-CSM1.1	B	MIROC5	M3
CanESM2	C	MPI-ESM-LR	P1
CNRM-CM5	D	MPI-ESM-MR	P2
CSIRO-Mk3.6.0	S	MRI-CGCM3	R
FGOALS-s2	F	Model Ensemble Mean	A
GFDL-ESM2G	G1		
GFDL-ESM2M	G2		
HadGEM2-CC	H		
INM-CM4	I		
IPSL-CM5A-LR	L1		
IPSL-CM5A-MR	L2		
MIROC-ESM	M1		
MIROC-ESM-CHEM	M2		

Figure 15. Scatterplots of the root-mean-square (RMS) error in P99M over North America (mm day^{-1}) versus horizontal resolution of CMIP models for (a) annual, (b) winter, and (c) summer (see section 2.5 for details). The abscissa is plotted on a logarithmic (base 10) scale due to the wide range in spatial resolution between the

models. Letters identify the individual models, as listed in the tables below the graphs, where red letters correspond to CMIP3 and blue letters correspond to CMIP5. For the multimodel average, the RMS error was computed after first computing the multimodel average biases at every grid cell. A least squares linear fit to the RMS error versus $\log_{10}(resolution)$ values for each model ensemble and for both ensembles together is plotted, along with the corresponding correlation coefficients (R^2).

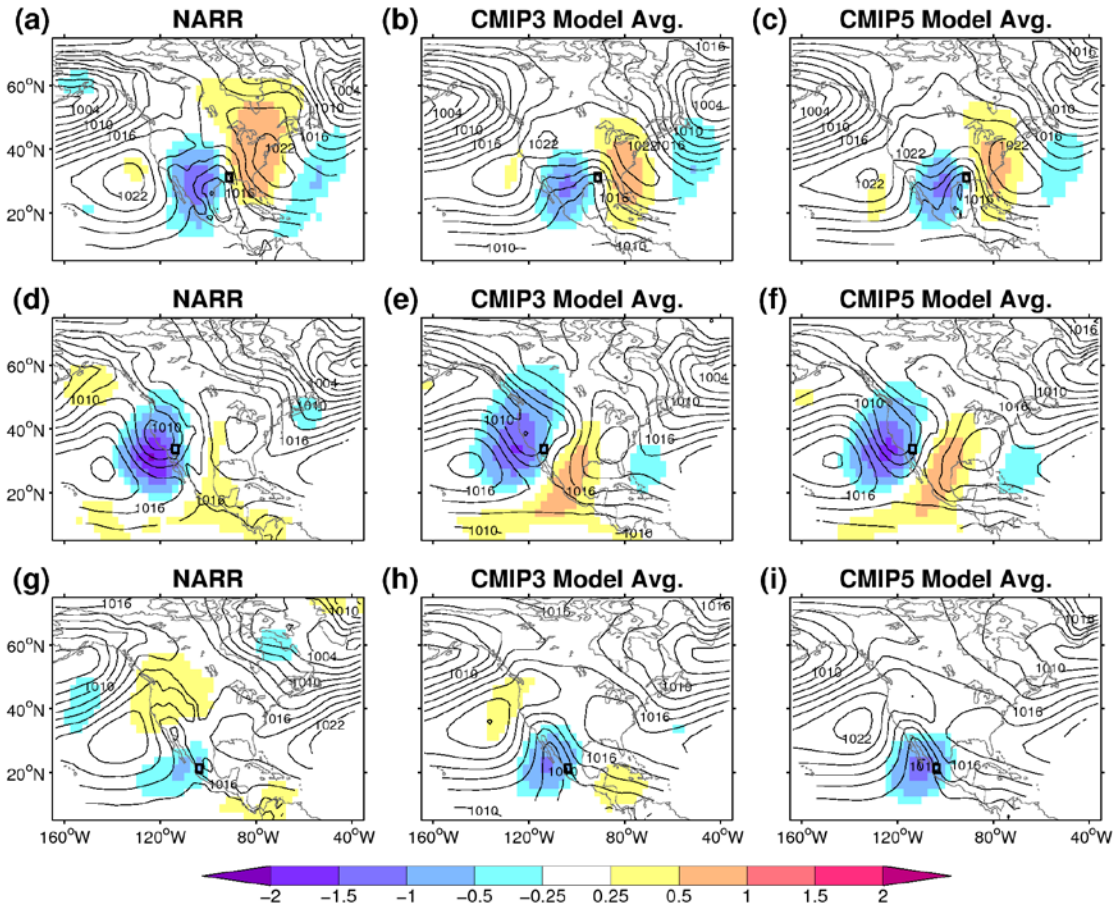

Figure 16. Composites of pressure at mean sea level (PMSL, hPa, contours) and 500 mb geopotential height standardized anomalies (Z500*, dimensionless, color fills) for the heaviest 1% of daily annual precipitation events at selected grid cells (indicated by black rectangles, which vary from top to bottom). Sea level pressure is contoured every 2 hPa. Composites are shown for (left) NARR, (middle) the CMIP3 model average, and (right) the CMIP5 model average.

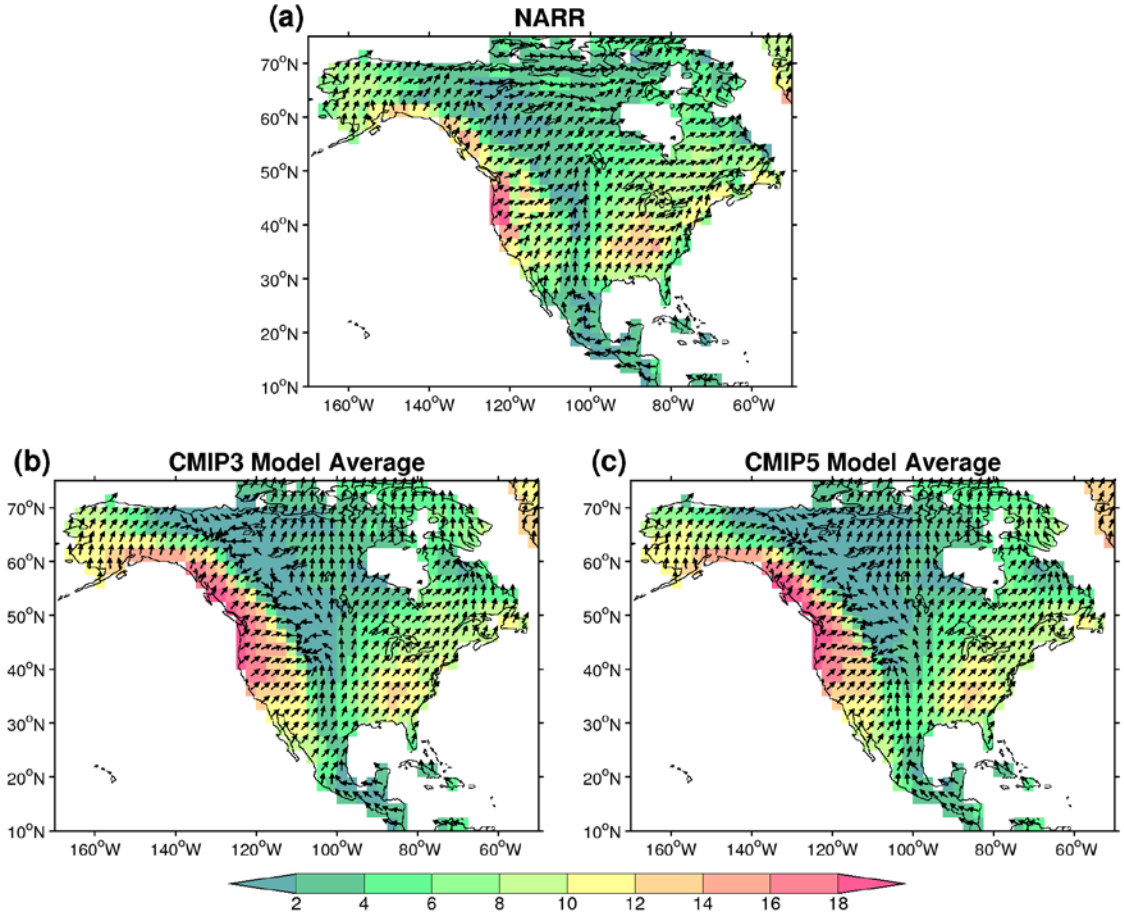

Figure 17. The local low-level (10-m to 500-mb mean) winds averaged over days when precipitation equals or exceeds the annual 99th percentile at every grid cell on the domain for (a) NARR, (b) the CMIP3 model average, and (c) the CMIP5 model average. Vectors (normalized to 1) show wind direction while color fills indicate wind speed in m s^{-1}.

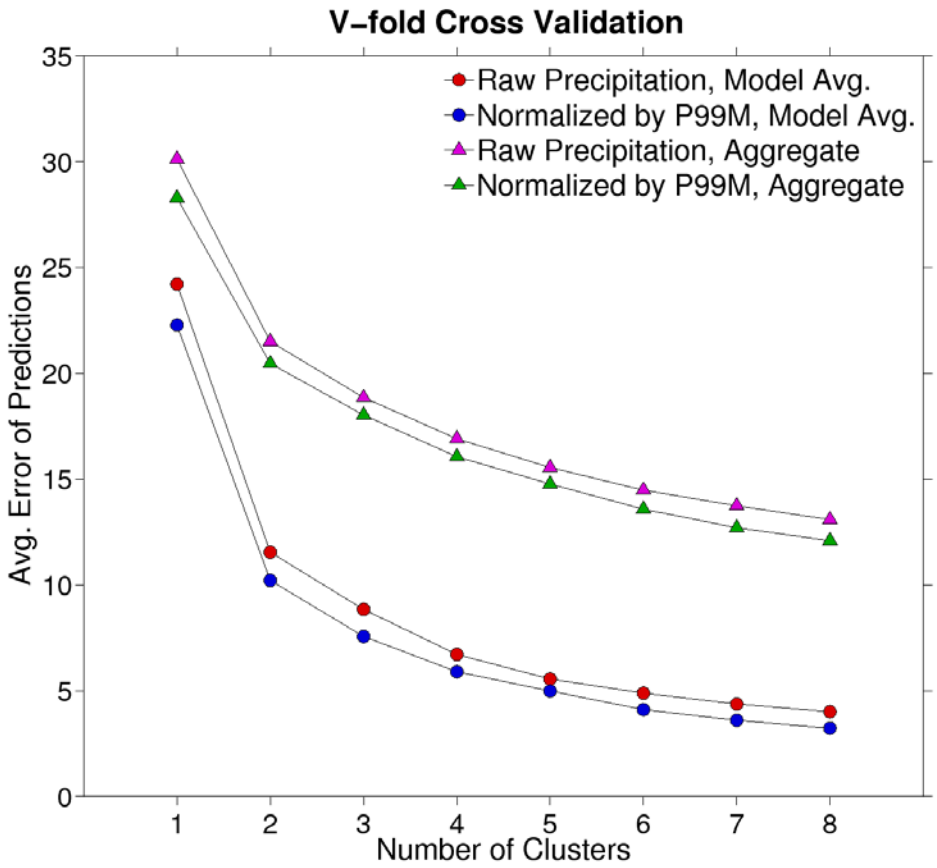

Figure 18. The average error in predictions of cluster assignments for a sample of left-out grid cells versus number of clusters, based on applying V-fold cross validation to precipitation change histograms using 5 subsamples (see section 3.2.c for details). The analysis was applied to histograms of count differences (RCP8.5-historical) in bins of raw precipitation or precipitation normalized by historical P99M for either the CMIP5 model average separately or the aggregate of all models (including the model average), following the legend. In all cases, the log of the count differences in the histograms was taken before applying the V-fold cross validation analysis. Values on the ordinate axis represent the sum of squared differences between the predicted centroid and grid cell histogram bin counts, averaged over all grid cells and subsamples left out in the cross validation process (in units of squared $\log_{10}(count\ differences)$).

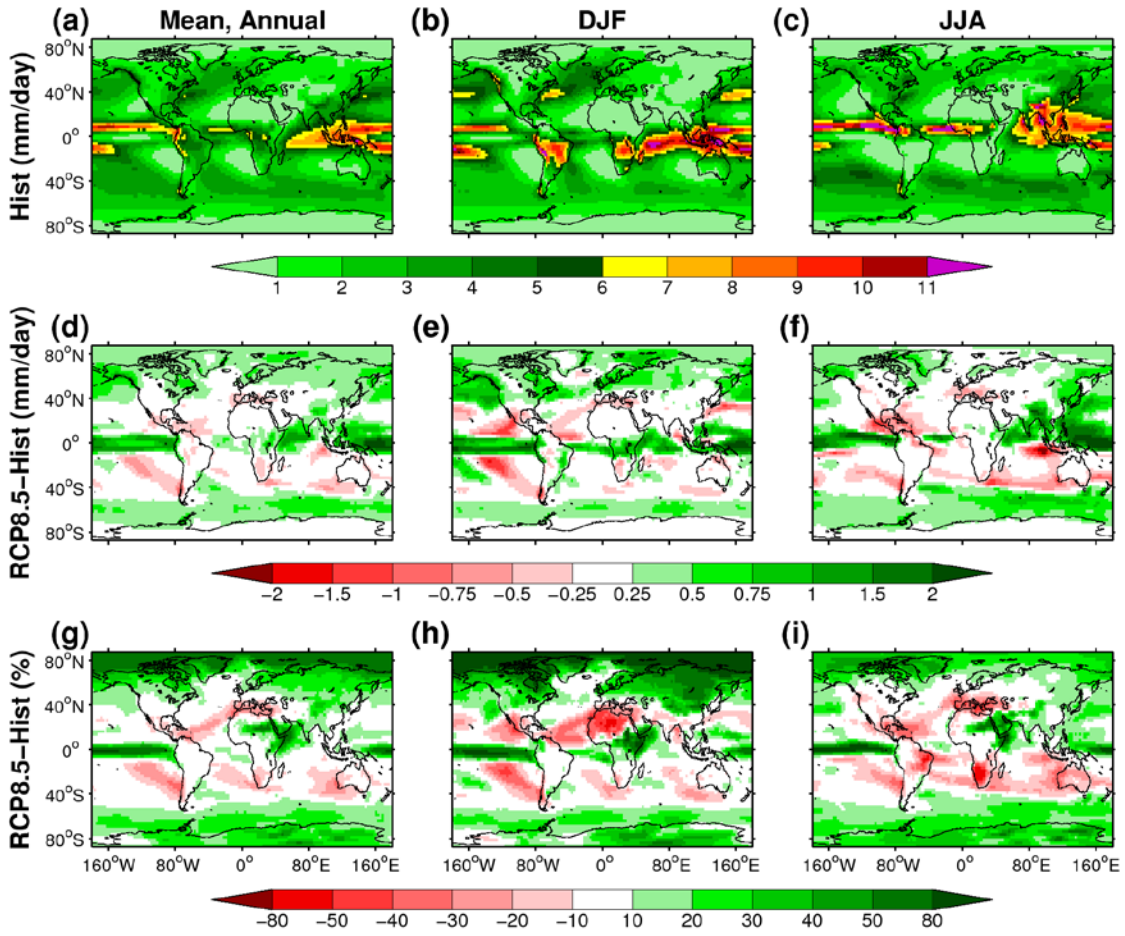

Figure 19. Mean precipitation for the multimodel average of CMIP5 models analyzed in this dissertation (see Table 2). The mean from the historical simulation over the period 1979-99 (mm day^{-1}) is shown in (a)-(c). The absolute difference between the RCP8.5 simulation period (2079-99) and historical period is shown in (d)-(f), while the percentage difference is shown in (h)-(i). Percentage differences were computed after first computing the model-mean historical and RCP8.5 values. The mean precipitation was computed over (left) annual, (middle) December-February (DJF), and (right) June-August (JJA) days.

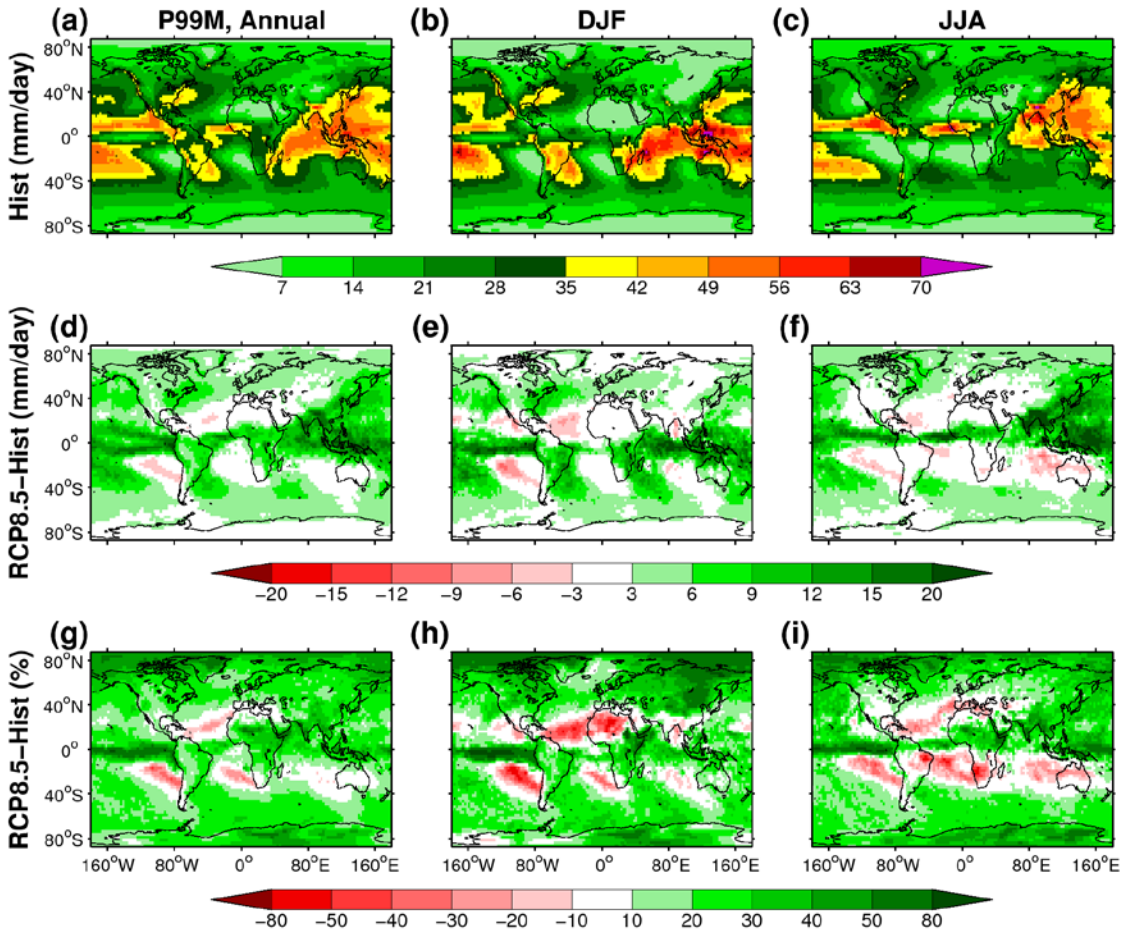

Figure 20. As in Fig. 19, but for the mean precipitation falling from the heaviest 1% of daily events (P99M, as defined in section 2.3).

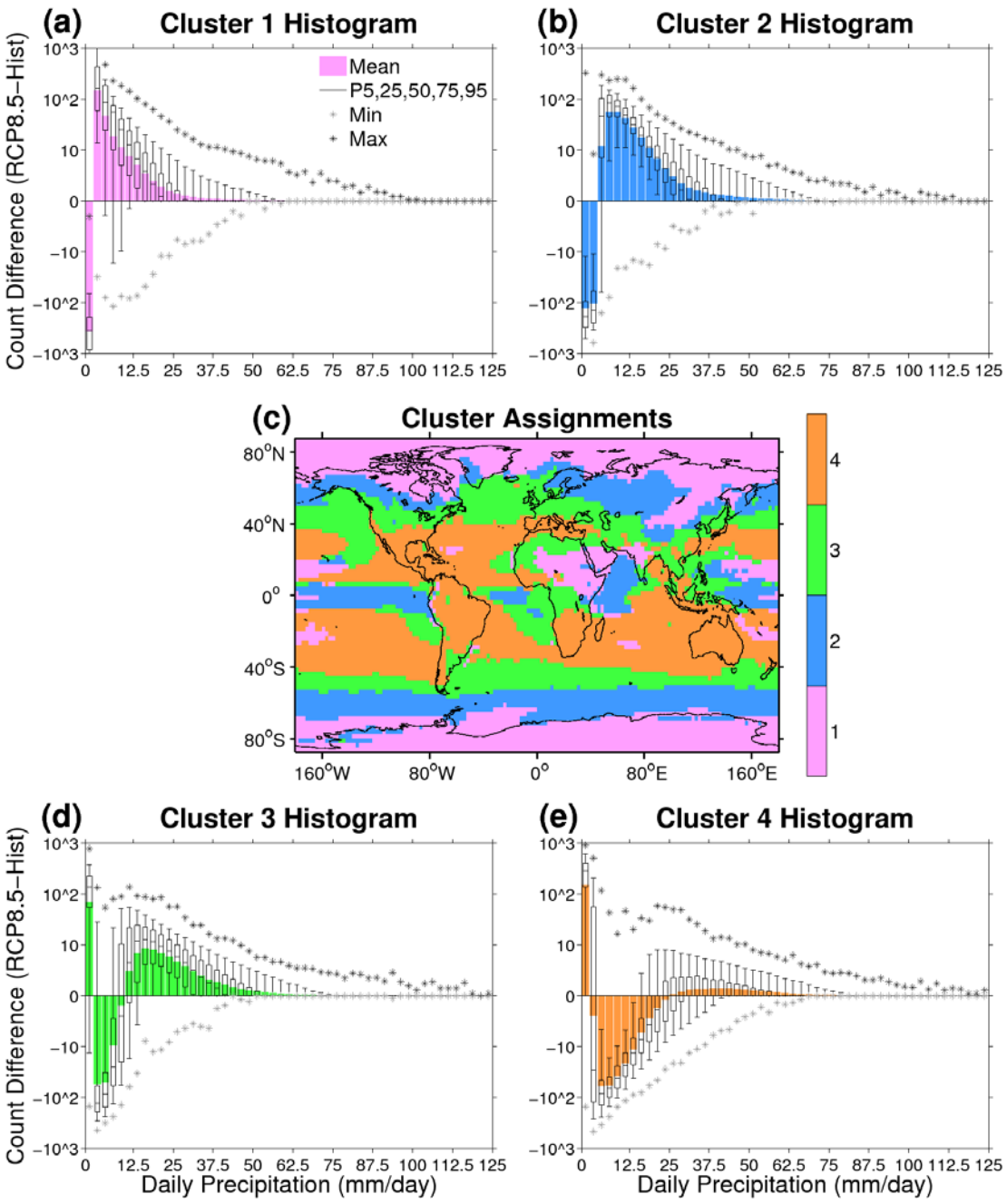

Figure 21. The (c) cluster assignments and (a) ,(b), (d), (e) centroid histograms for the application of k-means cluster analysis to difference histograms (RCP8.5-historical) of annual daily precipitation for the multimodel average (see section 3.2.b for details). The log of the count differences between the RCP8.5 and historical histograms was taken before applying cluster analysis. The histogram bars show the mean count differences

over all grid cells assigned each cluster, the box-and-whiskers show the inter-quartile range (25^{th}, 50^{th}, 75^{th} percentile, IQR, box) and 5^{th} to 95^{th} percentile spread (whiskers) of count differences among individual grid cells assigned each cluster, and the stars indicate the minimum and maximum count differences of all grid cells assigned each cluster. Note that some of these statistics are off the scale of the ordinate axis and not plotted. Precipitation bin edges are 0, 0.5, 2.5, 5.0, 7.5…125 mm day^{-1}.

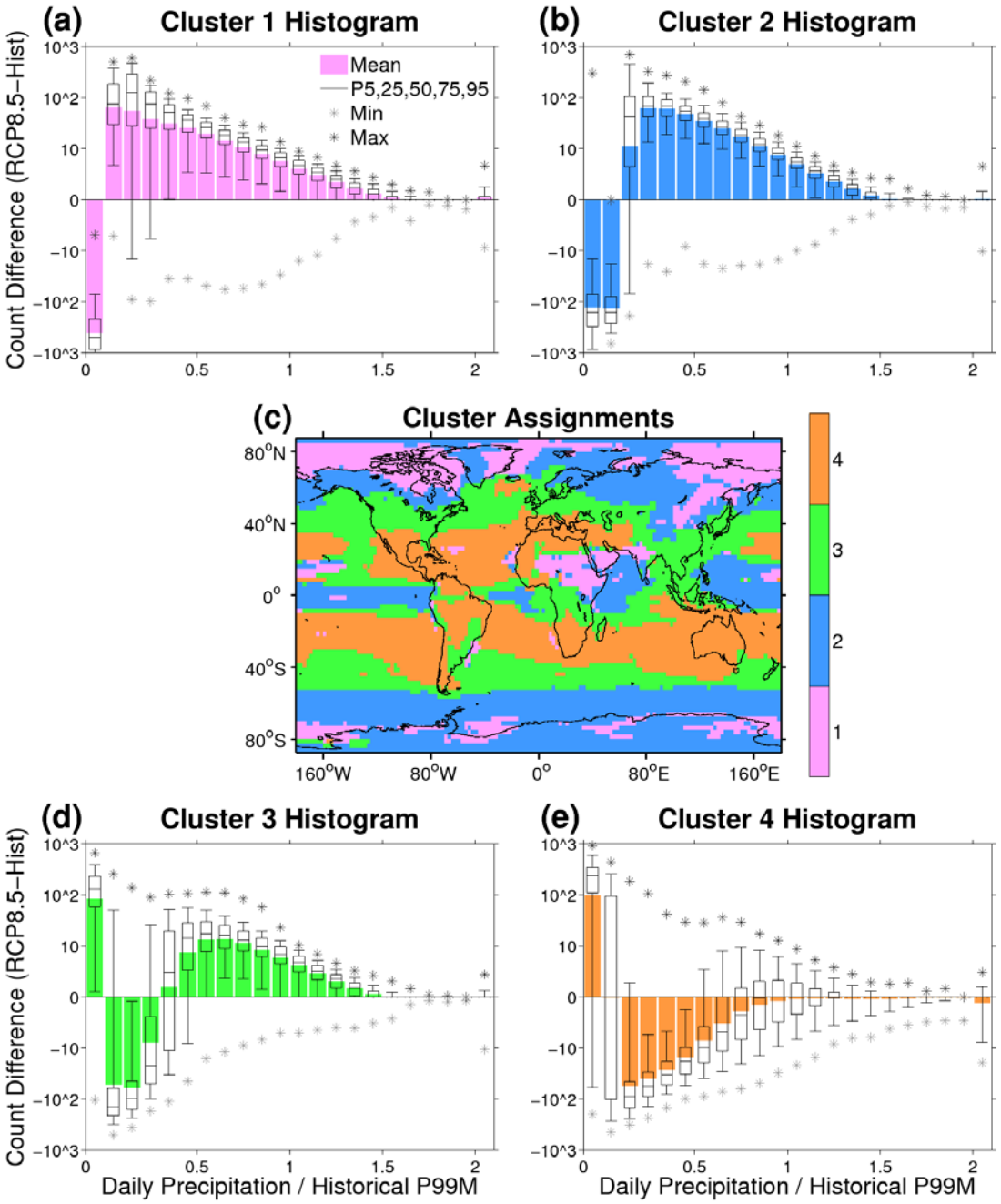

Figure 22. As in Fig. 21, but using precipitation normalized by the local historical P99M when generating histograms. The bin edges are 0, 0.01, 0.1, 0.2, 0.3…2, infinity.

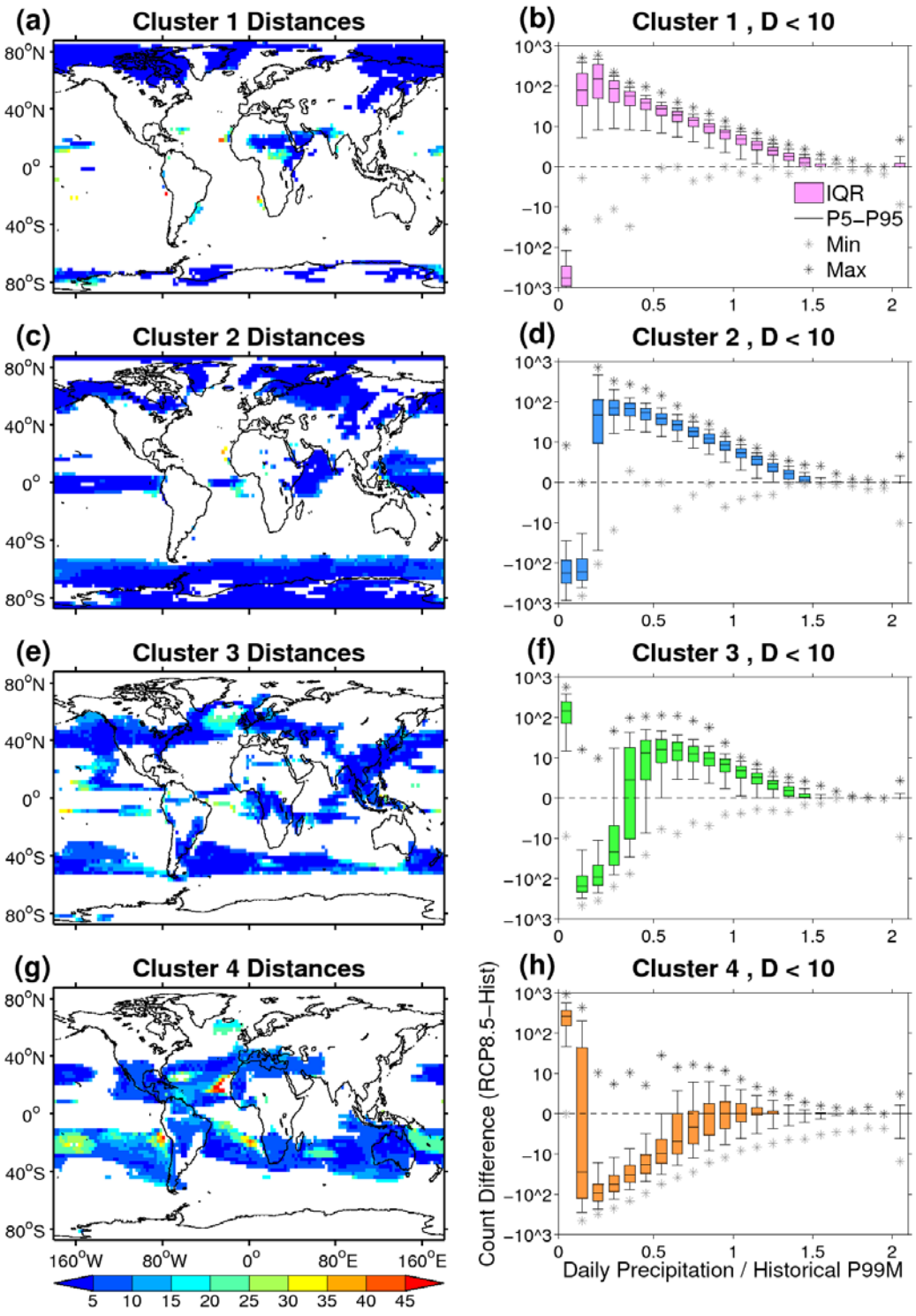

Figure 23. (left) The squared Euclidean distance (D, squared $\log_{10}(count\ differences)$) between the histogram at each individual grid cell and its corresponding assigned centroid histogram from Fig. 22 (i.e., using precipitation

normalized by historical P99M). (right) The variability (IQR, 5th to 95th percentile, min, max) of count differences among grid cells with a distance of less than 10 from their assigned cluster.

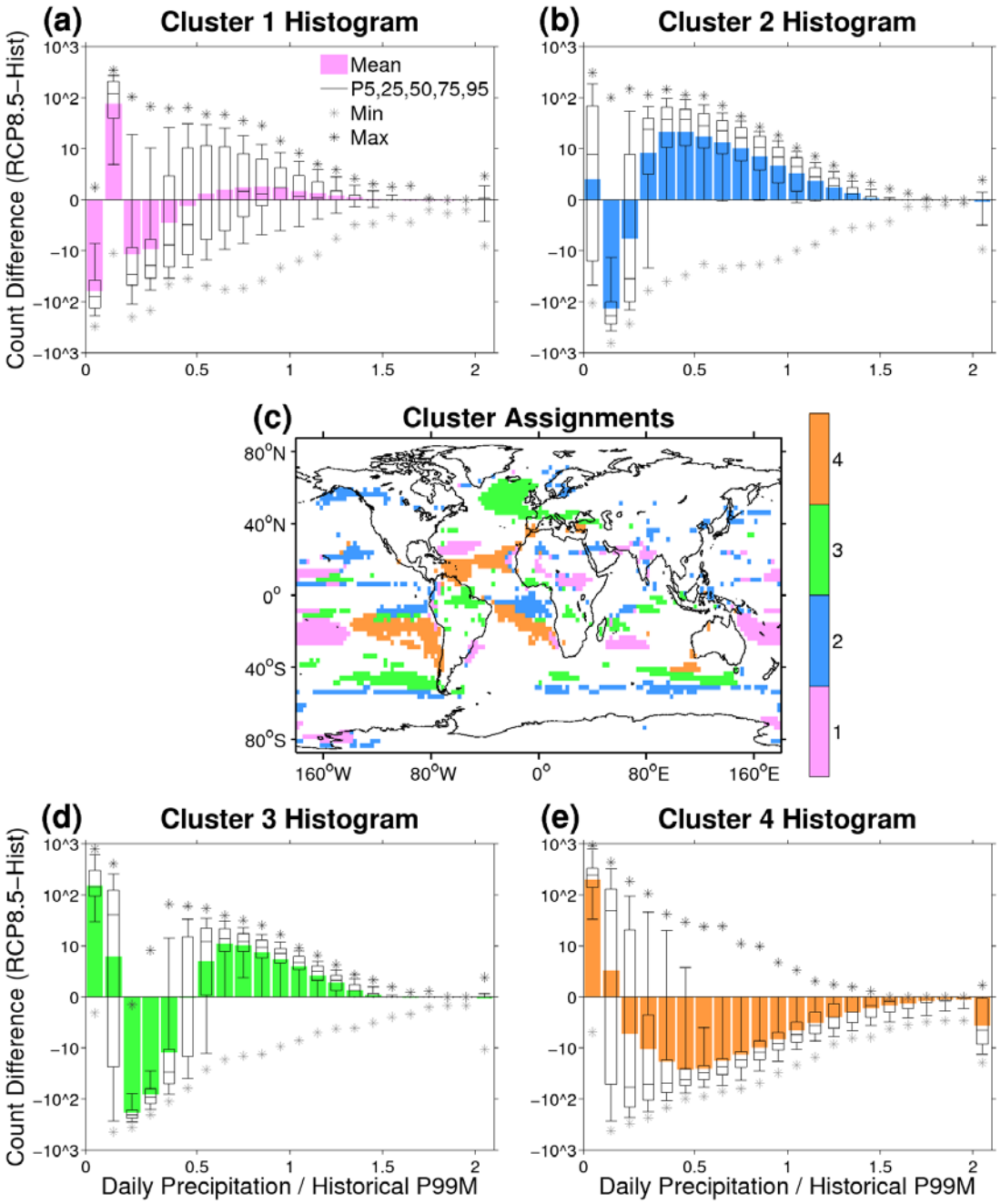

Figure 24. The results of applying cluster analysis to grid cells with a distance of 10 or more from their assigned cluster in Fig. 22 (i.e., using precipitation normalized by historical P99M). The quantities plotted are analogous to those in Fig. 22.

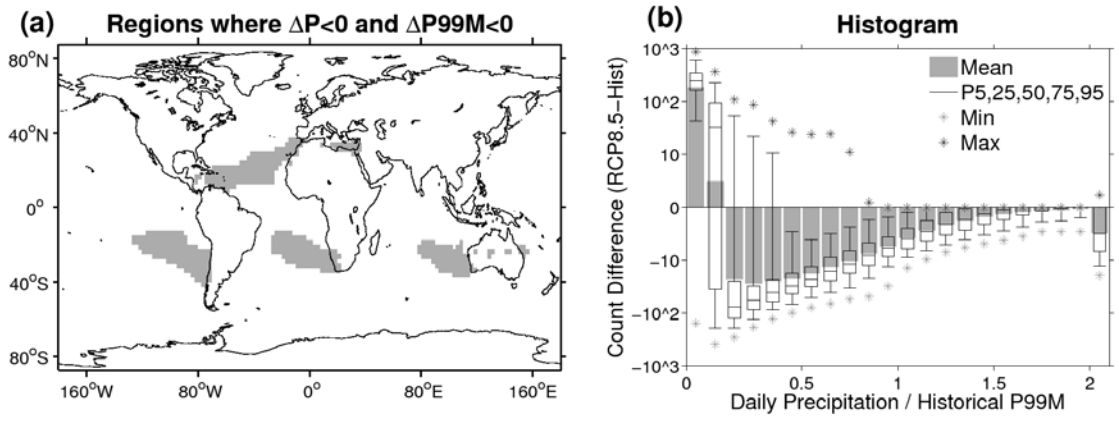

Figure 25. (a) Locations where annual mean precipitation (P) and heavy precipitation (P99M) are both projected to decrease in a warmer climate in the CMIP5 ensemble (gray shading). (b) The mean difference histogram (bars) and grid cell variability of count differences (box-and-whiskers, stars) computed over the regions shown in (a), using normalized precipitation. Both plots are based on the CMIP5 multimodel mean.

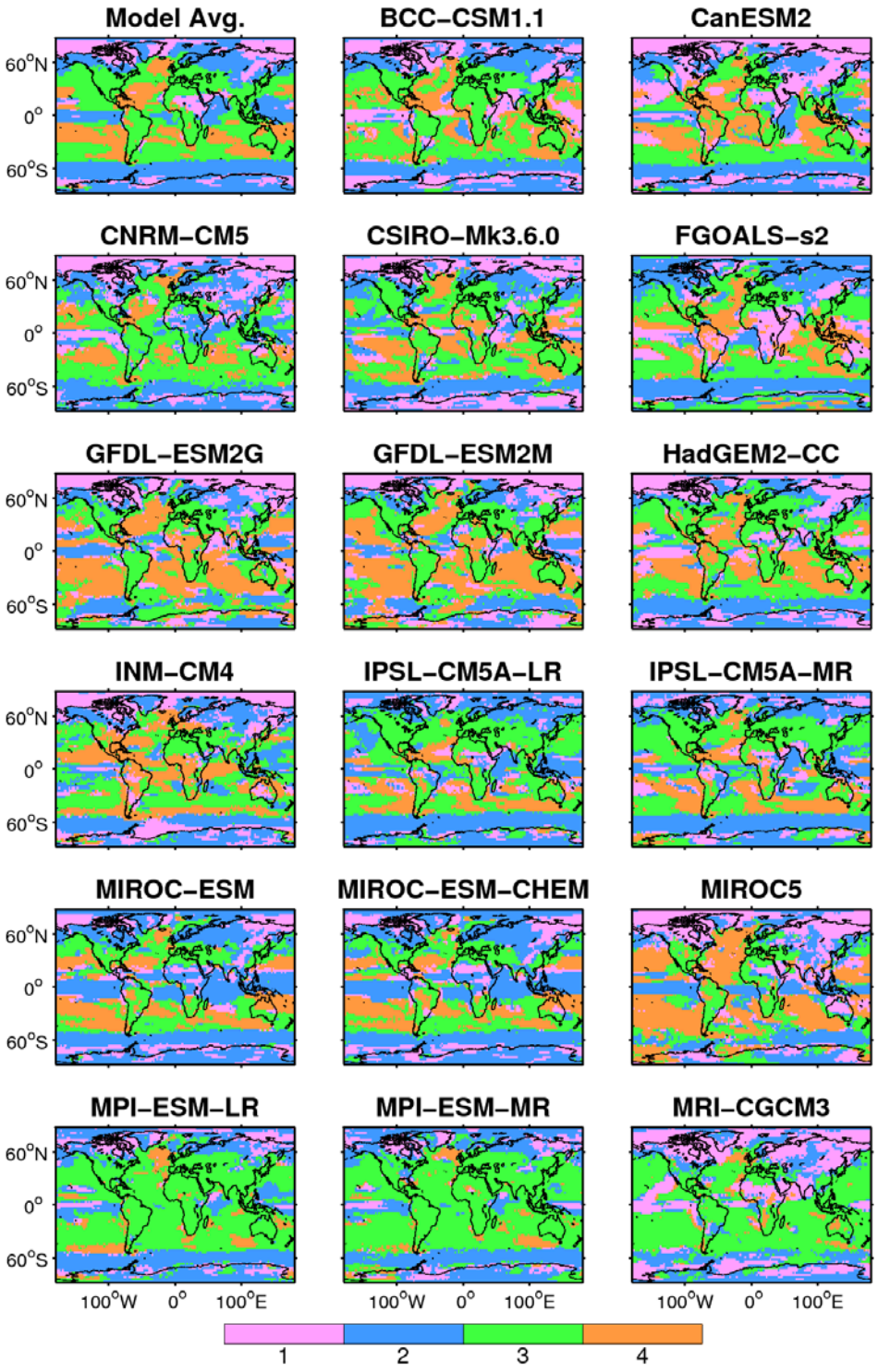

Figure 26. The cluster assignments when applying cluster analysis to the aggregate of all grid cells from every individual model and the model average (as described in section

3.2.b). Precipitation was binned after first normalizing by historical P99M before applying cluster analysis.

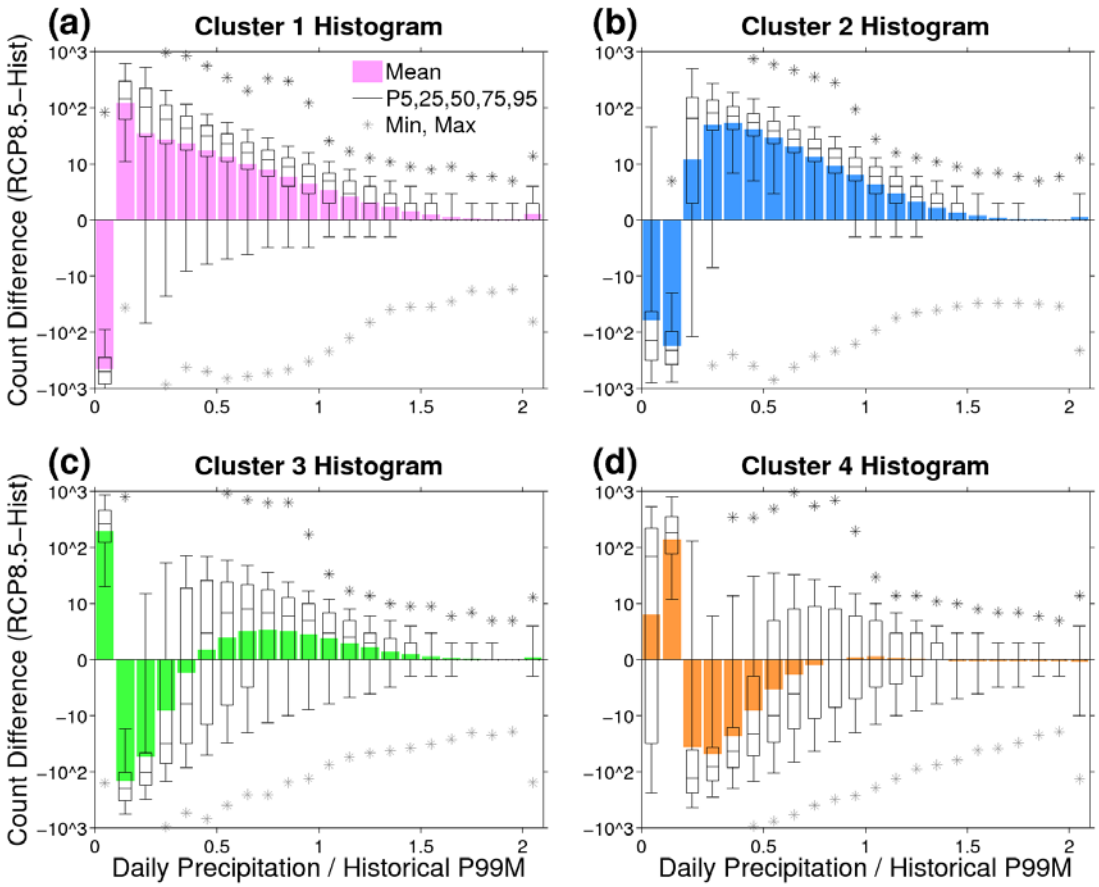

Figure 27. The cluster histograms corresponding to the assignments shown in Fig. 26. The statistics on the histograms were calculated from all grid cells from every model (including the multimodel average) and are analogous to those in Fig. 22.

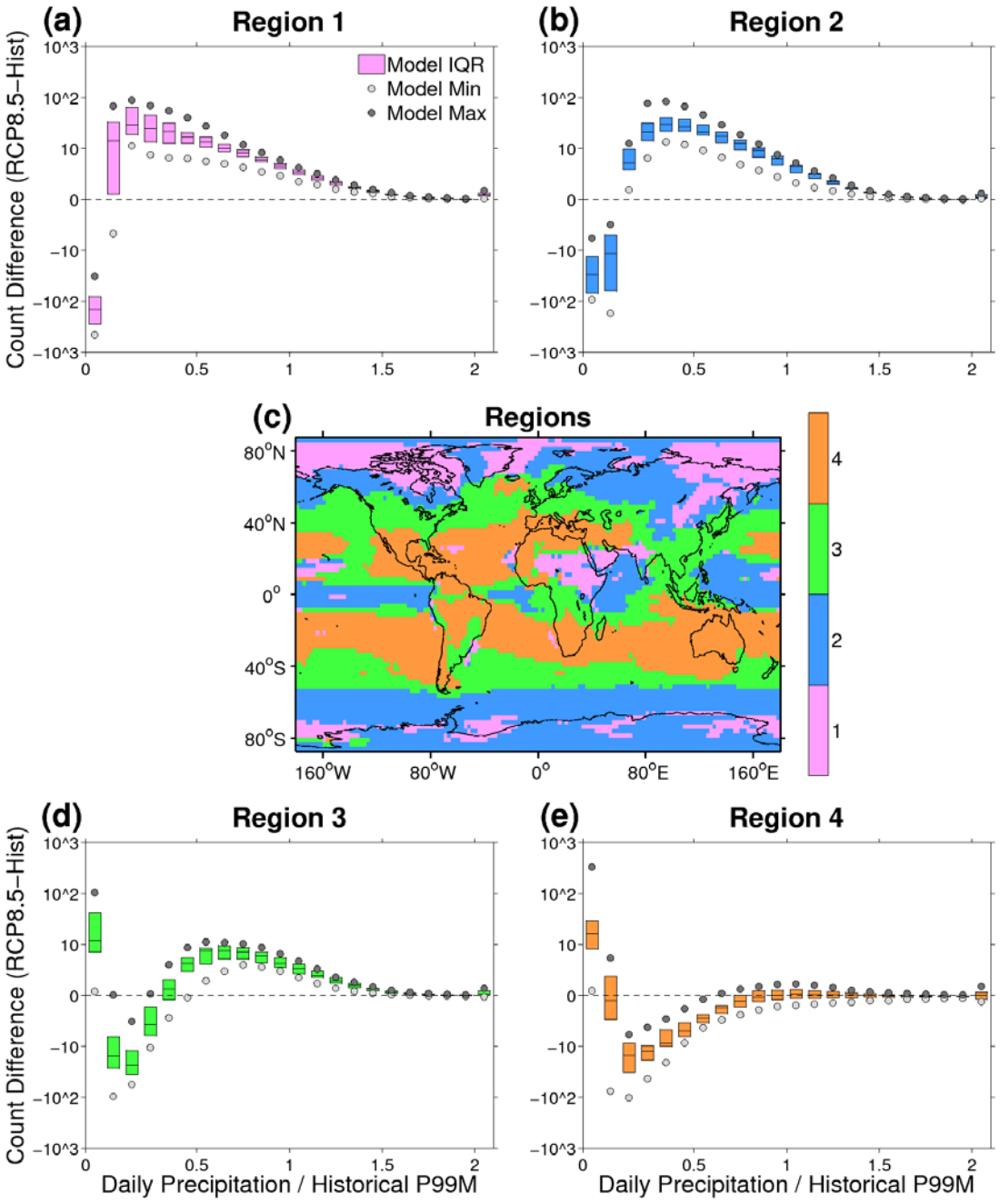

Figure 28. (c) Regions determined from the cluster assignments applied to the multimodel mean using precipitation normalized by historical P99M (identical to Fig. 22c). (a), (b), (d), (e) The linear mean of count differences (for the same bins in Fig. 22) over each region for each model, where the intermodel IQR, min, and max are shown.

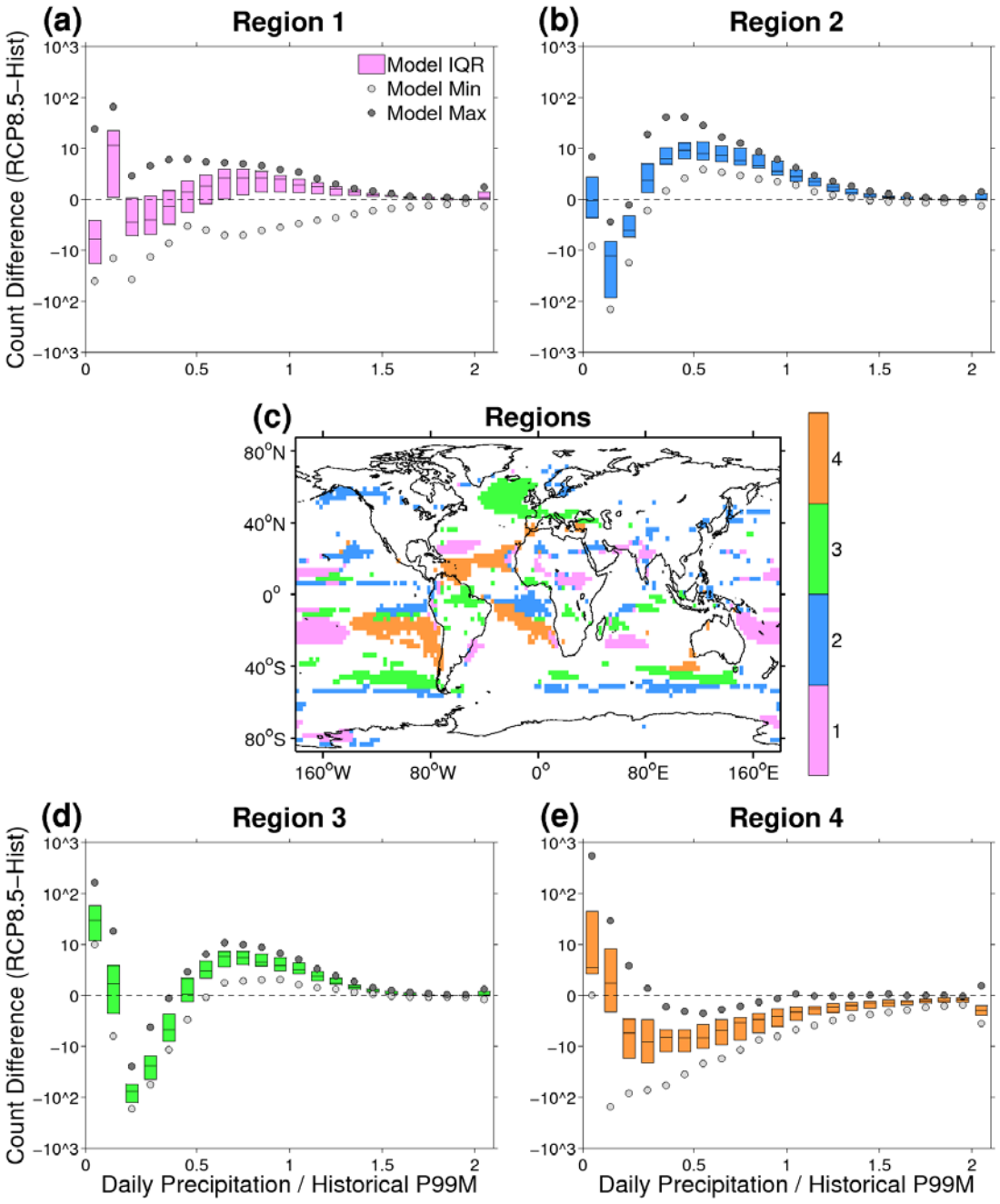

Figure 29. As in Fig. 28, but using the cluster assignments from the analysis in Fig. 24 to determine regions.

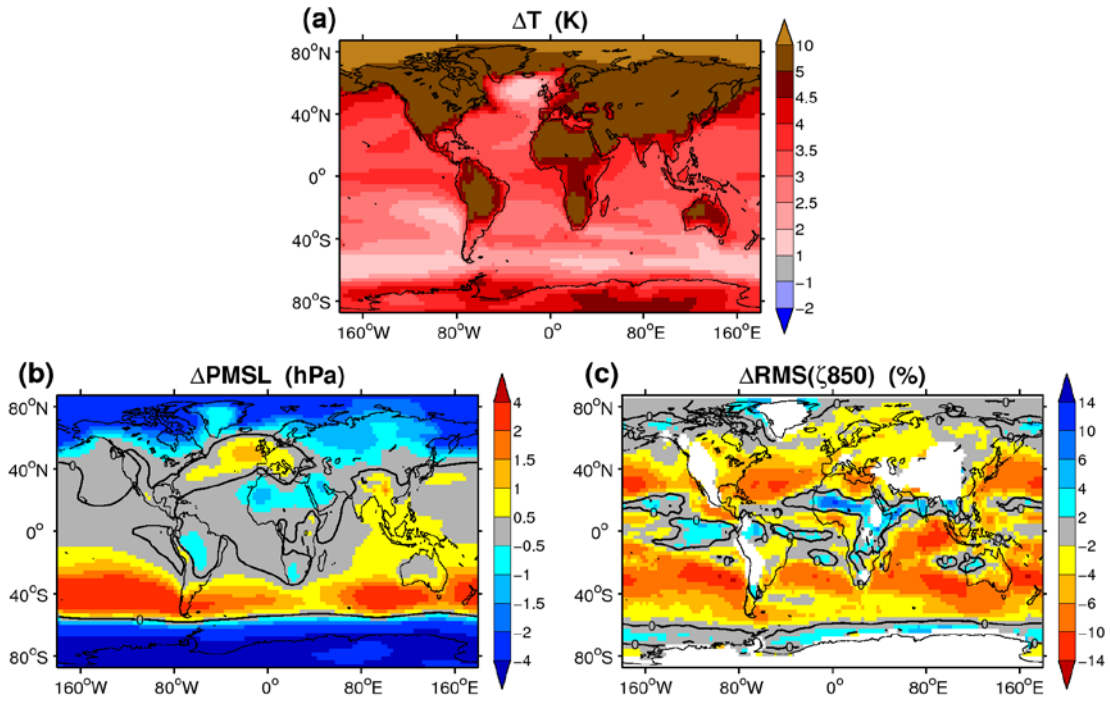

Figure 30. CMIP5 multimodel average difference (RCP8.5-historical) in (a) annual mean 2-m air temperature (ΔT, K), (b) annual mean sea level pressure (ΔPMSL, hPa), and (c) annual root-mean-square (RMS) of high pass filtered relative vorticity of the 850 mb wind (ΔRMS(ζ850), %). The zero contour is plotted as the thick black line in (b) and (c). Missing grid cells in (c) are due to topography at 850 mb.

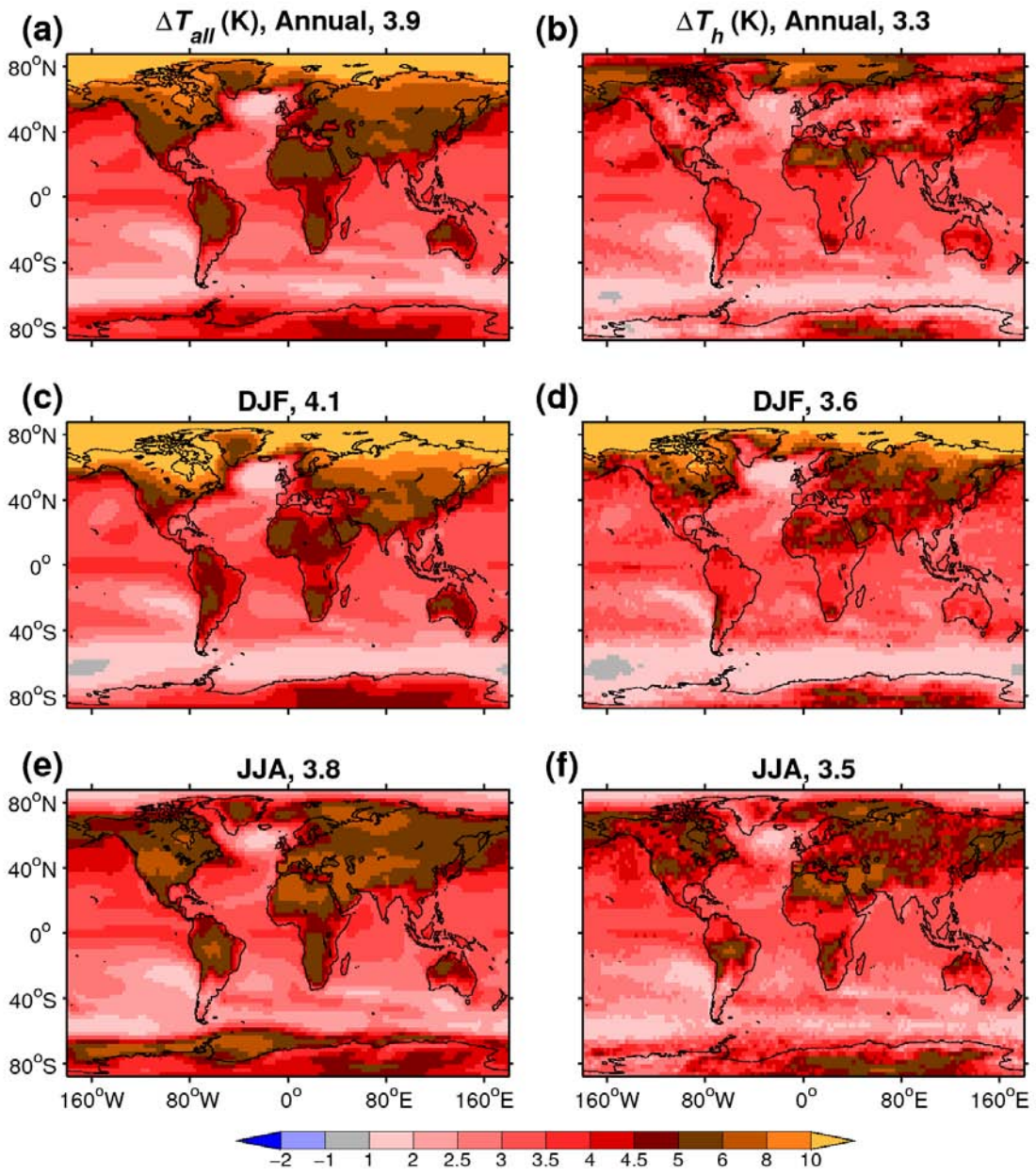

Figure 31. The CMIP5 multimodel average change in mean surface (2-m) air temperature from the historical (1979-99) to RCP8.5 (2079-99) period (K). The mean temperature is computed over (left) all days (ΔT_{all}), and (right) days when precipitation equals or exceeds the local 99th percentile (ΔT_h). The metrics are computed for (a)-(b) all seasons, (c)-(d) DJF only, or (e)-(f) JJA only. The corresponding area-weighted global-mean temperature change is given above each map.

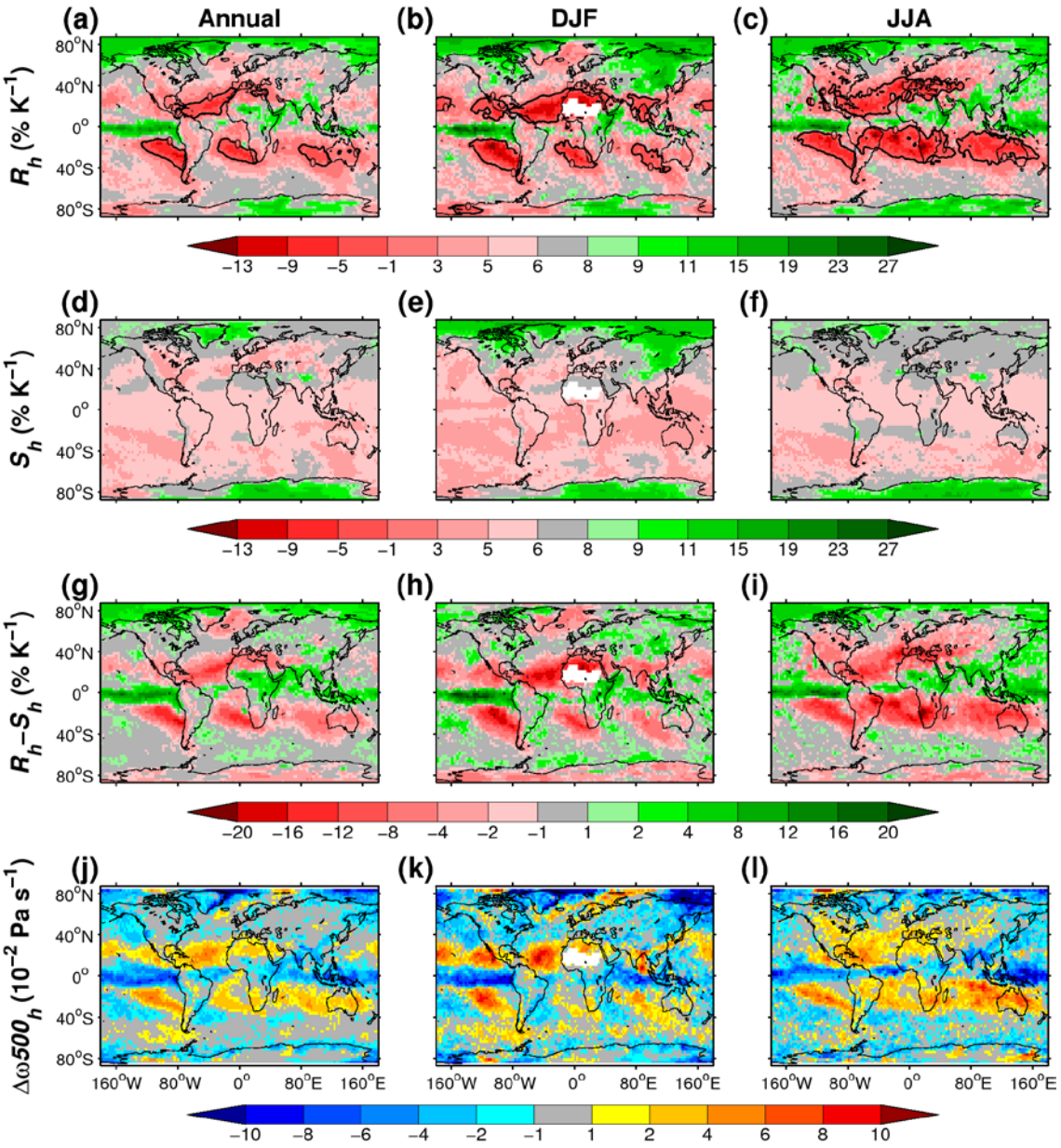

Figure 32. (a)-(c) The sensitivity of heavy precipitation to warming (R_h, % K^{-1}, see section 4.2.b for details, zero contour shown as a thick black line), (d)-(f) the thermodynamic sensitivity predicted by S_h (% K^{-1}, see section 4.2.b), (g)-(h) the difference between the actual and predicted sensitivity ($R_h - S_h$), and (j)-(l) the RCP8.5-historical difference in 500 mb pressure velocity averaged over heavy precipitation days (≥99th percentile) at each grid cell ($\Delta\omega 500_h$, Pa s^{-1}). Note that the color scale in (a)-(f) is

centered at 7% K^{-1} for comparison with Clausius-Clapeyron scaling. The metrics are computed for (left) annual, (middle) DJF, and (right) JJA days. The CMIP5 multimodel mean is shown in all panels (see section 4.3 for details). Missing values are those in which the 99^{th} percentile of daily precipitation is zero in at least one model for either the historical or RCP8.5 period.

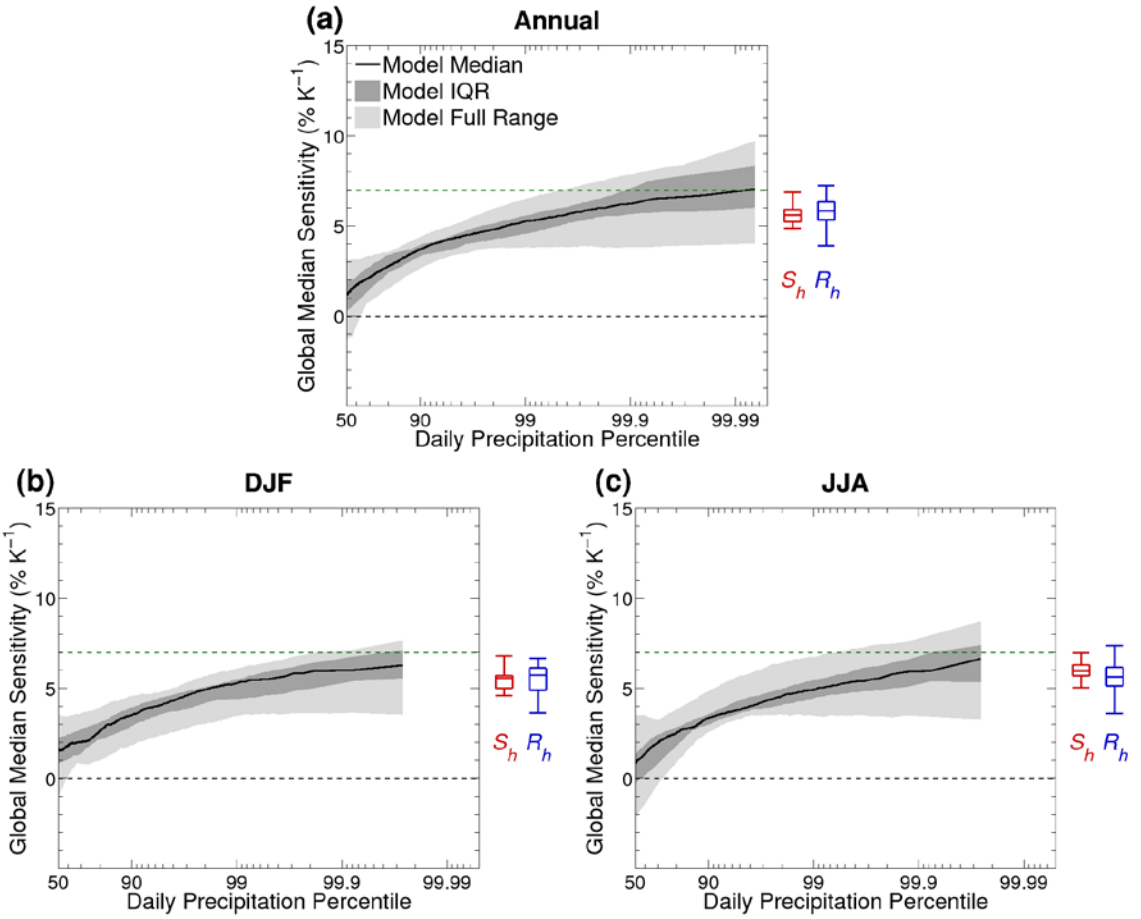

Figure 33. Global median sensitivity of precipitation at specific percentiles (% K^{-1}) computed from (a) annual, (b) DJF, and (c) JJA days (curves and shading, see section 4.3 for details). At each percentile, the model median (black line), interquartile range (IQR, 25th-75th percentile, dark shading) and full range (light shading) of the sensitivities are shown. For comparison, the intermodel variability (min, 25th percentile, median, 75th percentile, max) of the global median grid cell value of S_h and R_h (red and blue box-and-whiskers, respectively) are plotted to right of the respective plots, using the same y-axis. Note that S_h and R_h are computed using all percentiles ≥ 99th (as described in section 4.2.b). The black and green dashed lines indicate 0% K^{-1} and 7% K^{-1}, respectively.

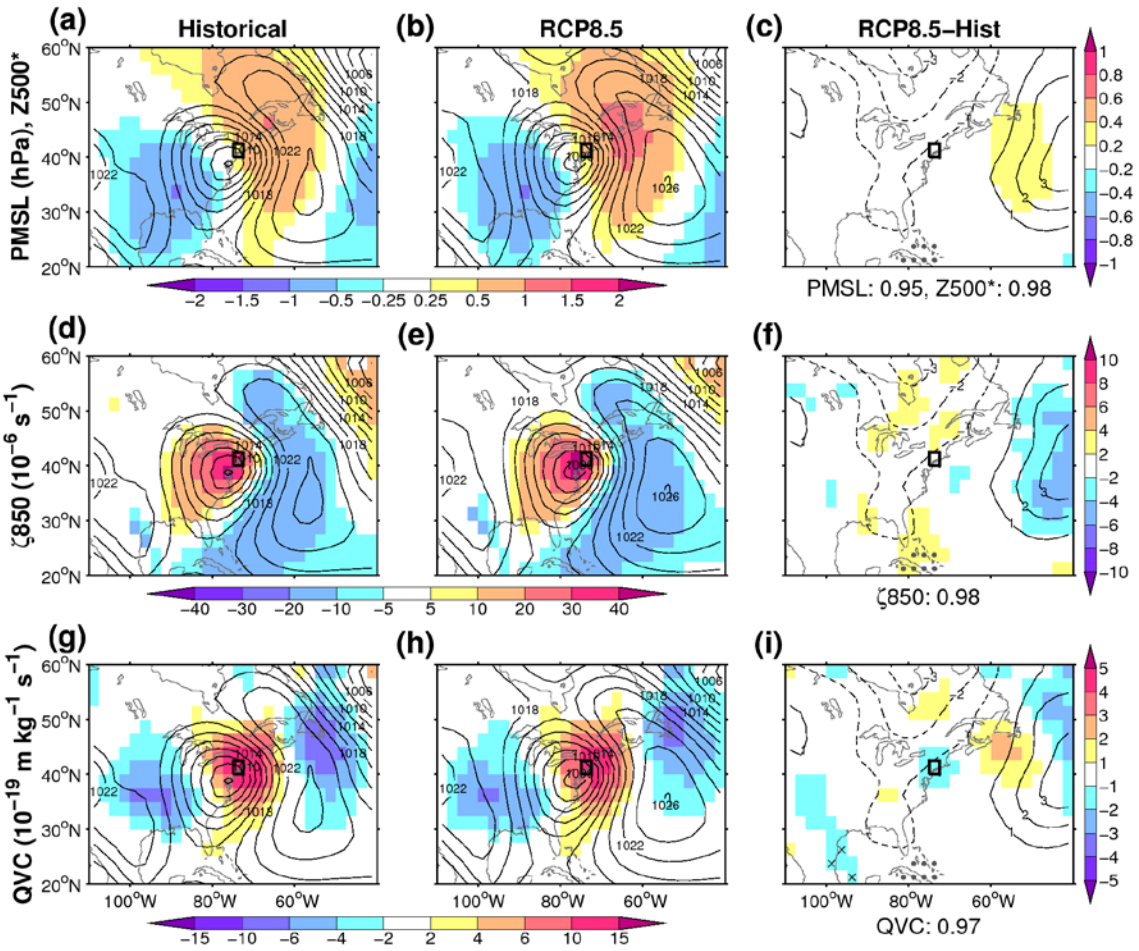

Figure 34. Winter (DJF) composite patterns of various quantities during heavy precipitation events at a grid cell in the northeastern United States (black box), for the CMIP5 ensemble mean. (left) Composite patterns for the historical period, (middle) RCP8.5 period, and (right) their difference. Pressure at mean sea level (PMSL, hPa, line contours) is shown in every panel, with a contour interval of 2 hPa in the historical and RCP8.5 plots and 1 hPa in the difference plots (negative changes are dashed, positive are solid). Color fills show (a)-(c) z-scores of geopotential height at 500 mb (Z500*), (d)-(f) wind voriticity at 850 mb (ζ850, 10^{-6} s^{-1}), and (g)-(i) **Q**-vector convergence (QVC, 10^{-19} m kg^{-1} s^{-1}); see section 4.2.c for further description of the plotted quantities. In the difference plots, grid cells where at least 12 of 17 individual models have the same sign

of change as the model mean and the change is statistically significant (see section 4.4.a) in at least 6 of those models, are identified with a dot for PMSL and cross for the respective color-filled quantities. Below each of the difference plots, the spatial correlation between the historical and RCP8.5 composites (computed over the plot domain) of the respective quantities is given.

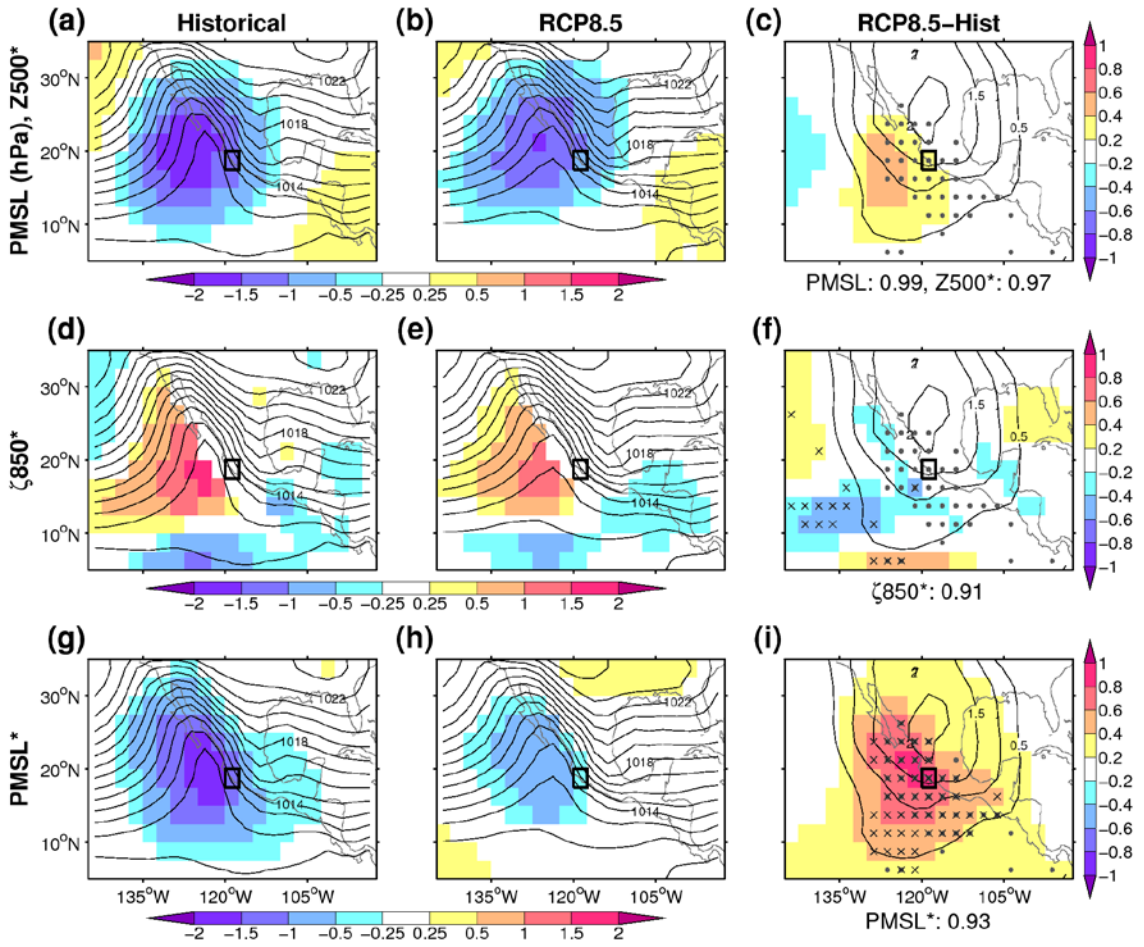

Figure 35. As in Fig. 34, but for a grid cell along the west coast of Mexico and showing different quantities as color fills in the bottom two rows; (d)-(f) the z-score of 850 mb wind vorticity (ζ850*), and (g)-(i) the z-score of pressure at mean sea level (PMSL*). Note that the contour interval for PMSL is 1 hPa in the historical and RCP8.5 plots, and 0.5 hPa in the difference plots. Also note that grid cells are missing over and near land in the plot of ζ850* due to topography.

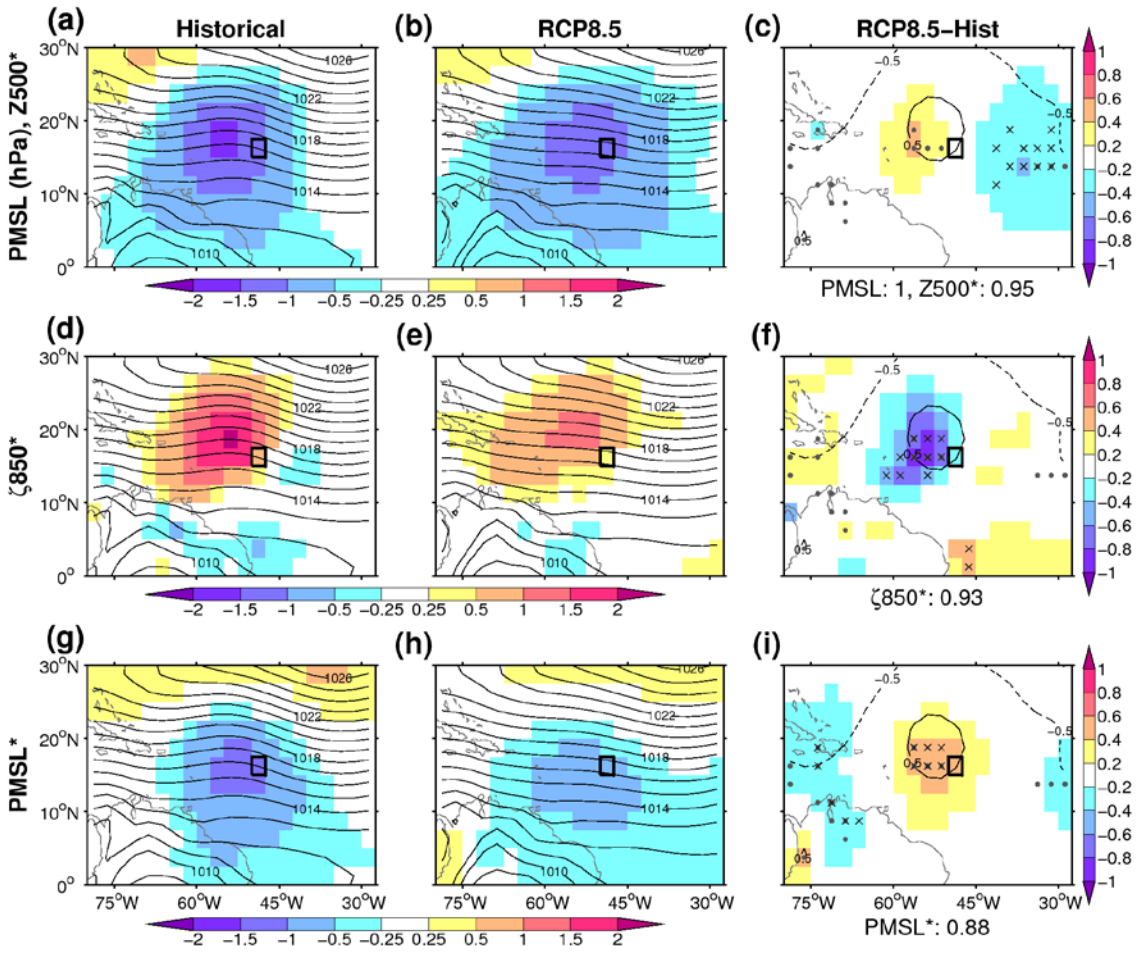

Figure 36. As in Fig. 35, but for a low-latitude grid cell in the North Atlantic.

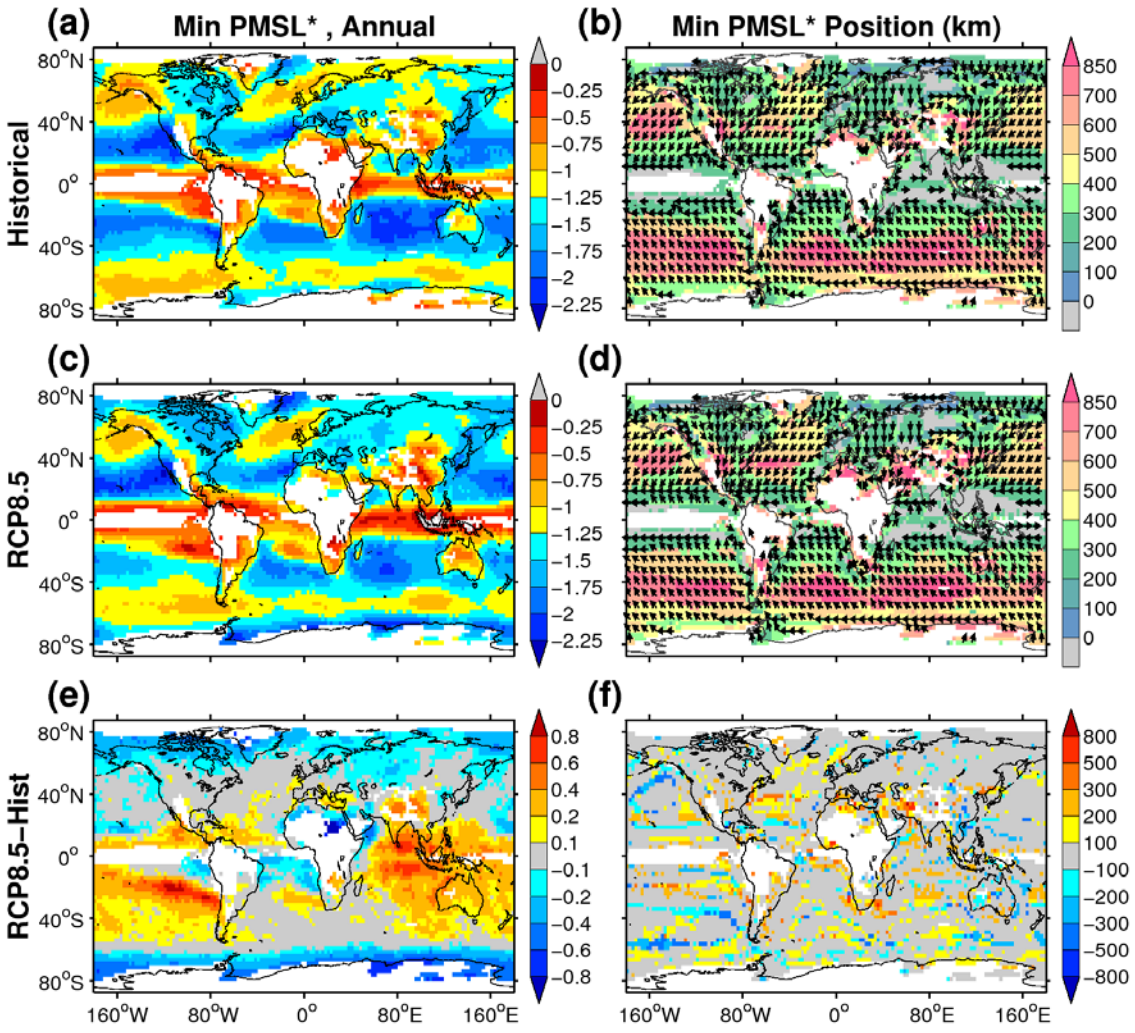

Figure 37. The nearest closed minimum in the z-score of PMSL (PMSL*) associated with the top 1% of annual precipitation events at each grid cell (see section 4.4.b for description). The magnitude of the detected minimum (dimensionless) is shown in the left column. The position of the minimum relative to the grid cell is shown in (b) and (d), where vectors (normalized) point in the direction of the minimum and color fills indicate the distance of the minimum (km) from the grid cell. Vectors are plotted at every third grid cell for better visibility. In (e)-(f), the RCP8.5-historical difference of the respective quantities is shown, where only changes in distance are shown in (f). Missing grid cells

are those in which a minimum was not detected in a box with east-west radius of 1000 km or less from the grid cell, in either the historical or RCP8.5 period.

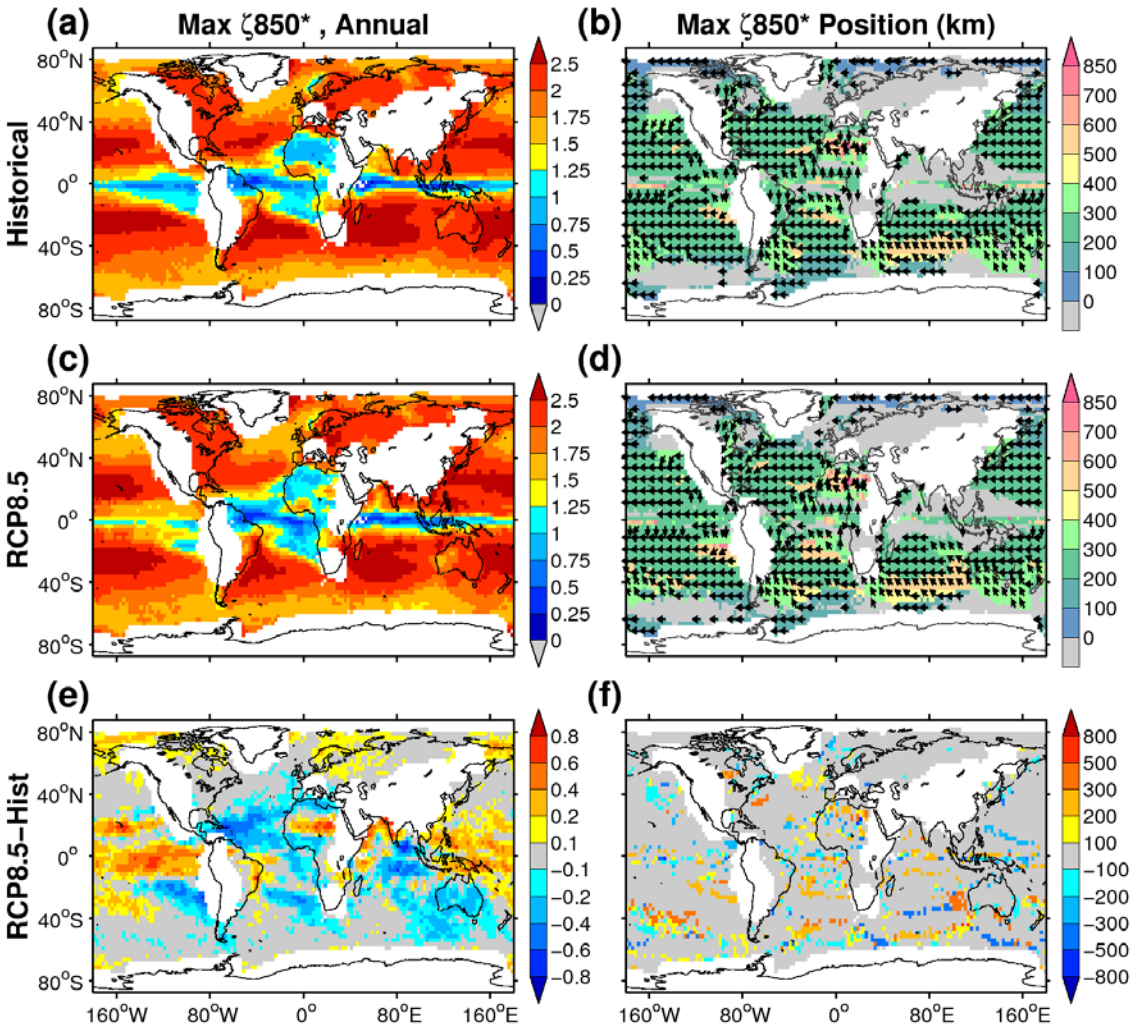

Figure 38. As in Fig. 37, but for the nearest closed maximum of ζ850 z-score (ζ850*). Prior to finding the maximum, Southern Hemisphere ζ850* values were multiplied by -1. Missing values result from a combination of topography at 850 mb and the failure to detect a maximum in a box with east-west radius of 1000 km or less from the grid cell.

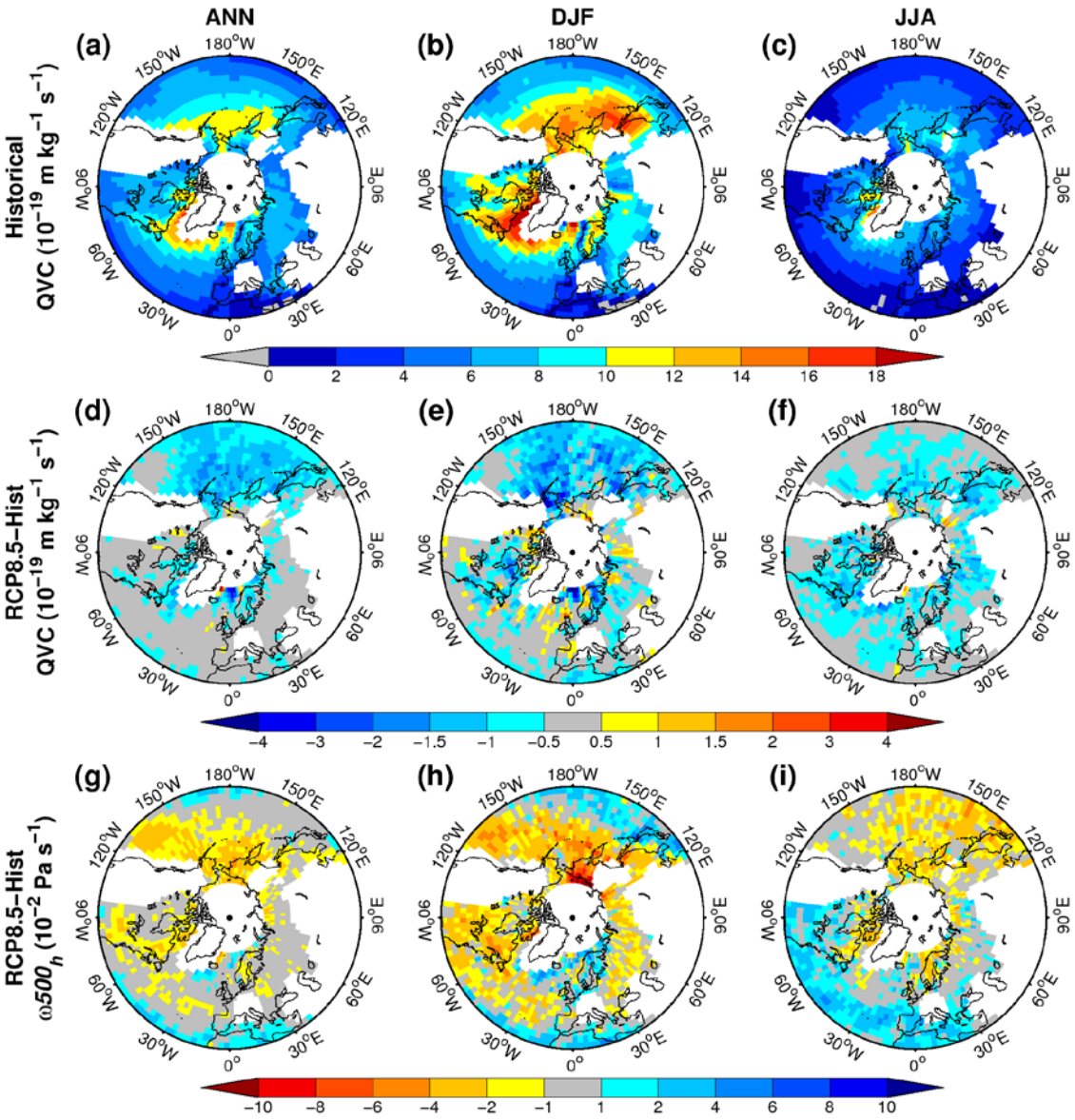

Figure 39. The local **Q**-vector convergence (QVC, 10^{-19} m kg^{-1} s^{-1}) associated with heavy precipitation events in the Northern Hemisphere extratropics (30°-90°N) for the (a)-(c) historical period and (d)-(f) RCP8.5-historical difference (see section 4.4.b for details). In (g)-(i), the RCP8.5-historical difference in local pressure velocity at 500 mb averaged over heavy events ($\Delta\omega 500_h$, 10^{-2} Pa s^{-1}, same quantity as Figs. 32j-i) is shown for comparison. The analysis was performed using (left) all days annually, (middle) DJF days, and (right) JJA days. QVC was not plotted where the 850, 700, or 500 mb level is

below ground or near the poles because of the domain boundary. Missing locations in QVC were also removed in $\Delta\omega 500_h$ for easier comparison. The color bar for $\Delta\omega 500_h$ was reversed from Figs. 32j-i so that consistent changes between $\omega 500_h$ and QVC appear as the same color (i.e., increasing QVC and decreasing $\omega 500_h$ or vice versa).

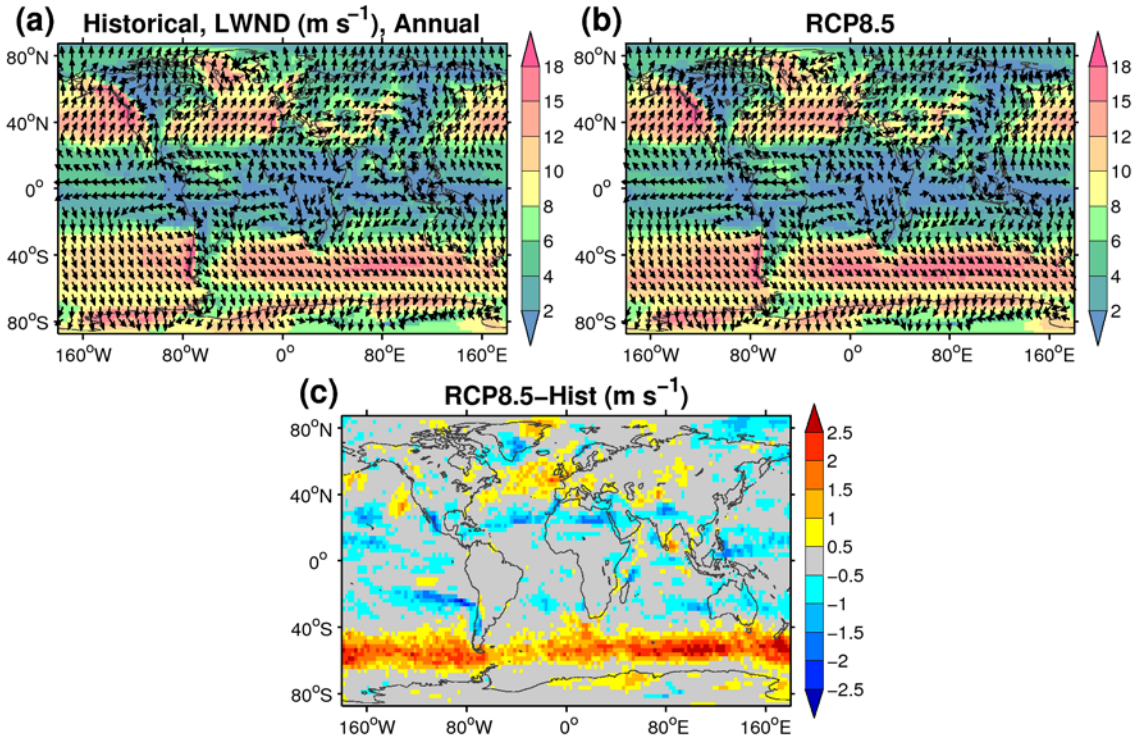

Figure 40. The local low-level wind (LWND, m s^{-1}) averaged over days with heavy precipitation (≥99th percentile, using all seasons) at each grid cell for the (a) historical period, (b) RCP8.5 period, and (c) RCP8.5-historical difference. The vectors (normalized) in the top panels indicate wind direction and the color fills indicate wind speed (m s^{-1}). The vectors are plotted at every third grid cell in the longitude and latitude dimensions. Only differences in wind speed (m s^{-1}) are shown in (c).

References

Alexander, L. V., and Coauthors, 2006: Global observed changes in daily climate extremes of temperature and precipitation. *J. Geophys. Res.*, **111**, D05109, doi:10.1029/2005JD006290.

Alexander, L. V., and J. M. Arblaster, 2009: Assessing trends in observed and modelled climate extremes over Australia in relation to future projections. *Int. J. Climatol.* **29**: 417–435.

Allan, R. P., and B. J. Soden, 2007: Large discrepancy between observed and simulated precipitation trends in the ascending and descending branches of the tropical circulation. *Geophys. Res. Lett.*, **34**, L18705, doi:10.1029/2007GL031460.

Allan, R. P., and B. J. Soden, 2008: Atmospheric warming and the amplification of precipitation extremes. *Science*, **321**, 1481-1484.

Allan, R. P., C. Liu, M. Zahn, D. A. Lavers, E. Koukouvagias, and A. Bodas-Salcedo, 2013: Physically consistent responses of the global atmospheric hydrological cycle in models and observations. *Surv. Geophys.*, doi: 10.1007/s10712-012-9213-z.

Allen, M. R., and W. J. Ingram, 2002: Constraints on future changes in climate and the hydrologic cycle. *Nature*, **419**, 224-232.

Archambault, H. M., L. F. Bosart, D. Keyser, and A. R. Aiyyer, 2008: Influence of large-scale flow regimes on cool-season precipitation in the Northeastern United States. *Mon. Wea. Rev.*, **136**, 2945-2963.

Barnett, D. N., S. J. Brown, J. M. Murphy, D. M. H. Sexton, and M. J. Webb, 2006: Quantifying uncertainty in changes in extreme event frequency in response to doubled CO_2 using a large ensemble of GCM simulations. *Climate Dyn.*, **26**, 489-511.

Bender, F. A.-M., V. Ramanathan, and G. Tselioudis, 2012: Changes in extratropical storm track cloudiness 1983–2008: observational support for a poleward shift. *Climate Dyn.*, **38**, 2037-2053.

Bengtsson, L., M. Botzet, and M. Esch, 1995: Hurricane-type vorticies in a general circulation model. *Tellus*, **47**, 175-196.

Bengtsson, L., K. I. Hodges, and E. Roeckner, 2006: Storm tracks and climate change. *J. Climate*, **19**, 3518-3543.

Boberg, F., P. Berg, P. Thejll, W. J. Gutowski, and J. H. Christensen, 2009: Improved confidence in climate change projections of precipitation evaluated using daily statistics from the PRUDENCE ensemble. *Climate Dyn.*, **32**, 1097-1106.

Boroneant, C., G. Plaut, F. Giorgi, and X. Bi, 2006: Extreme precipitation over the Maritime Alps and associated weather regimes simulated by a regional climate model: Present-day and future climate scenarios. *Theor. Appl. Climatol.*, **86**, 81–99.

Camargo, S. J., 2013: Global and regional aspects of tropical cyclone activity in the CMIP5 models. *J. Climate*, **26**, 9880-9902.

Chang, E. K. M., Y. Guo, and X. Xia, 2012: CMIP5 multimodel ensemble projection of storm track change under global warming. *J. Geophys. Res.*, **117**, D23118, doi:10.1029/2012JD018578.

Changnon, S. A., 2001: Thunderstorm rainfall in the conterminous United States, *Bull. Amer. Meteor. Soc.*, **82**, 1925-1940.

Chen, C., and T. Knutson, 2008: On the verification and comparison of extreme rainfall indices from climate models. *J. Climate*, **21**, 1605-1621.

Chen, M., and Coauthors, 2008a: CPC unified gauge-based analysis of global daily precipitation. *Eos, Trans. Amer. Geophys. Union*, **89** (Western Pacific Geophysics Meeting Suppl.), Abstract A24A-05. [Available online at ftp://ftp.cpc.ncep.noaa.gov/precip/CPC_UNI_PRCP/GAUGE_GLB/DOCU/Chen_et_al_2008_Daily_Gauge_Anal.pdf.]

Chen, M., and Coauthors, 2008b: Quality control of daily precipitation reports at NOAA/CPC. *Extended Abstracts, 12th Conf. on IOAS-AOLS*, New Orleans, LA, Amer. Meteor. Soc., 3.3. [Available online at http://ams.confex.com/ams/pdfpapers/131381.pdf.]

Chen, M., W. Shi, P. Xie, V. B. S. Silva, V. E. Kousky, R. W. Higgins, and J. E. Janowiak, 2008c: Assessing objective techniques for gauge-based analyses of global daily precipitation. *J. Geophys. Res.*, **113**, D04110, doi:10.1029/2007JD009132.

Chou, C., and J. D. Neelin, 2004: Mechanisms of global warming impacts on regional tropical precipitation. *J. Climate*, **17**, 2688-2701.

Chou, C., J. D. Neelin, C.-A. Chen, and J.-Y. Tu, 2009: Evaluating the ‘‘rich-get-richer’’ mechanism in tropical precipitation change under global warming. *J. Climate*, **22**, 1982-2005.

Chou, C., T.-C. Wu, and P.-H. Tan, 2013: Changes in gross moist stability in the tropics under global warming. *Climate Dyn.*, **41**, 2481-2496.

Christian H. J., and Coauthors, 2003: Global frequency and distribution of lightning as observed from space by the Optical Transient Detector, *J. Geophys. Res.*, **108**, D14005, doi: 10.1029/2002JD002347.

Colle, B. A., and C. F. Mass, 2000: The 5–9 February 1996 flooding event over the Pacific Northwest: Sensitivity studies and evaluation of the MM5 precipitation forecasts. *Mon. Wea. Rev.*, **128**, 593-617.

Dai, A., 2001: Global precipitation and thunderstorm frequencies. Part I: Seasonal and interannual variations. *J. Climate*, **14**, 1092-1111.

DeAngelis, A., F. Dominguez, Y. Fan, A. Robock, M. D. Kustu, and D. Robinson, 2010: Evidence of enhanced precipitation due to irrigation over the Great Plains of the United States. *J. Geophys. Res.*, **115**, D15115, doi: 10.1029/2010JD013892.

Dulière, V., Y. Zhang, and E. P. Salathé Jr., 2011: Extreme precipitation and temperature over the U.S. Pacific Northwest: A comparison between observations, reanalysis data, and regional models. *J. Climate*, **24**, 1950-1964.

Easterling, D. R., G. A. Meehl, C. Parmesan, S. A. Changnon, T. R. Karl, and L. O. Mearns, 2000: Climate extremes: Observations, modeling and impacts. *Science*, **289**, 2068-2074.

Emori, S., and S. J. Brown, 2005: Dynamic and thermodynamical changes in mean and extreme precipitation under changed climate. *Geophys. Res. Lett.*, **32**, L17706, doi:10.1029/2005GL023272.

Emori, S., A. Hasegawa, T. Suzuki, and K. Dairaku, 2005: Validation, parameterization dependence, and future projection of daily precipitation simulated with a high-

resolution atmospheric GCM. *Geophys. Res. Lett.*, **32**, L06708, doi: 10.1029/2004GL022306.

Frei, C., J. H. Christenson, M. Déqué, D. Jacob, R. G. Jones, and P. L. Vidale, 2003: Daily precipitation statistics in regional climate models: Evaluation and intercomparison for the European Alps. *J. Geophys. Res.*, **108**, D34102, doi:10.1029/2002JD002287.

Gastineau, G., H. L. Treut, and L. Li, 2008: Hadley circulation changes under global warming conditions indicated by coupled climate models. *Tellus*, **60A**, 863-884.

Gastineau, G. and B. J. Soden, 2009: Model projected changes of extreme wind events in response to global warming. *Geophys. Res. Lett.*, **36**, L10810, doi:10.1029/2009GL037500.

Gastineau, G. and B. J. Soden, 2011: Evidence for a weakening of tropical surface wind extremes in response to atmospheric warming. *Geophys. Res. Lett.*, **38**, L09706, doi: 10.1029/2011GL047138.

Giorgi, F., E. Coppola, E.-S. Im, N. S. Diffenbaugh, X. J. Gao, L. Mariotti, and Y. Shi, 2011: Higher hydroclimatic intensity with global warming, *J. Climate*, **24**, 5309–5324.

Groisman, P. Ya., R. W. Knight, T. R. Karl, D. R. Easterling, B. Sun, and J. H. Lawrimore, 2004: Contemporary changes of the hydrologic cycle over the continguous United States: Trends derived from in situ observations. *J. Hydrometeor.*, **5**, 64-85.

Groisman, P. Y., R. W. Knight, D. R. Easterling, T. R. Karl, G. C. Hegerl, and V. N. Razuvaev, 2005: Trends in intense precipitation in the climate record. *J. Climate*, **18**, 1326-1350.

Groisman, P. Y., R. W. Knight, and T. R. Karl, 2012: Changes in intense precipitation over the central United States. *J. Hydrometeor.*, **13**, 47-66.

Gutowski, W. J., S. G. Decker, R. A. Donavon, Z. Pan, R. W. Arritt, and E. S. Takle, 2003: Temporal-spatial scales of observed and simulated precipitation in central U.S. climate. *J. Climate*, **16**, 3841-3847.

Gutowski and Coauthors, 2008a: Causes of observed changes in extremes and projections of future changes. *Weather and Climate Extremes in a Changing Climate—Regions of Focus: North America, Hawaii, Caribbean, and U.S. Pacific Islands*, T. R. Karl et al., Eds., National Climatic Data Center, 81–116.

Gutowski, W. J., S. S. Willis, J. C. Patton, B. R. J. Schwedler, R. W. Arritt, and E. S. Takle, 2008b: Changes in extreme, cold-season synoptic precipitation events under global warming. *Geophys. Res. Lett.*, **35**, L20710, doi:10.1029/2008GL035516.

Hart, R. E., and R. H. Grumm, 2001: Using normalized climatological anomalies to rank synoptic-scale events objectively. *Mon. Wea. Rev.*, **129**, 2426-2442.

Haylock, M. R., and Coauthors, 2006: Trends in total and extreme South American rainfall in 1960–2000 and links with sea surface temperature. *J. Climate*, **19**, 1490-1512.

Haerter, J. O., and P. Berg, 2009: Unexpected rise in extreme precipitation caused by a shift in rain type? *Nature Geosci.*, **2**, 372-373.

Held, I. M. and B. J. Soden, 2006: Robust responses of the hydrological cycle to global warming. *J. Climate*, **19**, 5686-5699.

Higgins, R. W., W. Shi, E. Yarosh, and R. Joyce, 2000: Improved United States precipitation quality control system and analysis. NCEP/Climate Prediction Center Atlas 7, 40 pp. [Available online at http://www.cpc.ncep.noaa.gov/research_papers/ncep_cpc_atlas/7/.]

Hill, T., and P. Lewicki, 2006: *STATISTICS: Methods and Applications*. 1st ed. StatSoft Inc., 833 pp.

Holton, J. R., 2004: *An Introduction to Dynamic Meteorology*. 4th ed. Elsevier Academic, 535 pp.

Hoskins, B. J., I. Draghici, and H. C. Davies, 1978: A new look at the ω-equation. *Quart. J. Roy. Meteor. Soc.*, **104**, 31-38.

Huang, P., S.-P. Xie, K. Hu, G. Huang, and R. Huang, 2013: Patterns of the seasonal response of tropical rainfall to global warming. *Nat. Geosci.*, **6**, 357-361.

Hung, M.-P., J.-L. Lin, W. Wang, D. Kim, T. Shinoda, and S. J. Weaver, 2013: MJO and convectively coupled equatorial waves simulated by CMIP5 climate models. *J. Climate*, **26**, 6185-6214.

Iorio, J. P., P. B. Duffy, B. Govindasamy, S. L. Thompson, M. Khairoutdinov, and D. Randall, 2004: Effects of model resolution and subgrid scale physics on the simulation of precipitation in the continental United States. *Climate Dyn.*, **23**, 243–258.

IPCC, 2012: Summary for Policymakers. In: Managing the Risks of Extreme Events and Disasters to Advance Climate Change Adaptation [Field, C. B., V. Barros, T. F. Stocker, D. Qin, D. J. Dokken, K. L. Ebi, M. D. Mastrandrea, K. J. Mach, G.-K. Plattner, S. K. Allen, M. Tignor, and P. M. Midgley (eds.)]. A Special Report of Working Groups I and II of the Intergovernmental Panel on Climate Change. Cambridge University Press, Cambridge, UK, and New York, NY, USA, pp. 3-21.

IPCC, 2013: Summary for Policymakers. In: Climate Change 2013: The Physical Science Basis. Contribution of Working Group I to the Fifth Assessment Report of the Intergovernmental Panel on Climate Change [Stocker, T.F., D. Qin, G.-K. Plattner, M. Tignor, S. K. Allen, J. Boschung, A. Nauels, Y. Xia, V. Bex and P.M. Midgley (eds.)]. Cambridge University Press, Cambridge, United Kingdom and New York, NY, USA.

Jones, C., and L. M. V. Carvalho, 2011: Will global warming modify the activity of the Madden–Julian oscillation? *Quart. J. Roy. Meteor. Soc.*, **137**, 544-552.

Jones, C., and L. M. V. Carvalho, 2012: Spatial–intensity variations in extreme precipitation in the contiguous United States and the Madden–Julian oscillation. *J. Climate*, **25**, 4898-4913.

Karl, T. R., and R. W. Knight, 1998: Secular trends of precipitation amount, frequency, and intensity in the United States. *Bull. Amer. Meteor. Soc.*, **79**, 231-241.

Kawazoe, S., and W. J. Gutowski, 2013: Regional, very heavy daily precipitation in CMIP5 simulations. *J. Hydrometeor.*, **14**, 1228-1242.

Kendon, E.J., D.P. Rowell, R.G. Jones, and E. Buonomo, 2008: Robustness of future changes in local precipitation extremes. *J. Climate*, **21**, 4280-4297.

Kharin, V. V., and F. W. Zwiers, 2005: Estimating extremes in transient climate change simulations. *J. Climate*, **18**, 1156–1173.

Kharin, V. V., F. W. Zwiers, X. Zhang, and G. C. Hegerl, 2007: Changes in temperature and precipitation extremes in the IPCC ensemble of global coupled model simulations. *J. Climate*, **20**, 1419-1444.

Kharin, V. V., F. W. Zwiers, X. Zhang, and M. Wehner, 2013: Changes in temperature and precipitation extremes in the CMIP5 ensemble. *Climatic Change*, **119**, 345-357.

Kiktev, D., D. M. H. Sexton, L. Alexander, and C. K. Folland, 2003: Comparison of modeled and observed trends in indices of daily climate extremes, *J. Climate*, **16**, 3560–3571.

Kimoto, M., N. Yasutomi, C. Yokoyama, and S. Emori, 2005: Projected changes in precipitation characteristics near Japan under the global warming. *SOLA*, **1**, 85–88.

Kunkel, K. E., D. R. Easterling, D. A. R. Kristovich, B. Gleason, L. Stoecker, and R. Smith, 2010: Recent increases in U.S. heavy precipitation associated with tropical cyclones. *Geophys. Res. Lett.*, **37**, L24706, doi:10.1029/2010GL045164.

Kunkel, K. E., D. R. Easterling, D. A. R. Kristovich, B. Gleason, L. Stoecker, and R. Smith, 2012: Meteorological causes of the secular variations in observed extreme precipitation events for the conterminous United States. *J. Hydrometeor.*, **13**, 1131-1141.

Lambert, F. H., and M. J. Webb, 2008: Dependency of global mean precipitation on surface temperature. *Geophys. Res. Lett.*, **35**, L16706, doi:10.1029/2008GL034838.

Lau, K.-M., Y. P. Zhou, and H.-T. Wu, 2008: Have tropical cyclones been feeding more extreme rainfall? *J. Geophys. Res.*, **113**, D23113, doi:10.1029/2008JD009963.

Lau, K.-M., and H.-T. Wu, 2011: Climatology and changes in tropical oceanic rainfall characteristics inferred from Tropical Rainfall Measuring Mission (TRMM) data (1998–2009), *J. Geophys. Res.*, **116**, D17111, doi:10.1029/2011JD015827.

Lau, W. K.-M., H.-T. Wu, and K.-M. Kim, 2013: A canonical response of precipitation characteristics to global warming from CMIP5 models. *Geophys. Res. Lett.*, **40**, 3163-3169, doi: 10.1002/grl.50420.

Lenderink, G. and E. V. Meijgaard, 2008: Increase in hourly precipitation extremes beyond expectations from temperature changes. *Nat. Geosci.*, **1**, 511-514.

Li, F., W. D. Collins, M. F. Wehner, D. L. Williamson, J. G. Olson, C. Algieri, 2011: Impact of horizontal resolution on simulation of precipitation extremes in an aqua-planet version of Community Atmospheric Model (CAM3). *Tellus*, **63**, 884-892.

Li, F., D. Rosa, W. D. Collins, and M. F. Wehner, 2012: ‘‘Super-parameterization’’: A better way to simulate regional extreme precipitation? *J. Adv. Model. Earth Syst.*, **4**, M04002, doi:10.1029/2011MS000106.

Liepert, B. G., and M. Previdi, 2009: Do models and observations disagree on the rainfall response to global warming? *J. Climate*, **22**, 3156-3166.

Lionello, P. and F. Giorgi, 2007: Winter precipitation and cyclones in the Mediterranean region: Future climate scenarios in a regional simulation. *Adv. Geosci.*, **12**, 153–158.

Lintner, B. R., and J. D. Neelin, 2007: A prototype for convective margin shifts. *Geophys. Res. Lett.*, **34**, L05812, doi:10.1029/2006GL027305.

Lintner, B. R., M. Biasutti, N. S. Diffenbaugh, J.-E. Lee, M. J. Niznik, and K. L. Findell, 2012: Amplification of wet and dry month occurrence over tropical land regions in response to global warming, *J. Geophys. Res.*, **117**, D11106, doi:10.1029/2012JD017499.

Liu, S. C., C. Fu, C.-J. Shiu, J-P. Chen, and F. Wu, 2009: Temperature dependence of global precipitation extremes. *Geophys. Res. Lett.*, **36**, L17702, doi: 10.1029/2009GL040218.

Loikith, P. C., B. R. Lintner, J. Kim, H. Lee, J. D. Neelin, and D. E. Waliser, 2013: Classifying reanalysis surface temperature probability density functions (PDFs) over North America with cluster analysis. *Geophys. Res. Lett.*, **40**, 3710-3714, doi:10.1002/grl.50688.

Lu, J., G. A. Vecchi, and T. Reichler, 2007: Expansion of the Hadley cell under global warming. *Geophys. Res. Lett.* **34**, L06805, doi:10.1029/2006GL028443.

Manganello, J. V., and Coathors, 2012: Tropical cyclone climatology in a 10-km global atmospheric GCM: Toward weather-resolving climate modeling. *J. Climate*, **25**, 3867-3893.

Marengo, J. A., M. Rusticucci, O. Penalba, and M. Renom, 2010: An intercomparison of observed and simulated extreme rainfall and temperature events during the last half of the twentieth century: Part 2: Historical trends. *Climatic Change*, **98**, 509-529.

May, W., 2004: Simulation of the variability and extremes of daily rainfall during the Indian summer monsoon for present and future times in a global time-slice experiment. *Climate Dyn.*, **22**, 183–204.

McCabe G. J., M. P. Clark, and M. C. Serreze, 2001: Trends in northern hemisphere surface cyclone frequency and intensity. *J. Climate*, **14**, 2763–2768.

McClean, J. L., and Coathors, 2011: A prototype two-decade fully-coupled fine-resolution CCSM simulation. *Ocean Modell.*, **39**, 10-30.

Meehl, G. A., J. M. Arblaster and C. Tebaldi, 2005: Understanding future patterns of increased precipitation intensity in climate model simulations. *Geophys. Res. Lett.*, **32**, L18719, doi:10.1029/2005GL023680.

Meehl, G. A., C. Covey, T. Delworth, M. Latif, B. McAvaney, J. F. B. Mitchell, R. J. Stouffer, and K. E. Taylor, 2007: The WCRP CMIP3 multimodel dataset: A new era in climate change research, *Bull. Amer. Meteor. Soc.*, **88**, 1383-1394.

Mesinger, F., and Coauthors, 2006: North American Regional Reanalysis. *Bull. Amer. Meteor. Soc.*, **87**, 343-360.

Milrad, S. M., E. H. Atallah, and J. R. Gyakum, 2010: Synoptic typing of extreme cool-season precipitation events at St. John's, Newfoundland, 1979-2005. *Wea. Forecasting*, **25**, 562-586.

Min, S., X. Zhang, F. W. Zwiers, and G. C. Hegerl, 2011: Human contribution to more-intense precipitation extremes. *Nature*, **470**, 378-381.

Moss, R. H., and Coauthors, 2010: The next generation of scenarios for climate change research and assessment. *Nature*, **463**, 747-756.

Neelin, J. D., C. Chou, and H. Su, 2003: Tropical drought regions in global warming and El Niño teleconnections. *Geophys. Res. Lett.*, **30**, 2275, doi:10.1029/2003GL018625.

Novak, D. R., L. F. Bosart, D. Keyser, and J. S. Waldstreicher, 2004: An observational study of cold season-banded precipitation in northeast U.S. cyclones. *Wea. Forecasting*, **19**, 993-1010.

O'Gorman, P. A. and T. Schneider, 2009a: Scaling of precipitation extremes over a wide range of climates simulated with an idealized GCM. *J. Climate*, **22**, 5676-5685.

O'Gorman, P. A. and T. Schneider, 2009b: The physical basis for increases in precipitation extremes in simulations of 21st-century climate change. *Proc. Nat. Acad. Sci.*, **106**, 14773-14777.

O'Gorman, P. A., 2010: Understanding the varied response of the extratropical storm tracks to climate change. *Proc. Nat. Acad. Sci.*, **107**, 19176-19180.

O'Gorman, P. A., R. P. Allan, M. P. Byrne, M. Previdi, 2012: Energetic constraints on precipitation under climate change. *Surv. Geophys.*, **33**, 585-608.

Orlowsky, B., and S. I. Seneviratne, 2012: Global changes in extremes events: Regional and seasonal dimension. *Climatic Change*, **110**, 669-696.

Pall, P., M. R. Allen, and D. A. Stone, 2007: Testing the Clausius-Clapeyron constraint on changes in extreme precipitation under CO_2 warming. *Climate Dyn.*, **28**, 351-363.

Pall, P., T. Aina, D. A. Stone, P. A. Stott, T. Nozawa, A. G. J. Hilbberts, D. Lohmann, and M. R. Allen, 2011: Anthropogenic greenhouse gas contribution to flood risk in England and Wales in autumn 2000. *Nature*, **470**, 382-385.

Perkins, S. E., A. J. Pitman, N. J. Holbrook, and J. McAneney, 2007: Evaluation of the AR4 climate models' simulated daily maximum temperature, minimum temperature, and precipitation over Australia using probability density functions. *J. Climate*, **20**, 4356-4376.

Pfahl, S., and H. Wernli, 2012: Quantifying the relevance of cyclones for precipitation extremes. *J. Climate*, **25**, 6770-6780.

Previdi, M., and B. Liepert, 2008: Interdecadal variability of rainfall on a warming planet, *Eos*, **89**, 193-195, doi:10.1029/2008EO210002.

Raible, C. C., M. Yoshimori, T. F. Stocker, and C. Casty, 2007: Extreme midlatitude cyclones and their implications for precipitation and wind speed extremes in simulations of the maunder minimum versus present day conditions. *Climate Dyn.*, **28**, 409-423.

Rappaport, E. N., 2000: Loss of life in the United States associated with recent Atlantic tropical cyclones. *Bull. Amer. Meteor. Soc.*, **81**, 2065-2073.

Riemann-Campe, K., K. Fraedrick, F. Lunkeit, 2009: Global climatology of Convective Available Potential Energy (CAPE) and Convective Inhibition (CIN) in ERA-40 reanalysis. *Atmos. Res.*, **93**, 534-545.

Ruiz-Barradas, A., and S. Nigam, 2006: IPCC's twentieth-century climate simulations: Varied representations of North American hydroclimate variability. *J. Climate*, **19**, 4041–4058.

Salathé, E. P. Jr., 2006: Influences of a shift in North Pacific storm tracks on western North American precipitation under global warming. *Geophys. Res. Lett.*, **33**, L19820, doi:10.1029/2006GL026882.

Schubert, S. D., Y. Chang, M. J. Suarez, and P. J. Pegion, 2008: ENSO and wintertime extreme precipitation events over the contiguous United States. *J. Climate*, **21**, 22-39.

Scoccimaro, E., S. Gualdi, A. Bellucci, M. Zampieri, and A. Navarra, 2013: Heavy precipitation events in a warmer climate: results from CMIP5 models. *J. Climate*, **26**, 7902-7911.

Seager, R., N. Naik, and G. A. Vecchi, 2010: Thermodynamic and dynamic mechanisms for large-scale changes in the hydrological cycle in response to global warming. *J. Climate*, **23**, 4651-4668.

Semmler, T., and D. Jacob, 2004: Modeling extreme precipitation events—a climate change simulation for Europe. *Global Planet. Change, **44**, 119-127.*

Seneviratne, S. I., and Coauthors, 2012: Changes in climate extremes and their impacts on the natural physical environment. In: Managing the Risks of Extreme Events and Disasters to Advance Climate Change Adaptation [Field, C. B., V. Barros, T. F. Stocker, D. Qin, D. J. Dokken, K. L. Ebi, M. D. Mastrandrea, K. J. Mach, G.-K. Plattner, S. K. Allen, M. Tignor, and P. M. Midgley (eds.)]. A Special Report of Working Groups I and II of the Intergovernmental Panel on Climate Change (IPCC). Cambridge University Press, Cambridge, UK, and New York, NY, USA, pp. 109-230.

Shiu C.-J., S. C. Liu, C. Fu, A. Dai, and Y. Sun, 2012: How much do precipitation extremes change in a warming climate? *Geophys. Res. Lett.*, **39**, L17707, doi:10.1029/2012GL052762.

Sillmann, J., V. V. Kharin, F. W. Zwiers, X. Zhang, and D. Bronaugh, 2013a: Climate extreme indices in the CMIP5 multimodel ensemble: Part 1. Model evaluation in the present climate. *J. Geophys. Res. Atmos.*, **118**, 1716-1733.

Sillmann, J., V. V. Kharin, F. W. Zwiers, X. Zhang, and D. Bronaugh, 2013b: Climate extreme indices in the CMIP5 multimodel ensemble: Part 2. Future climate projections. *J. Geophys. Res. Atmos.*, **118**, 2473-2493.

Sugiyama, M., H. Shiogama, and S. Emori, 2010: Precipitation extreme changes exceeding moisture content increases in MIROC and IPCC climate models. *Proc. Nat. Acad. Sci.*, **107**, 571-575.

Sun, Y., S. Solomon, A. Dai, and R. W. Portmann, 2007: How often will it rain? *J. Climate*, **20**, 4801-4818.

Taylor, K. E., R. J. Stouffer, and G. A. Meehl, 2009: A summary of the CMIP5 experiment design. PCDMI Rep., 33 pp. [Available online at http://cmip-pcmdi.llnl.gov/cmip5/docs/Taylor_CMIP5_design.pdf.]

Taylor, K. E., R. J. Stouffer, and G. A. Meehl, 2012: An overview of CMIP5 and the experiment design. *Bull. Amer. Meteor. Soc.*, **93**, 485-498.

Tebaldi, C., K. Hayhoe, J. M. Arblaster, and G. A. Meehl, 2006: Going to the extremes: An intercomparison of model-simulated historical and future changes in extreme events. *Climatic Change*, **79**, 185-211.

Tomassini, L., and D. Jacob, 2009: Spatial analysis of trends in extreme precipitation events in high-resolution climate model results and observations for Germany. *J. Geophys. Res., **114**,* D12113, doi:10.1029/2008JD010652.

Trenberth, K. E., 1999: Conceptual framework for changes of extremes of the hydrological cycle with climate change. *Climatic Change*, **42**, 327–339.

Trenberth, K. E., A. Dai, R. M. Rasmussen, and D. B. Parsons, 2003: The changing character of precipitation. *Bull. Amer. Meteor. Soc.*, **84**, 1205-1217.

Vecchi, G. A., B. J. Soden, A. T. Wittenberg, I. M. Held, A. Leetmaa, and M. J. Harrison, 2006: Weakening of tropical Pacific atmospheric circulation due to anthropogenic forcing. *Nature*, **441**, 73-76.

Vecchi, G.A. and B. J. Soden, 2007: Global warming and the weakening of the tropical circulation. *J. Climate*, **20**, 4316-4340.

Villarini, G., and G. Vecchi, 2013: Projected increases in North Atlantic tropical cyclone intensity from CMIP5 models. *J. Climate*, **26**, 3231-3240.

Villarini, G., J. A. Smith, G. A. Vecchi, 2013a: Changing frequency of heavy rainfall over the central United States. *J. Climate*, **26**, 351-357.

Villarini, G., E. Scoccimarro, and S. Gualdi, 2013b: Projections of heavy rainfall over the central United States based on CMIP5 models. *Atmos. Sci. Lett.*, **14**, 200-205.

Wang, X. L., V. R. Swail, and F. W. Zwiers, 2006: Climatology and changes of extratropical cyclone activity: Comparison of ERA-40 with NCEP-NCAR reanalysis for 1958–2001. *J. Climate*, **19**, 3145–3166.

Wehner, M. F., R. L. Smith, G. Bala, and P. Duffy, 2010: The effect of horizontal resolution on simulation of very extreme United States precipitation events in a global atmosphere model. *Climate Dyn.*, **34**, 241-247.

Wehner, M. F., 2013: Very extreme seasonal precipitation in the NARCCAP ensemble: model performance and projections. *Climate Dyn.*, **40**, 59-80.

Wentz, F. J., L. Ricciardulli, K. Hilburn, C. Mears, 2007: How much more rain will global warming bring? *Science*, **317**, 233-235.

Westra, S., L. Alexander, and F. Zwiers, 2013: Global increasing trends in annual maximum daily precipitation. *J. Climate*, **26**, 3904-3918.

Wilby, R. L., and T. M. L. Wigley, 2002: Future changes in the distribution of daily precipitation totals across North America. *Geophys. Res. Lett.*, **29**, 1135, doi:10.1029/2001GL013048.

Wilcox, E. M., and L. J. Donner, 2007: The frequency of extreme rain events in satellite rain-rate estimates and an atmospheric general circulation model. *J. Climate*, **20**, 53-69.

Wilks, D. S., 2006: *Statistical Methods in the Atmospheric Sciences*. 2nd ed. Elsevier Inc., 627 pp.

Wuebbles, D., and Coauthors, 2013: CMIP5 climate model analyses: Climate extremes in the United States. *Bull. Amer. Meteor. Soc.*, doi: 10.1175/BAMS-D-12-00172.1, in press.

Yin, J. H., 2005: A consistent poleward shift of the storm tracks in simulations of 21st century climate. *Geophys. Res. Lett.*, **32**, L18701, doi:10.1029/2005GL023684.

Yiou, P., and M. Nogaj, 2004: Extreme climatic events and weather regimes over the North Atlantic: When and where? *Geophys. Res. Lett.*, **31**, L07202, doi:10.1029/2003GL019119.

Zhang, X., W. D. Hogg, and E. Mekis, 2001: Spatial and temporal characteristics of heavy precipitation events over Canada. *J. Climate*, **14**, 1923-1936.

Zhang, X., J. Wang, F. W. Zwiers, and P. Y. Groisman, 2010: The influence of large-scale climate variability on winter maximum daily precipitation over North America. *J. Climate*, **23**, 2902-2915.

Zwiers, F. W., and V. V. Kharin, 1998: Changes in the extremes of the climate simulated by CCC GCM2 under CO_2 doubling. *J. Climate*, **11**, 2200-2222.